WARWICK
THE UNIVERSITY OF WARWICK

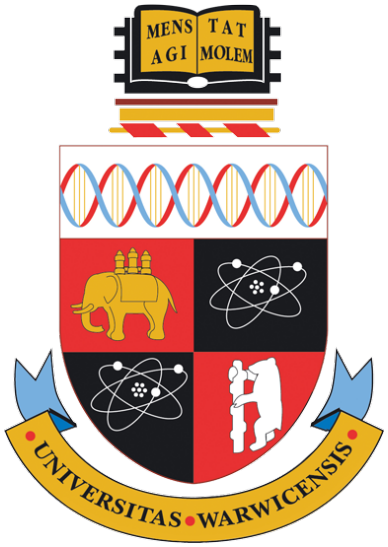

Performance Analysis of mmWave Vehicle-to-Vehicle Communications: A Stochastic Geometry Approach

by

Mümin ÖZPOLAT

Thesis

Submitted to the University of Warwick

in partial fulfilment of the requirements

for admission to the degree of

Doctor of Philosophy

WMG

February 2021

Contents

List of Tables

List of Figures

Acknowledgments

First of all, I would like express my sincere gratitude to my supervisors, Dr Matthew D. Higgins and Dr Erik Kampert. Thanks to their guidance and encouragement, I overcame a variety of hard-to-overcome problems ranging from the conceptual and cognitive challenges of the field to delivering world-class academic outputs.

I am thankful to Dr Konstantinos Koufos for contributing his expertise in this field. The rewarding academic discussions with him have helped greatly to improve the quality of this thesis.

I am thankful to Dr Osama Alluhaibi and Dr Tony Mo for their various contributions on the academic outputs of this PhD.

Additionally, I would like thank the Ministry of National Education, Republic of Turkey, and University of Warwick for the funding of this PhD.

Last but definitely not the least, I would like to express my heartfelt gratitude to my beloved wife Elvan who never stopped supporting me. Finally, I must express my gratitude to my beloved mom and dad who have supported me all the time throughout my life.

Mümin ÖZPOLAT, Coventry, February, 2021

List of Publications Associated with this Research

Published

- **M. Ozpolat**, E. Kampert, P. A. Jennings and M. D. Higgins, "A Grid-Based Coverage Analysis of Urban mmWave Vehicular Ad Hoc Networks," in IEEE Communications Letters, vol. 22, no. 8, pp. 1692-1695, Aug. 2018

- **M. Ozpolat**, O. Alluhaibi, E. Kampert and M. D. Higgins, "Connectivity Analysis for mmWave V2V Networks: Exploring Critical Distance and Beam Misalignment," 2019 IEEE Global Communications Conference (GLOBECOM), Waikoloa, HI, USA, 2019, pp. 1-6

- **M. Ozpolat**, K. Bhargava, E. Kampert and M. D. Higgins, "Multi-Lane Urban mmWave V2V Networks: A Path Loss Behaviour Dependent Coverage Analysis," Vehicular Communications, Elsevier

To Be Submitted

- **M. Ozpolat**, E. Kampert, and M. D. Higgins, "Routing-Based Mean Interference Analysis of mmWave V2V Networks"

Abstract

Advanced sensory systems are the driving force behind autonomous vehicles. They have led to such vehicles producing and processing much more content-intensive visual data. It is foreseen that traffic consisting solely of autonomous vehicles will enable people and goods to travel more safely. Using millimetre wave (mmWave) frequencies for wireless communication between vehicles is a rising research topic, both to enhance safety and reliability of autonomous vehicles and to meet the data rate required by the content-intensive data-set produced by their advanced sensory systems. The main goal of this thesis is to make a stochastic analysis of the signal quality that can be achieved by vehicles when using mmWave frequencies for the wireless communication between them. To address this issue, the tools of stochastic geometry is used in this thesis. Firstly, stochastic geometry provides advanced mathematical properties to model the system fairly accurate and tractable. Secondly, resulting analytical model helps system designers to develop insights to understand relationships between system parameters.

The first academic contribution of this thesis is a two-fold probabilistic connectivity analysis of an autonomous vehicle fleet for a single-lane road. In other words, it stochastically models the connectivity probability of the sensory data of the head and tail vehicles of the fleet shared over intermediate fleet vehicles by using a Poisson point process and geometric probability tools. The proposed model takes into account both the threshold of the obtained Signal-to-interference-plus-noise ratio in terms of the critical distance requirements and the beam misalignment issues caused by the lateral displacement of the vehicles in the lane.

The second contribution of this thesis is a mean interference analysis for a *typical* receiver if the vehicles employ in-lane and closest vehicle routing schemes for a two-lane road. By comparing these two routing schemes, a strategy is proposed for different antenna beamwidths and vehicle densities. Additionally, the distribution of autonomous vehicular traffic, that is modelled by the shifted Poisson point process, gains more realism by taking into account platooning-based headway distance requirements.

The third contribution of this thesis is a derivation of the coverage probability and road spectral efficiency for multi-lane vehicle-to-vehicle communications, by taking into account the blockage impact of adjacent lane vehicles and antenna-placement dependent path loss behaviour under an in-lane routing scheme. Finally, all the analytical models are verified by Monte Carlo simulations.

Acronyms

3GPP 3rd Generation Partnership Project.

ABG Alpha-Beta-Gamma.

AFC Automated Frequency Control.

ASE Area Spectral Efficiency.

BPP Binomial Point Process.

CI Close In.

C-ITS Cooperative Intelligent Transportation System.

C-V2X Cellular Vehicle-to-Everything.

CAV Connected Autonomous Vehicles.

CCAV Cooperative Connected Autonomous Vehicles.

CVR Closest Vehicle Routing.

DSRC Dedicated Short Range Communications.

FCC Federal Communications Commission.

FSPL Free Space Path Loss.

ILR In-Lane Routing.

LIDAR Light Detection and Ranging.

LOS Line-of-Sight.

LTE-A Long Term Evaluation-Advanced.

MGF Moment Generating Function.

MHCPP Matern Hardcore Point Process.

MIMO Multiple Input Multiple Output.

mmWave Millimetre Wave.

NLOS Non-Line-of-Sight.

Ofcom Office of Communications.

OLOS Obstructed-Line-of-Sight.

P2P Peer-to-Peer.

PCP Poisson Clustered Process.

PGFL Probability Generating Functional.

PLE Path Loss Exponent.

PPP Poisson Point Process.

RSE Road Spectral Efficiency.

RSU Road Side Unit.

SINR Signal-to-Interference-Plus-Noise Ratio.

SNR Signal-to-Noise Ratio.

V2I Vehicle-to-Infrastructure.

V2V Vehicle-to-Vehicle.

V2X Vehicle-to-Everything.

VANET Vehicular Ad Hoc Network.

Symbols

α	Generic Path Loss Exponent
α_L	LOS Path Loss Exponent
α_N	NLOS Path Loss Exponent
β	Angle between Closest Adjacent Lane Tx-Rx Pair
η	Large Vehicle Ratio
θ	Angle of Boresight Error between any Interferer and Rx
λ	Density of Vehicles/Nodes
λ_t	Density of Transmitter Vehicles/Nodes
$\mathbf{\Phi}$	Point Process
ϕ	Half-Power Beamwidth
ϕ_h	Half of Half-Power Beamwidth
A	Path Loss Intercept
B	Bandwidth
c	Speed of Light
d	Distance between Tx-Rx Pair
d_0	Reference Distance
$\mathbb{E}$	Expected Value
f_c	Carrier Frequency
G_m	Main Lobe Antenna Gain
g_s	Side Lobe Antenna Gain
h_o	Small-Scale Fading Gain between Tx and Rx
h_i	Small-Scale Fading Gain between i-th Interferer and Rx
$\mathcal{L}$	Laplace Transform
L_i	i-th Lane
L_w	Lane Width
N_0	Noise Power
$\mathbb{P}$	Probability
$\mathbb{P}_c$	Coverage Probability
$\mathbb{P}_{G_mG_m}$	Main-to-Main Lobe Alignment Probability
$\mathbb{P}_{G_mg_s}$	Main-to-Side Lobe Alignment Probability
$\mathbb{P}_{g_sg_s}$	Side-to-Side Lobe Alignment Probability
P_t	Transmitter Power

$\mathcal{T}$	SINR Threshold

Chapter 1

Introduction

1.1 An Introduction to Autonomous Vehicles

In general, as we move ever more towards a digitally centred society, the number of electronic devices is rapidly increasing. As such, this trend means that the amount of data generated, transmitted, and stored is also rising. In the vehicular and mobility services application domains, these trends and observations are no different. For instance, currently, the average number of sensors and electronic control units in a new vehicle is estimated to have increased from a few, to now be around 200 [1]. This trend is largely driven by the proliferation of new and improved sensors in image detection and processing technologies, artificial intelligence engines, their fusion units, and the wireless communications provisions that will provide the basis that enable *autonomous* features.

The premise of autonomous vehicles is that they will safely enable a vast number of socially diverse passengers to move from point A to point B with a higher efficiency. This premise is fulfilled by each of the vehicle's sensors *seeing* further, faster, and with higher accuracy and precision than human drivers. Hence, the vehicle will make subsequent *smarter* decisions. This thus leads to both an increase in the number of heterogeneous sensors and the quantity of data produced, which in turn leads to the emergence of vehicle behaviours, such as obstacle and/or collision detection/avoidance, platooning, situational awareness, and route planning. The 'UK Connected and Automated Mobility Roadmap to 2030' has appeared to accelerate the development of this self-driving vehicle revolution [2]. Table 1.1 broadly classifies the sensors that support autonomous driving based on their performance in terms of range, data rate, accuracy etc. for different conditions, each with their own advantages and disadvantages. Fusion of the data generated by those sensors eliminates some of those disadvantages, and increases the overall quality of the produced and processed data.

Table 1.1: Comparison of potential sensors for autonomous driving

Sensor Type	Range	Drawback	Required data rate per sensor	Detection accuracy	Detection resolution	Brightness dependency	Quantity
Radar	~200 m	difficult to distinguish targets	up to 15 Mbps	high	medium	good	4-6
Camera	~100 m	needs computer vision	10-700 Mbps	medium	high	poor	6-12
LIDAR	~100 m	high cost	10-100 Mbps	high	high	good	1-5
Ultrasonic	~10 m	short range	up to 0.01 Mbps	high	low	good	8-16

1.2 Wireless Communications for Connected Autonomous Vehicles

The sensor vision of a generic autonomous vehicle is visualized in Fig. 1.1 where the sensor's range is typically 250 m at maximum. However, this range could be reduced to only a few meters in congested traffic. That is to say, that whilst the community is continually striving to increase the performance and capabilities of cameras and other imaging technologies, ultimately, they are still limited by blockages such as buildings, foliage, and pedestrians. Hence, to overcome such limitations, the connected autonomous vehicle (CAV) concept has evolved. It is the *connected* element of this concept that is vital to the future capability of the vehicles for one core reason – that of being able to *see* beyond line-of-sight. Thus, vehicle-to-vehicle (V2V) communications are seen as a way to provide an awareness beyond line-of-sight. For example, using V2V communications, it may be possible to resolve blind spots, detect empty parking spots, identify positions, directions and velocities of all vehicles in the vicinity etc.

V2V communications in general has been a popular topic and under investigation by many academics for many years now. Additionally, it is feasible to establish a communications link from Vehicle-to-Infrastructure (V2I), Vehicle-to-Pedestrian (V2P), as well as V2V. To maintain simplicity in nomenclature, Vehicle-to-Everything (V2X) is now more commonly used. As a result of the associated research, the latest V2X protocols to emerge are known as Dedicated Short Range Communications (DSRC) which is based on IEEE 802.11p [3] and Cellular-Vehicle-to-Everything (C-V2X) [4] as part of the 3rd Generation Partnership Project (3GPP) Release 14. DSRC provides a communications link between vehicles and supports up to 1 km in the best case. It operates at 5.8 GHz with a 10 MHz bandwidth per channel [3], and the maximum data rate in practice is between 2 and 6 Mbps [5].

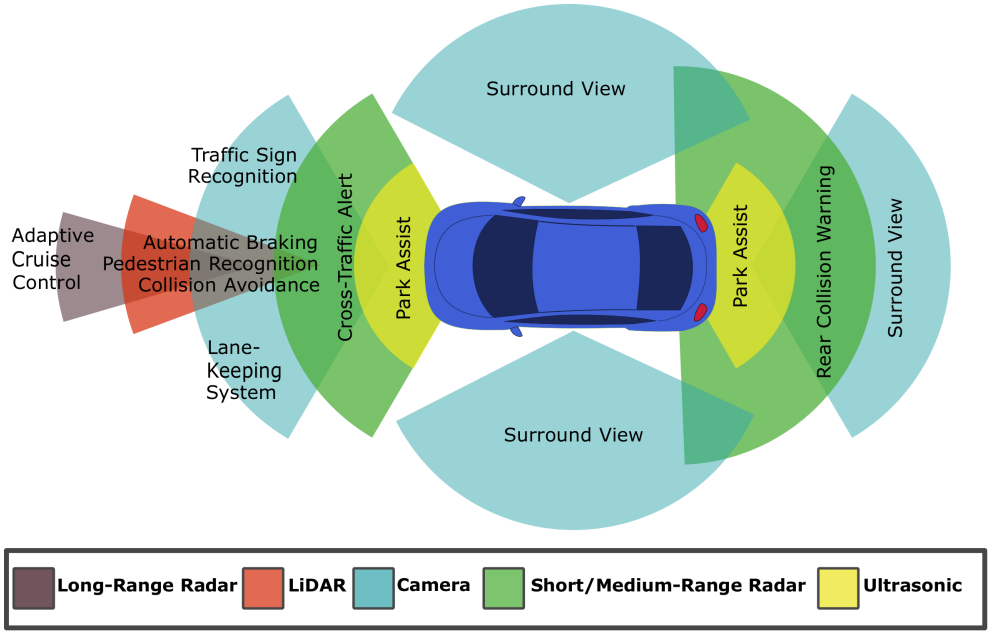

Figure 1.1: A selection of vehicular sensors and their ranges that are typically used in enabling Advanced Driver-Assistance System (ADAS) features [6].

C-V2X uses the cellular infrastructure of the Long Term Evolution-Advanced (LTE-A) standard. It spans multiple bands between 450 MHz and 5.9 GHz and achieves a data rate up to 1 Gbps [7]. The latencies of C-V2X and DSRC are in the range of 10 ms to 200 ms [8]. Moreover, the use of recently developed and available V2V protocol provides enough data rate for safety features such as forward collision warnings, do not pass warnings, blind intersection warnings, and red light violations [9].

These protocols are not able to reach the extremely high date rates that are required for the exchange of raw camera and sensor data, anticipated to be in the tens of Gbps [5]. Thus, the capabilities of DSRC and C-V2X for V2X are shown to be insufficient [9] for many of the core needs of future CAVs. Moreover, they are limited by the bandwidth they offer in comparison to the rate of growth in sensor data, demanded by vehicle manufacturers to fully exploit cooperative autonomy features.

To overcome this bandwidth/data rate challenge, academia proposes to use higher carrier frequencies, in a range where plenty of unallocated spectrum exists. These frequencies are between 30 GHz and 300 GHz GHz, commonly known as millimeter waves (mmWave) due to the wavelength of such frequencies being in the order of millimetres. For instance, Fig. 1.2 shows the relationship between frequency and attenuation per km in signal power. Accordingly, it shows that the attenuation in signal power in the mmWave band is significantly larger than frequencies of currently used communications systems. Nevertheless, the associated technology is still very much in the academic space, and has not

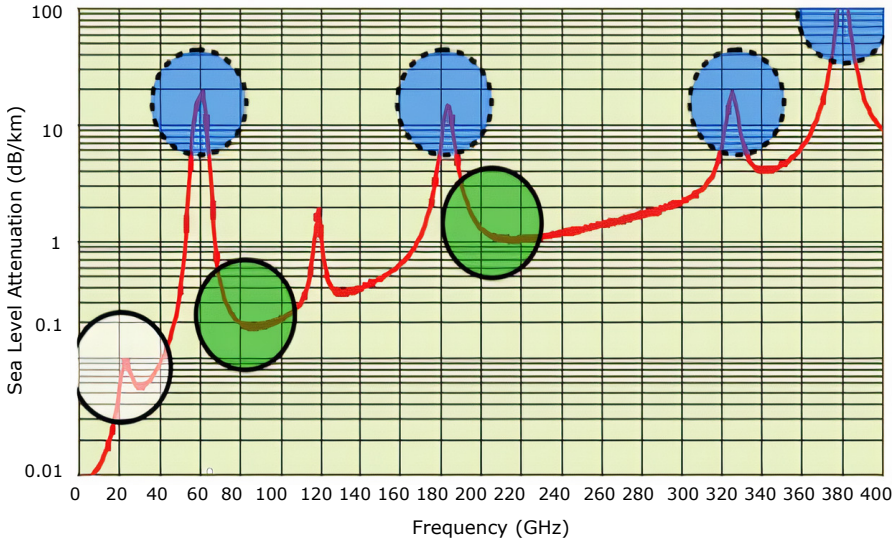

Figure 1.2: Atmospheric attenuation for mmWave frequencies [10]. The green circles highlight attenuation similar to current communication systems, i.e. the white circle. The blue circles highlight frequencies with increased attenuation [11].

yet been commercialised. As such, there is a great amount of debate about its real world capabilities. A core debate for example is that on the one hand, mmWave channels have a high path loss due to the reduction in the transmitter and receiver antenna size which is illustrated in Fig. 1.2, and also have a high sensitivity to blockage due to the frequency used. On the other hand, as the antenna dimensions are inversely proportional to the carrier frequency, it is possible to place a large amount of tiny antennas in small areas. This leads to huge possibilities in using massive Multiple Input Multiple Output (MIMO) techniques, which can provide highly directional beams, which have very high signal-to-interference-plus-noise ratios (SINR) that might overcome the high path losses.

Further, enabling connectivity amongst vehicles using mmWave, and accordingly achieving Gbps data rates, is gaining momentum as the beneficial characteristics derived from cooperative techniques, i.e. *See-Through* and *Bird's Eye View*, *safety awareness*, *adaptive platooning* or even *cloud-driven* traffic networks could be possible [5, 12] where the future of the concept is illustrated in Fig. 1.3.

To meet the extremely high data rates demanded for V2X links, utilization of the mmWave frequency band [13] has been proposed by several individual nations and unions. The Cooperative Intelligent Transport Systems (C-ITS) of the European Commission has proposed the 63 GHz and 64 GHz bands for higher capacity demand of future vehicles [14]. In the US, the Federal Communications Commission (FCC) allocated the 57–64 GHz band for unlicensed

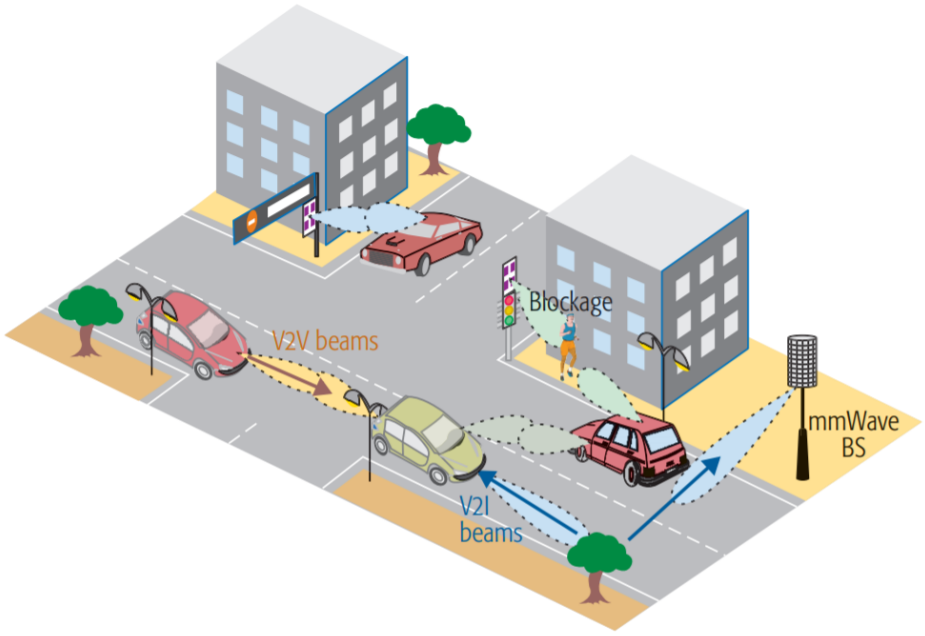

Figure 1.3: The concept of mmWave V2X communications through beam steering [5]. Multi-point communications between vehicles and mmWave base stations are possible, and a human body can act as a blockage, in addition to buildings, foliage and other vehicles.

usage [15]. In the UK, the Office of Communications (Ofcom) proposed a licence exemption for short-range wireless communications in the range of 57-71 GHz [16].

1.3 Quality Measures for Wireless Networks

So far, possible applications of mmWave V2X and the applicability and disadvantages of current communication protocols have been discussed. Four cross-cutting and crucial quality parameters of a wireless network will now be introduced, namely: Capacity, Coverage, Area Spectral Efficiency (ASE) and Connectivity. The maximum achievable data rate of link is known as the Shannon-Hartley capacity, which is given as

$$\text{Capacity} = B \log_2 (1 + \text{SINR}), \tag{1.1}$$

where

$$\text{SINR} = \frac{P_t h_o G_t G_r A d^{-\alpha}}{\sum_{i \epsilon \Phi} P_t h_i G_{i->t_r} G_{t_r->i} A r_i^{-\alpha} + N_0}, \tag{1.2}$$

where B, P_t, h_o, h_i are bandwidth, transmitter power, small-scale fading between transmitter-receiver pair, i-th interferer-receiver pair, respectively. Plus, G_t, G_r, d are antenna gains of transmitter and receiver, distance between

transmitter and receiver, respectively. Moreover, r_i, A, α, N_0 are interferer distance to receiver, path loss intercept, path loss exponent, thermal noise of electronic circuits, respectively. Further, $G_{i->t_r}$ and $G_{t_r->i}$ represents the transmitting antenna lobe gain from the i-th interferer to the receiver, and the receiving antenna lobe gain to the i-th interferer from the receiver, respectively. In addition, Φ is the point process that represents all the interfering nodes which surround the receiver. Bandwidth is a scarce source for carrier frequencies under 6 GHz, whereas there are massive unallocated bandwidths in the mmWave spectrum. However, allocation of bandwidths are pre-specified and set by national authorities and institutions, which makes capacity optimization through dynamic bandwidth allocation less favourable. Consequently, researchers typically focus on optimization of SINR in (1.1) and separately shown in (1.2). Throughout this thesis, the SINR is measured over a selected communication node, that is named *typical* receiver. In addition, the transmitter power, P_t, is assumed to be constants and equal for all the vehicles throughout the thesis.

The fading of a signal between any transmitter and receiver pair in (1.2) is classified as either large-scale fading or small-scale fading. The former estimates the path loss over large distances, i.e. > 100 m, and diffraction caused by large objects. The latter estimates the rapid fluctuations in the received signal over short distances, i.e. a few wavelengths, or over a short duration [17]. As the stochastic geometry analyzes the networks performance over the snapshots, i.e. sampling the system parameters such as locations of the nodes, path loss, antenna gain instantaneously, the impact of time-variance of the vehicular network is ignored throughout the thesis.

Several random variables and carrier frequency dependent parameters can be found within (1.2). In literature, small-scale fading is typically modelled as Rayleigh fading and Rician/Nakagami fading [17] for carrier frequencies below and above 6 GHz, respectively. Moreover, the distribution of antenna gains and the distances between the interferers and the *typical* receiver are random variables that need to be taken into account based on the network structure that is being modelled. Path loss exponents are very different at sub-6 GHz and mmWave frequencies when there are blockages, which can be modelled as another random variable.

To simplify the analytical model, the Nakagami fading is modelled with the gamma random variable $h_o \sim \Gamma(m, 1/m)$ throughout the thesis, where m is an integer. If $m \to \infty$, the small-scale fading h_o becomes a deterministic value with a mean of 1, whereas the scenario of $m = 1$ causes the most fluctuations in small-scale fading, and is equivalent to an exponential distribution which is typically used to model Rayleigh fading. The small-scale fading between the *typical* receiver-transmitter pair, h_o, and the receiver and i-th interferer,

h_i, are both modelled by the same parameter m, but represented by different symbols for analytical convenience.

In addition to capacity, optimization of SINR through the selection of half-power beamwidth, antenna gain, routing scheme etc. takes place via coverage analysis, which is the probability of the received SINR to be greater than some threshold $\mathcal{T}$, as given by

$$\text{Coverage} = \mathbb{P}(\text{SINR} > \mathcal{T}). \tag{1.3}$$

Note that in this thesis, beamwidth and half-power beamwidth are used as synonyms. In addition to capacity and coverage, throughout the generations of cellular communications, maximizing the spectral efficiency, i.e. the amount of bits transmitted per unit spectrum, has been a major focus point of research. In order to present an enhanced system level efficiency metric, that takes into account the number of vehicles and the region in which they reside, the Road Spectral Efficiency (RSE) has been proposed. RSE is defined as the average number of bits transmitted per unit time per unit bandwidth per unit road section. The analytical definition of RSE is given as

$$\text{RSE} = \frac{\lambda}{L_w} \lambda \log_2 (1 + \mathcal{T}) \, \mathbb{P}(\text{SINR} > \mathcal{T}), \tag{1.4}$$

where λ is the density of transmitter vehicles and L_w is length of lane width similar to Area Spectral Efficiency (ASE)[18]. Similar to the coverage probability, because of its inclusion of SINR, the capacity and RSE are key parameters for the analysis of vehicular communications, which can be stochastically modelled through the optimization of multiple variables.

Furthermore, since the purpose of this research is maximizing the vision of connected autonomous vehicles beyond line-of-sight, it is important to connect the head and the tail vehicles of a fleet through the vehicles in-between them. Hence, the connectivity, which counts the number of connections between the vehicles in a fleet, is another criterion that is employed in this research,and formulated as

$$\mathbb{P}_{\text{Connectivity}} (i|n) = \mathbb{P} \left(\, i \text{ links are established} | N(t) = n \right), \tag{1.5}$$

given that n vehicles exist in the fleet at a moment t.

1.4 The Stochastic Geometry Technique

The aforementioned quality measures of wireless communications typically incorporate many random variables, and accordingly cause a highly uncertain system response. In order to reduce the uncertainty of the system performance

in terms of coverage and data rate, as well as to estimate the impact of channel properties and interferers in mmWave vehicular networks, typically ray-tracing [19], discrete-event simulators [20, 21], and the tools of different analytical methods have been utilized. Whereas such simulators provide solid conclusions from a given set of input parameters after numerical iteration, they fail to draw the mathematical relations between each parameter, and thus lack a capability to provide analytical relationships between parameters. As a result, researchers have focused on different analytical tools to provide an insightful analysis.

Analytical models can be classified into two categories, namely deterministic and stochastic. The Wyner model is a commonly used example for deterministic modelling, which follows the Wyner method [22] and fixes the locations of users in a homogeneously distributed manner to present tractable results. By means of Monte Carlo simulations [23], it has been shown that in the case of uplink communications for a sufficient number of users, the Wyner model provides an accurate performance [24]. However, for downlink communications the Wyner model is rather inaccurate. Even though, it presents more complex analytical results, stochastic modelling is a growing trend in academic literature. With an ambition to reveal underlying analytical relationships, researchers are turning to stochastic geometry methods as a core methodology to capture the stochasticity of wireless networks.

Stochastic geometry presents a way of characterizing and computing insightful properties in a tractable manner, by averaging over all potential geometrical realizations for the wireless network [25]. Furthermore, stochastic geometry is built on random point processes, a collection of random variables in a mathematical space. The most common point processes are variants of the Poisson Point Process (PPP), in which the points in are distributed with the probability distribution function of Poisson. Alternatively, in the Binomial point process (BPP), the number of points in a space are distributed with the Binomial distribution. Those variants can be classified by their distribution on a plane, namely, homogeneous, clustered, or repulsive. In the homogeneous class, points on the plane are distributed uniformly, with a typical variant being the homogeneous Poisson point process. Alternatively, the Poisson clustered process (PCP) and the Matern hard core point process (MHCPP) are typically used to model clustered and repulsive point processes, respectively. In this thesis, the original and a modified homogeneous PPP are used as they yield tractable results. Moreover, all results of the derived analytical models are compared and verified with Monte Carlo simulations due to their simplicity in application, which provides a good indication of the models' accuracies.

To the best of the author's knowledge, so far, no stochastic geometry model has been specifically designed for mmWave V2V networks, taking into account appropriate small-scale fading, antenna gains and their alignment probabilities,

node distribution, and both a channel and a blockage model. Hence, stochastic geometry will be the foundation of this thesis.

1.5 Thesis Outline

Motivated by the above reasons, the quality of mmWave communications for CAV applications is evaluated in this thesis, primarily through the quality measures of coverage; rate coverage as a metric of capacity; ASE; and connectivity. Practical issues around mmWave communications in the CAV application context are also examined and included to maximise the impact of the research herein. Tractable, and where possible, closed-form mathematical derivations supported with numerical results are provided to enable the discussion and subsequent analysis.

In Chapter 2, a background chapter is provided that classifies different stochastic geometry models, path loss measurements in mmWave channels, and probabilistic blockage models from existing academic literature. In addition, it defines a general relationship between antenna gains, beamwidth and angular alignment error. Further, it ranks the modelling of small-scale fading in terms of its complexity and accuracy. Finally, several characteristic tools of stochastic geometry are presented that are utilized throughout the thesis.

In Chapter 3, the coverage is modelled using a grid-like representation of the city layout, and the impact of types of road structure, for instance crossings and parallel roads, is investigated. This simplified model is proposed to reduce the complexity of the analytical model. This chapter reveals the key factors that effect the coverage performance. Firstly, the impact of antenna placement on vehicles and the blockage effect of the surrounding vehicles are discussed. Secondly, the relationship between the direction in which vehicles point their beams and the level of interference that the *typical* receiver suffers is investigated. Thirdly, the trade-off between antenna gain and beam alignment probabilities are discussed. Furthermore, the coverage performance of existing vehicular communications protocols is compared to mmWave vehicular communications and analysed for a scenario in which each vehicle participates in communications simultaneously. Through investigation and analysis, this chapter sheds light on the possible challenges of mmWave vehicular communications and becomes a guide for the following chapters. The key results of this chapter have also been presented in IEEE Communications Letters [26].

Building on the coverage model for a single-lane road in Chapter 3, which presents an analysis for individual pairs of transceivers, Chapter 4 approaches the quality of mmWave communications on such road from a holistic perspective which is named connectivity in this thesis. Moreover, a measurement-based model for the lateral displacement of in-lane vehicles is proposed. Hence, the

relationship between the reciprocal beam alignment of a receiver-transmitter pair and the in-lane lateral displacement of vehicles is analysed. Secondly, using the tools of geometric probabilities and stochastic geometry, a SINR-based critical transmission range for mmWave vehicular communications is modelled. This range determines if a receiver vehicle is in a reachable distance from a transmitter. Thereafter, the beam misalignment probability and critical transmission range are combined into one model and their interdependence is investigated. This chapter presents a beamwidth adjustment strategy that optimizes connectivity for different vehicles densities and road curvatures. The key results of this chapter have also been presented at the flagship conference of IEEE GLOBECOM 2019 [27].

Chapter 5 investigates the mean interference for the *typical* receiver on a two-lane road layout for various routing schemes. By building on Chapter 3, the impact of routing schemes and beamwidth is analysed in detail, and the number of adjacent lanes is gradually increased. Two baseline routing schemes are analysed, namely the in-lane and the closest vehicle routing scheme. Since homogeneous PPP allows points to be very close or even to be on top of each other, this contradicts with the real-world distribution of vehicular traffic. Hence, this chapter addresses it by utilizing the headway distance specifications for platooning. Additionally, a framework is presented that compares two routing schemes for different vehicular densities. Finally, by means of investigating different antenna gain alignments, the analytical model is further simplified. The key results of this chapter have also been prepared to be submitted.

Chapter 6 builds on the motivations and methodologies of Chapters 3 and 5, presenting the coverage probability, rate coverage and road spectral efficiency for a four-lane road layout under an in-lane routing scheme. In addition to taking account the impact of routing behaviour and the increased number of lanes, the presented model gains realism through the addition of the blockage impact of vehicles that are located in adjacent lanes. Furthermore, this impact is diversified for different path loss characteristics, namely, LOS (Line-of-Sight), OLOS (Obstructed-Line-of-Sight) and NLOS (Non-Line-of-Sight). Finally, the interdependencies of antenna gain, beamwidth and the received interference will be interpreted. The key results of this chapter are currently also under review in Elsevier Vehicular Communications.

Chapter 7 concludes this thesis through summarising the research and detailing its envisaged impact. Potential future work is also proposed, which includes guidance on the expansion of the connectivity quality measure into multi-lane scenarios. As future work, the multi-lane coverage analysis could be enhanced for the alternative routing schemes. Furthermore, the trade-off between different routing schemes in terms of rate, latency and sustainability

of network topology is another direction to be explored. Moreover, different beamwidth optimization schemes and the impact of co-existing autonomous and conventional vehicles on the wireless communications system performance could also be investigated.

The most important contributions of the thesis from a system level point of view could be summarized as follows:

- It has been shown that mmWave V2V communications provides fairly comprehensive performance as a system, even if any interference mitigating techniques are not implemented. Moreover, use of mmWave amongst vehicles provides significantly better data rate compared to off-the-shelf protocols.

- It is found that the system performance is heavily affected by the vehicles located in their own lane and adjacent lanes, and limited by the LOS and main-to-main antenna lobe aligned interferers. Further, the coverage performance of mmWave V2V networks are density-insensitive.

- It is revealed that there is a beamwidth optimization regime to maximize connectivity in a single lane mmWave V2V network for different vehicular densities and road curvatures.

- Inserting a platooning based headway requirement as a hardcore separation between subsequent vehicles into homogeneous Poisson Point Processes to model the distribution of autonomous vehicles provides fairly realistic results.

Chapter 2

Review of Stochastic Geometry and Vehicular mmWave Communications

In this chapter, the current state-of-the-art thinking in mmWave channel modelling, V2V communications and their intersection in stochastic geometry is presented. In addition, this chapter summarizes various approximation techniques for small-scale fading, blockage modelling, antenna gain and beamwidth relationship models known in the field.

In general, stochastic geometry has been used to model performance of cellular and device-to-device networks. For instance, [28] stochastically modelled uplink performance of cellular network using stochastic geometry and compared the resulting model with deterministic technique. Furthermore, [29] has modelled downlink SINR distribution of heterogenous cellular network. Plus, [30] has investigated the relationship between offloading and resource allocation among macrocells and small cells to improve rate of cell edge users. Moreover, [31] has modelled the offloading from cellular to Wi-Fi by using two Poisson point processes to reveal optimum traffic offloading for maximization of SINR and rate coverage. In addition, [32] has derived coverage probability and energy efficiency of homogenous and heterogenous cellular network for different sleeping policies of macrocells. Plus, [33] has modelled outage probability for heterogeneous cellular networks with flexible cell association. Moreover, [34] has modelled orthogonal and non-orthogonal spectrum sharing between device-to-device and cellular networks. Similarly, [35] has investigated the cognitive radio based device-to-device communications under cellular networks for random spectrum access and prioritized spectrum access policies. Furthermore, [36] has proposed a random network model for a device-to-device communications underlaid cellular network by utilizing stochastic geometry and develops centralized and distributed power control algorithms.

Table 2.1: Comparison of mmWave or V2V stochastic geometry models

Ref.	**Small-Scale Fading / Path Loss Model**	**Blockage Model**	**Radio Access Technology**	**Node Distribution**
[37]	Nakagami / CI mmWave Path Loss Model	LOS-Ball Method	mmWave Cellular Networks	2-D Homogeneous PPP
[23]	Rayleigh / CI mmWave Path Loss Model	Two-Ball Method	mmWave Multi-Tier Celullar Networks	2-D Homogeneous PPP
[38]	Nakagami / CI mmWave Path Loss Model	LOS-Ball Method	mmWave Dense Cellular Networks	2-D Homogeneous PPP
[39]	Nakagami / CI mmWave Path Loss Model	Distance-Dependent LOS Probability	mmWave Ad Hoc Networks	2-D Homogeneous PPP
[40]	Nakagami / CI mmWave Path Loss Model	LOS-Ball Method	mmWave D2D Networks	2-D Thomas Cluster Process
[41]	Rayleigh / CI mmWave Path Loss Model	Street Orientation Dependent LOS Model	mmWave Cellular Networks	1-D Homogeneous MPLP / Cox
[42]	Rayleigh / Standard Path Loss Model	None	DSRC V2V Networks	1-D Homogeneous PPP / Vehicular
[8]	Rayleigh - Nakagami CI mmWave Path Loss Model	Large Vehicles Dependent Probability	mmWave V2I Networks	1-D Homogeneous PPP / Vehicular
[43]	Rayleigh / Standard Path Loss Model	None	DSRC V2V Networks	1-D Non/Homogeneous PPP / Vehicular

Neverthless, the aforementioned well-known works do not adress specifically mmWave vehicular communications. Accordingly, Table 2.1 is presented to summarize the current leading literature on stochastic geometry models for mmWave and vehicular communications, and classify them based upon channel models, blockage models, radio access technologies, and node distributions. Clearly, Table 2.1 shows that there is no specifically designed analytical model for mmWave V2V communications that takes into account the path loss model, blockage model, radio access technology and the node distribution. Moreover, it can be inferred that there are still open research questions on the exact modelling of interferences caused by surrounding vehicles located in different lanes on urban roads, and how blockages affect the system performance.

Stochastically, coverage modelling of wireless networks depends on several assumptions. For instance, the classification of these models is based on blockage modelling, directionality of antenna beams, carrier frequency, clustering of nodes, and/or by their applicability to either ad hoc or cellular type networks. Since radio wave propagation at mmWave frequencies differs significantly for LOS and NLOS cases, researchers are driven to propose different blockage models for all these different scenarios.

2.1 Channel Characteristics of mmWave Propagation

The propagation path loss, $\mathcal{P}_L$, of mmWaves has been modelled using various mathematical models. These mathematical models include several parameters such as the 3-D Euclidean distance between transmitter and receiver, antenna heights, directionality of antenna beams, and density of obstructions. One of the most commonly implemented propagation path loss models for mmWave, is the close-in (CI) path loss model [45], described by

$$\mathcal{P}_L[dB] = \mathcal{P}_L(d_0) + 10\alpha \log_{10}(d/d_0) + X_{\sigma_m}, \text{ for } d \geq d_0, \tag{2.1}$$

where $\mathcal{P}_L(d_0)$ is the CI free space path loss (FSPL) in decibels at a separation distance of d_0 between the transmitter and receiver pair. $\mathcal{P}_L(d_0)$ is considered as the immediate path loss after the beam leaves the antennas in free space and anchor point in order to standardise all measurement campaigns. It is typically formulated as

$$\mathcal{P}_L(d_0) = 10 \log_{10} \left(\frac{4\pi f_c d_0}{c} \right)^2, \tag{2.2}$$

where d_0 is usually taken as 1 m. Also, c, f_c, and d are the speed of light, carrier frequency and distance between transmitter and receiver, respectively.

In addition, α is the path loss exponent that is obtained from a minimum mean square error (MMSE) fit to a large data set resulting from various measurement trials. X_{σ_m} is a zero-mean Gaussian random variable with a standard deviation of σ_m in dBs. It is used to model large-scale signal fluctuations due to large obstructions between the transmitter and receiver [44]. Throughout the thesis, the deviation in the path loss models is ignored for the analytical convenience.

Alternatively, other proposed path loss models, such as the floating intercept, or alpha-beta-gamma model stated in (2.3) forms part of the 3GPP WINNER 2 model [46, 47] formulated as

$$\mathcal{P}_L[dB] = 10\alpha \log_{10}(\frac{d}{d_0}) + \beta + 10\gamma \log_{10}(\frac{f_c}{1 \text{ GHz}}) + X_{\sigma_m}. \tag{2.3}$$

In (2.3), α and γ are coefficients that represent the dependence of path loss on distance and frequency, respectively, β is an optimized offset value for path loss in dB, and X_{σ_m} is a zero-mean Gaussian random variable with a standard deviation of σ_m [48]. The advantage of this model is that it provides a realistic best fit to measured data using least-squares regression [11]. However, it is only valid for the scenario types on which the measurements have focused, and is less applicable in new scenarios not previously considered as key to commercial deployment.

Table 2.2 summarizes typical path loss exponents and standard deviations of both LOS and NLOS cases for mmWave V2V and Peer-to-Peer (P2P) communications to be used in (2.1). In Table 2.2, the column named NLOS-best contains the lowest measured path loss for a single antenna beam at both the transmitter and receiver [44]. Note that, the path loss exponent in Table 2.2 differs a lot between LOS and NLOS cases. Therefore, this determines that the coverage and connectivity modelling of mmWave communications must be handled differently for LOS and NLOS cases. Throughout the thesis, (2.1) and the channel parameters in Table 2.2 are converted to use Watt as the unit of power. In addition, the fundamental difference between V2V and conventional

Table 2.2: Measurement-based path loss parameters for mmWave vehicular and P2P networks [44] with σ_m in dB and distances in meters.

P2P Directional Path Loss Models (d_0 = 1 m)								
			LOS		NLOS		NLOS-best	
Freq.	Tx height	Rx height	PLE	σ_m	PLE	σ_m	PLE	σ_m
38 GHz	1.5 m	1.5 m	2.0	3.8	3.9	10.6	3.3	7.7
60 GHz			2.2	2.0	3.6	9.0	3.3	9.2
V2V Directional Path Loss Models (d_0 = 1 m)								
			LOS		NLOS		NLOS-best	
Freq.	Tx height	Rx height	PLE	σ_m	PLE	σ_m	PLE	σ_m
60 GHz	1.5 m	1.5 m	2.5	3.5	5.4	14.8	5.0	10.9

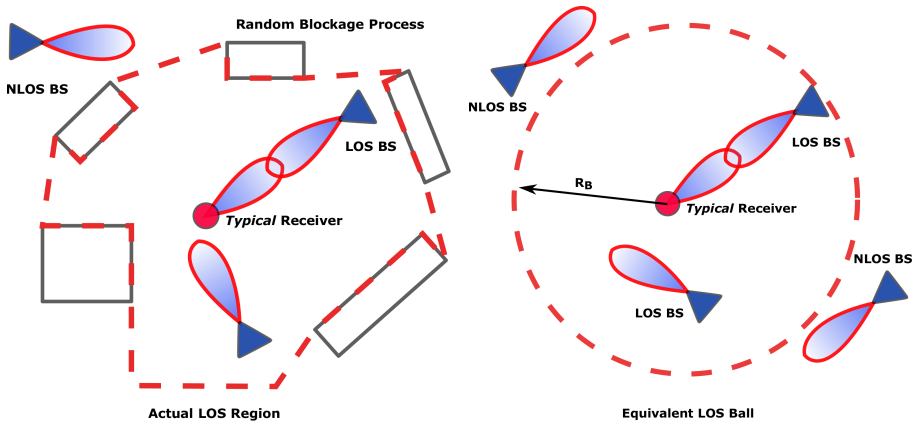

(a) Actual LOS region (b) LOS ball

Figure 2.1: mmWave LOS ball method classification [37] with (a) an irregular shape of an actual LOS region in-between buildings that are modelled as another random process, (b) Approximation of the LOS region using LOS ball method.

channel models is the Doppler shift due to the mobility of vehicles. Doppler shift and coherence time characterize fading speed and frequency selectiveness [49]. For instance, the maximum Doppler shifts of V2V channels are in the range of 10 Hz - 20 kHz when the carrier frequency is in the range of 3 - 60 GHz [50, 51]. However, those results are based on omnidirectional links, whereas [52] states that directional beams decrease the Doppler shift. Moreover, the use of an automated frequency control (AFC) loop at the receiver side can significantly compensate a Doppler shift [51]. Therefore, in this thesis and similar to [8], the effect of mobility on performance, i.e. Doppler shift, is not taken into account in the mathematical derivations.

Given that significant path loss differences exist between LOS and NLOS channels, it is also necessary to differentiate between LOS and NLOS interferers in the analytical model. Accurate modelling of the blockage that is caused by an NLOS link has recently been explored in the academic literature. For instance, [37] proposes the LOS ball method, which assumes that all the nodes within a specific radius from the receiver are assumed as LOS, with the rest of the nodes classified as NLOS interferers, as is illustrated in Fig. 2.1. The radius of the LOS ball is adjusted so that it includes the same average number of LOS base stations in the network as a receiver can see. Due to the linear distribution of vehicles in traffic, the LOS ball blockage classification is not suitable for modelling blockage in vehicular terms. In contrast, in mmWave V2V communications, the surrounding vehicles are the cause of blockage and interference. This makes mmWave V2V communications fundamentally different from mmWave ad hoc and cellular communications.

Alternatively, [39] proposes a probabilistic LOS model where the probability

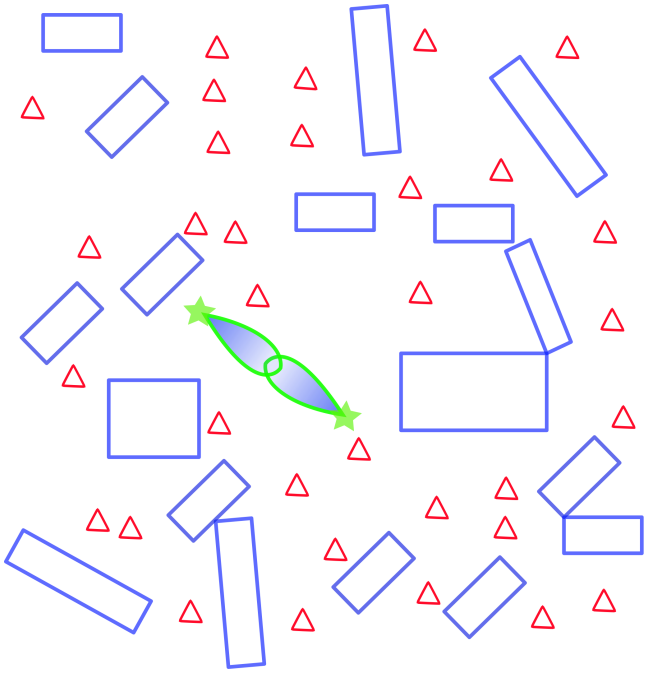

Figure 2.2: LOS model depending on communications distance and density of buildings [39], where green stars are the *typical* receiver and transmitter pair, and red triangles and blue rectangles are interferers and blockages, respectively.

of being a LOS link exponentially decreases with distance from the typical receiver and transmitter pair as shown in Fig. 2.2. In this method, the buildings, i.e. the source of blockage, are modelled as another PPP, and each point in the process is independently marked by width, length and orientation. In other words, each point in the process is modelled as the center point of rectangular random shape and marked with random width,W_b , and length, L_b. Hence, the probability of establishing a LOS link in an outdoor environment [53] is $\mathbb{P}_{\text{LOS}} = e^{-\beta_b d}$, where d is the communications distance and β_b is given as

$$\beta_b = \frac{2\lambda_b \left(\mathbb{E}\left(W_b\right) + \mathbb{E}\left(L_b\right)\right)}{\pi}, \tag{2.4}$$

where λ_b is the density of buildings of PPP, and $\mathbb{E}\left(W_b\right)$ and $\mathbb{E}\left(L_b\right)$ are the expected values for the average width and length of the buildings, respectively. Obviously, this widely used blockage model is designed for a city-layout and cellular communications, and does not meet the unique requirements of mm-Wave vehicular communications, such as the distribution of vehicles, and the blockage impact of in-lane and adjacent lane vehicles.

On the other hand, [8] proposes a probabilistic LOS model based on the density of large vehicles and the number of lanes for use as a V2I coverage model, as shown in Fig. 2.3. Yet, this large vehicle dependent model is specifically designed for V2I communications and does not take into account V2V communications, which is the topic of interest in this thesis. Hence, a

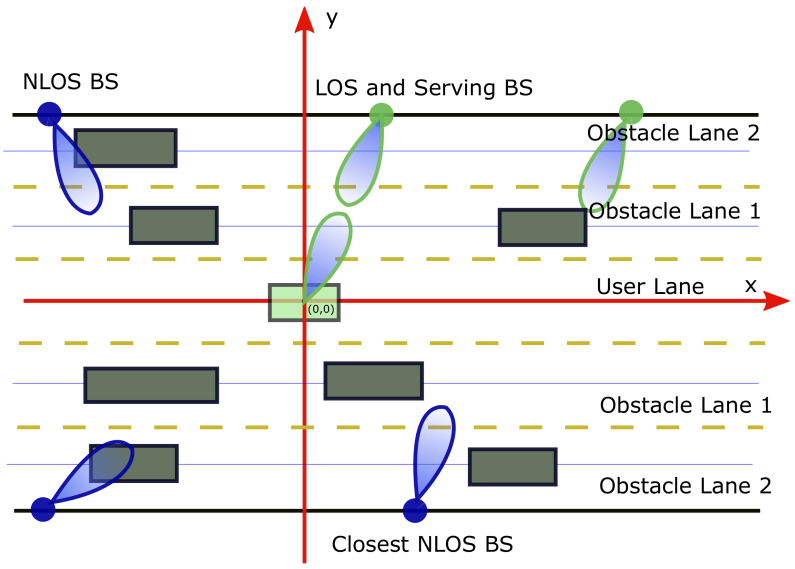

Figure 2.3: Lane and large vehicle dependent mmWave LOS model [8], where the dark rectangles represent large vehicles. The central lane is modelled as the user lane in which no large vehicle blockages exists.

stochastic geometry based blockage modelling for mmWave vehicular networks is required.

Finally, whereas it is possible to extend the vision of CAVs through the combination of vehicle-to-infrastructure and infrastructure-to-vehicle communications, this would push system designers to equip both vehicles and road side units (RSUs) with mmWave transceivers. Even though communications with RSU infrastructure have their own advantages, it will increase the total cost, since for mmWave V2V communications it is sufficient to only equip the vehicles with mmWave transceivers.

Table 2.3: Comparison of Nakagami small-scale fading models

Methods	Approximation Level	Tractability	Closed-Form
Gil-Pelaez Inversion Theorem [54]	Exact	Low	No
Hamdi's Lemma [55]	Exact	Medium	No
Faà Di Bruno's Lemma [56]	Exact	Low	No
Alzer's Lemma [57]	Approximation	High	Yes
Treat as Rayleigh	Approximation	High	Yes

2.1.1 Wireless Network Modelling Techniques in Literature

One of the main steps in the derivation of a coverage probability is the modelling of small-scale fading. Whereas, in stochastic geometry literature, the small-scale fading is modelled with either an exponential random variable, or gamma random variable for sub-6 GHz and mmWave frequencies, respectively. Table 2.3 summarizes techniques to model Nakagami small-scale fading in terms of their complexity and accuracy. The modelling of Nakagami fading is carried out using the Gil-Pelaez Inversion Theorem [54], Hamdi's lemma [55], and Faà di Bruno's lemma [56]. For tractability reasons, Alzer's lemma [57] is also used within this thesis.

Academic literature has proposed several methods to overcome the mathematical challenges of stochastic geometry analysis of wireless networks. Firstly, limiting the model by only considering the most dominant n interferers, is a widely used approach to reduce the complexity. Typically, the nearest [58] or the strongest interferer n nodes are taken into account to provide a lower bound on performance modelling. Secondly, the probability distribution function of the aggregate interference power is approximated with commonly used distributions, such as Gaussian and shifted log-normal distributions [59]. Nevertheless, currently no standard exists on how to choose the optimal distribution [60]. Thirdly, the use of the Plancherel-Parseval theorem evaluates the distribution of the aggregate interference by integrating the Fourier Transform of an interference's distribution [61]. Even though this technique provides exact results, it complicates the model and causes the loss of tractability, which is the major advantage of stochastic geometry.

2.2 Antenna Gain Modelling

As steering of directional antenna beams is proposed to overcome high path loss and the impact of blockages, it is necessary to present a model that describes the relationship between antenna beamwidth and the antenna gain. Thus, the main lobe antenna gain, G_m, and side lobe antenna gain, $0 < g_s \leq 1$, are used to express such directional beam steering [62]. Hence, the general formula for the antenna alignment and beamwidth dependence of the gain is given as

$$G_{i->j} = \begin{cases} G_m = \frac{2\pi - (2\pi - \phi)g_s}{\phi}, & \text{if } |\theta_{i->j}(\sigma)| \leq 0.5\phi, \\ g_s, & \text{otherwise.} \end{cases} \tag{2.5}$$

with ϕ the half-power beamwidth as illustrated in Fig. 2.4. $\theta_{i->j}(\sigma)$ is the alignment angle error in angular degrees between the i-th transmitter and j-th receiver. Further, Fig. 2.5 shows the relationship of the beamwidth and the alignment error where the boresight is the centre of the main lobe. If the angle

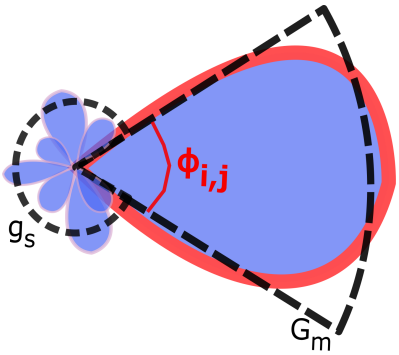

Figure 2.4: Visual representation of a sectored antenna gain model, and main and side lobe gain in relationship to the half-power beamwidth. Note that, an actual antenna pattern is simplified with the sectored model.

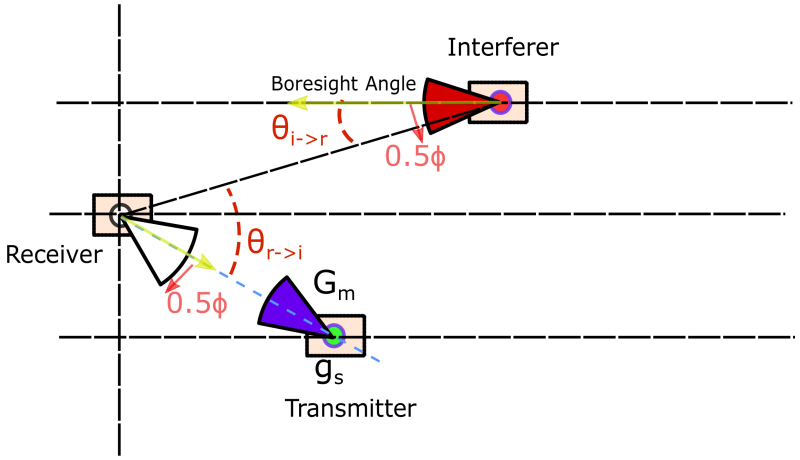

Figure 2.5: Illustration of the antenna alignment and potential interference. The rectangles and dashed lines represent vehicles and centres of the lanes, respectively.

between the boresight of the interferer and the location of the receiver, $\theta_{i->r}$, is smaller than 0.5ϕ, the interferer interferes with the receiver through the main lobe gain. Similarly, if the angle between the boresight of the receiver and the location of the interferer, $\theta_{r->i}$, is larger than 0.5ϕ, the receiver multiplies the signal strength of the interferer with its side lobe gain.

Hence, this leads to four different beam alignment scenarios between an interferer and the receiver, namely, main-to-main (G_mG_m), main-to-side (G_mg_s), side-to-main (g_sG_m) and side-to-side (g_sg_s) lobe alignment. Because the main-to-side and side-to-main scenarios are mathematically equivalent, three independent alignment scenarios remain.

The next step is to realistically model the probability of the aforementioned alignment probabilities. Considering that mmWave V2V communications typically take place between vehicles that are located in the same or adjacent lanes, this causes the alignment angle between the vehicular antennas to

depend on the ratio of the lane width and distance in the direction of travel between the vehicles. Given that this ratio is quite small because the horizontal distance between the vehicles is much larger than the lane width, the alignment angle will be small too. It is assumed that a vehicle wants to communicate with another vehicle in front of it or to its rear. It is also assumed that a vehicle will less likely communicate with RSUs and pedestrians. Hence, it is likely that the boresight angle distribution will accumulate near 0° and 180°. This causes the aforementioned alignment cases, G_mG_m, G_mg_s, g_sg_s to have different probabilities. To address this, the density of interferers is thinned with the probabilities that represent the lobe alignment probabilities. For the most dominant interference probability case G_mG_m, that is $\mathbb{P}_{G_mG_m}$. This is a function of the node's beam misalignment angle $\theta_{i->j}(\sigma)$, which is a random variable distributed two-peak truncated normal distribution, with its probability distribution function illustrated in Fig. 2.6, as described by

$$\mathbb{P}_{G_mG_m} = \frac{1}{2}\int_{-\frac{\phi}{2}}^{\frac{\phi}{2}} \frac{\frac{1}{\sqrt{2\pi}} e^{\frac{-x^2}{2\sigma^2}}}{\frac{\sigma}{2}\left(\operatorname{erf}\left(\frac{\pi/2}{\sqrt{2}\sigma}\right) - \operatorname{erf}\left(\frac{-\pi/2}{\sqrt{2}\sigma}\right)\right)} dx \tag{2.6}$$

where

$$\operatorname{erf}(z) = \frac{2}{\sqrt{\pi}} \int_0^z e^{-t^2} dt.$$

Thus, two truncated normal distributions with standard deviation σ, and zero-mean and π-mean, respectively, are combined. $\mathbb{P}_{G_mG_m}$ is normalized through dividing the distribution by 2, because of the combination of two equivalent truncated normal distributions. Therefore, with this model, a parametric angular error model is proposedin Fig. 2.6 which illustrated the relationship between probability distribution function (PDF) and alignment angle error, in order to cover different communications scenarios, in which the increase of σ corresponds to an increase in inter-lane V2V or V2I communications.

2.3 Tools of Stochastic Geometry

In order to provide a basis for point processes and stochastic geometry which are employed throughout the thesis, this section describes a selection of characteristics.

1. **One-dimensional PPP:** The definition of 1-D PPP [63] with uniform density λ is a point process in Euclidean space $\mathbb{R}$ such that for every bounded range $[a, b)$, $N([a, b))$ has a Poisson distribution with mean $\lambda(b - a)$, where N is the number of points in the given interval:

$$\mathbb{P}(N([a, b)) = k) = e^{-\lambda(b-a)} \frac{(\lambda(b - a))^k}{k!}. \tag{2.7}$$

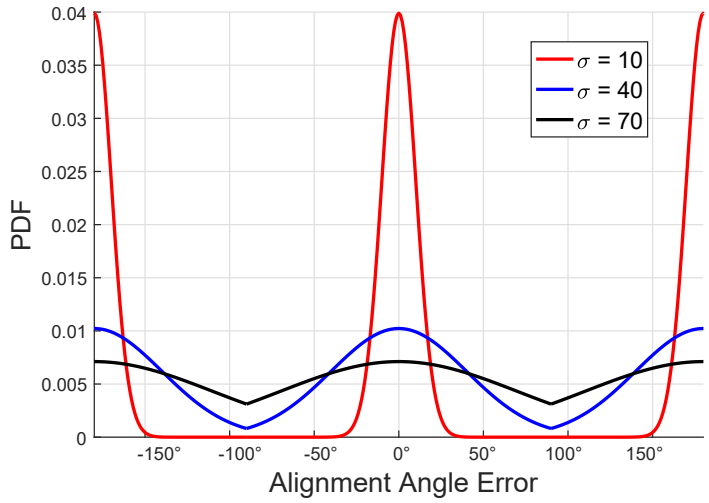

Figure 2.6: The relationship of the alignment error between the transmitter and receiver pair and its probability distribution function for different standard deviations σ.

2. **Slivnyak-Mecke's Theorem:** For a PPP,

$$\mathbb{P}_o^! \equiv \mathbb{P}, \tag{2.8}$$

which is equivalent to the reduced Palm distribution of a PPP corresponding to the distribution of the PPP itself, i.e. it states that an extra point added to the point process does not change the distribution of the other points of the PPP [64]. Similarly, removing a node does not change the statistical characteristics of the PPP. This property enables deleting the corresponding transmitter of the *typical* receiver from the process, or conditioning that the *typical* receiver is located at the centre of the coordinate system, without this having an effect on the statistical modelling.

3. **Independent Thinning:** Given that Φ is a PPP, independent thinning is the random removal of points from the process with a probability of p. The resulting point process after the removal operation is still a PPP. This property becomes significantly useful when the LOS/NLOS and different alignment probabilities of the interferers are independently classified.

4. **Superposition:** Given that $\Phi_1,...\Phi_i$ are i independent homogeneous PPPs, with densities of $\lambda_1,...\lambda_i$, respectively, the union of all PPPs, $\cup_{j=1}^{I}\Phi_j$, is another homogeneous PPP with density $\lambda = \sum_{j=1}^{I}\lambda_j$. This property is typically used for multi-tier cellular communications, and also enables the union of previously separated PPPs for LOS/NLOS and

antenna alignment probabilities.

5. **Displacement:** If the points of a PPP are randomly and independently displaced by a transformation matrix, the resulting point process is another PPP. Mathematically, if a translation matrix, M_{x_i}, is applied to a PPP, Φ, the resulting PPP will be

$$\bar{\Phi} = \{x_i \quad \epsilon \quad \Phi : x_i + M_{x_i}\}. \tag{2.9}$$

   The mobility of vehicles inherently causes a displacement of points, hence this makes the application of a PPP a suitable process in the vehicular domain.

6. **Campbell's Theorem:** Given that Φ is a stationary PPP with density λ on Euclidean space $\mathbb{R}^d$ with dimension d, for non-negative f Campbell's theorem [65] then states that

$$\mathbb{E}\left(\sum_{x \epsilon \Phi} f(x)\right) = \lambda \int_{\mathbb{R}^d} f(x)\, dx, \tag{2.10}$$

$$\text{var}\left(\sum_{x \epsilon \Phi} f(x)\right) = \lambda \int_{\mathbb{R}^d} f^2(x)\, dx. \tag{2.11}$$

   This property provides a solution for the sum of the interfering powers of each interferer in the network after being subject to path loss.

7. **Probability Generating Functional (PGFL):** Given that Φ is a stationary PPP with density λ on $\mathbb{R}^d$, for non-negative f PGFL [64] then states that

$$\mathbb{E}\left(\prod_{x \epsilon \Phi} f(x)\right) = e^{-\lambda \int_{\mathbb{R}^d} (1 - f(x)) dx}. \tag{2.12}$$

   This delivers a solution for the product of the interfering power of each interferer in the network after being subject to path loss.

8. **Moment generating function (MGF) of aggregate interference:** It presents a mathematical substitute to calculate the moments of a random variable instead of handling directly with probability density functions or cumulative distribution functions. The analytical formulation is presented as

$$M_I(s) = \mathbb{E}\left(e^{-sI}\right), \tag{2.13}$$

   where I and s are the sum interference and a dummy variable, respectively. The general expressions of $M_I(s)$ for several different point processes are given in [63]. If evaluation of the mean and variance of a random variable is not straightforward, then the model can be simplified by taking

derivatives of a moment generating function of the random variable. Then, the mean and variance of I can be calculated as

$$\mathbb{E}(I) = \frac{dM_I(s)}{ds}|_{s=0}, \tag{2.14}$$

$$\text{var}(I) = \frac{d^2M_I(s)}{ds^2}|_{s=0}. \tag{2.15}$$

.

2.4 Conclusions

Given the potentially high socio-economic impact that CAVs may entail, and the subsequent motivation to thus enhance their connectivity provisions, this chapter has methodically identified:

- An absence from within the community for the provision of a stochastic geometry based model that is specifically designed for mmWave V2V communications.
- That furthermore, whilst various incumbent models exist, they may only account for some specific aspects of the channel or scenario, and none accommodate a more holistic, measurement-supported, accountability of path loss model, blockage models, directional beam forming and node distribution.

Thus, over the following chapters, I will build upon this foundation, and contribute new knowledge related to the acceleration of mmWave V2V communications utilizing the tools of stochastic geometry.

Chapter 3

A Grid-based Coverage Analysis of Urban mmwave Vehicular Ad Hoc Networks

In this chapter, a tractable coverage model, specifically designed for urban vehicular ad hoc networks, is presented to aid a better system design. This is achieved through the use of a model based upon grid lines, which simplifies the analysis. This chapter sheds a light on the criteria that affect the performance of mmWave V2V communications. It is found, that even in scenarios with a large number of interferers, mmWave vehicular communications can establish reliable links with a SINR threshold of around 5 dB, with a coverage probability of approximately 0.8 at 50 m separation between a *typical* transmitter and a *typical* receiver where *typical* adjective corresponds to selected transmitter and receiver pair that system performance is measured over. These results, and their inference towards the design and deployment of an urban vehicular ad hoc network (VANET), are critical to the development of future V2V applications and services.

Further, this chapter examines mmWave V2V communications from a city level perspective. According to the analysis presented in this chapter, mmWave V2V communications are sensitive to the routing behaviour of vehicles, the blockage characteristics of the metallic bodies of vehicles and the transceiver antennas' half-power beamwidths. It will also be shown, that reducing the complexity of the problem from a city-layout to a multi-lane single road, provides a significant simplification in modelling and highly accurate results as is confirmed by comparison with Monte Carlo simulations.

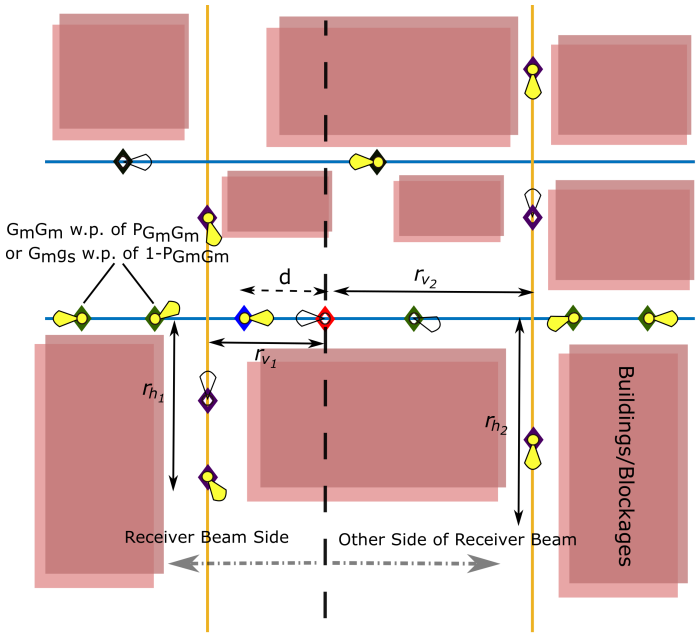

Figure 3.1: Graphical representation of the proposed PPP-distribution of vehicles roads in a grid-based city layout. The *typical* receiver and transmitter are depicted as red and blue diamonds, respectively. The neglected, own lane and vertical lane interferers are represented as black, green, and purple diamonds, respectively. The yellow and white beams illustrate the transmitting and receiving vehicular antennas, respectively.

3.1 Introduction

Intuitively, urban ad hoc vehicular communications networks can only exist within the bounded urban corridors formed along the roads by buildings, foliage etc. Empirical evidence for the strong influence of the urban corridor on the coverage of the transmitter has been provided by measurements in [66], performed at a carrier frequency of 55 GHz and involving a transmitter antenna with a 10° beamwidth installed on the top of a building and a mobile receiver vehicle with a 20° beamwidth. Strong signal propagation is limited to the street in which the transmitter is installed and the streets at right angles to this street, whereas propagation at parallel streets is negligible [66][67]. Hence, within this chapter, the signal propagation at the road of interest and vertically intersected roads are taken into account whereas signal propagation from the parallel roads to the road of interest is neglected as illustrated in Fig. 3.1.

Another challenge in mmWave V2V communications that needs to be addressed, is the modelling of NLOS effects due to obstructing vehicles between the *typical* transmitter and receiver. According to measurements carried out at 77 GHz in [68], an obstructing vehicle has no effect on the communication as gap between the vehicle's under-body and the road surface forms a wave-guide. Contrary to that conclusion, measurements carried out at 60 GHz in [69] state

that an obstructing vehicle could cause a typical 8 dB additional path loss, which corresponds to a 6.3 times smaller signal. This contradiction is probably caused by these measurements being carried out under different conditions, such as carrier frequency, antenna placement, beamwidth. For this reason, two different coverage models are proposed in this chapter which have been peer-reviewed by the IEEE community, based on two different measurement results. Moreover, this chapter applies a grid-based distribution to model V2V communications in urban ad hoc networks, thereby defining a tractable coverage model for mmWave vehicular communications, which:

- is based on the Manhattan distance to represent the distance between the *typical* transmitter, *typical* receiver and interferers, which is the sum of the vertical and horizontal grid components. Rather than using Euclidean distance, it has been shown in [70] that path loss in an urban environment is closely related to the graph/Manhattan distance and street oriented path loss models for mmWave communications are proposed.

- models that LOS and NLOS separation takes place when the receiver-transmitter distance is larger than the inverse of the density of vehicles per line, λ^{-1}. This is considered as the first case of interest herein, and will be referred to as *LOS-NLOS*.

- models LOS and NLOS links for vehicular communications based upon a grid-based distribution, where vehicles on the same line have LOS communications links and line-to-line communications are defined by NLOS links. This is considered to be the second case of interest herein, and will be referred to as *LOS-always*.

By considering both cases of interest, (*LOS-NLOS* and *LOS-always*), this chapter enables a considerably higher quality analysis of the effects of linear clustering of vehicles and the extreme blockage effects of the surrounding buildings.

3.2 Blockage and Antenna Models

In the model, the blockage of mmWave V2V communications depends on the relative position of the *typical* transmitter, *typical* receiver and interferers on a grid. *LOS-NLOS* separation takes place at the position of the obstructing vehicle between *typical* transmitter and *typical* receiver. Therefore, it is assumed that the nearest obstructing vehicle is located at a distance of λ^{-1} m from the *typical* receiver because of the homogeneous PPP. In other words, if the density of vehicles is 0.02 and on average two vehicles exist per 100 m, then the average distance between two consecutive vehicles is 50 m, which is equivalent

to λ^{-1}. Similarly, the location of the next consecutive vehicle is λ^{-1} and it also acts as a blockage. To address the blockage relationships, the following path loss model is proposed,

$$\mathcal{P}_L(r,\lambda) = \begin{cases} C_1 \begin{cases} Ar^{-\alpha_L} & \text{if } r \leq \lambda^{-1} \text{ and nodes are on the same road for } r > 1, \\ Ar^{-\alpha_N} & \text{otherwise.} \end{cases} \\ \\ C_2 \begin{cases} Ar^{-\alpha_L} & \text{if nodes are on the same road for } r > 1, \\ Ar^{-\alpha_N} & \text{otherwise.} \end{cases} \end{cases} \tag{3.1}$$

where $\mathcal{P}_L(r,\lambda)$ and r are the path loss function and Manhattan distance between any transmitter/interferer-receiver pair, and A is the path loss intercept modelled as $(4\pi f_c/c)^{-2}$ where f_c and c are the carrier frequency and speed of light, respectively. For case C_1, the path loss is LOS until the position of $r = \lambda^{-1}$. Alternatively, case C_2 defines the path loss for a communications link between either the *typical* transmitter and the *typical* receiver, or the interferer and the *typical* receiver subject to LOS fading if both are positioned on the same grid line. For both cases, if one is positioned on a vertical grid line and the other on a horizontal grid line, the communications link is subject to NLOS fading. If both are located on parallel streets, it is defined that communication is not possible and that interference is negligible.

The vehicles on a single line form a homogeneous PPP, with a Poisson-distributed number of nodes and a uniform distribution of the nodes on the line. The origin is defined as the *typical* receiver location, and related changes of the probability model are prevented by using Slivnyak's theorem and PPP. A clear illustration of the relative positions of *typical* transmitter-receiver and interferers in the proposed blockage model in Fig. 3.1. Note that the impact of the location and blockage of the *typical* transmitter is omitted in this chapter, to enable a tractable baseline for comparison in later chapters where the model is refined to include such effects.

3.3 Coverage Analysis

The definition of the signal-to-interference-plus-noise-ratio (SINR) is presented in (3.2) with transmitter power P_t, small scale fading random variable between *typical* transmitter and receiver h_0, distance between *typical* transmitter and receiver d, and path loss exponents for LOS links α_L, distance r_i, small-scale fading random variable for interferers h_i, path loss exponents for NLOS links α_N, noise power N_0, and main and side lobe gains G_m and g_s, respectively.

In addition, the antenna gain relationships and half-power beamwidths are defined as in (2.5). $\Phi_{\text{LOS+NLOS}}/\{z\}$ defines the group of all LOS and NLOS interferers, excluding the *typical* transmitter at position z. Moreover, it is assumed that the beams of the *typical* transmitter and receiver are defined to be perfectly aligned. The SINR is then given as

$$\text{SINR} = \frac{P_t G_m G_m h_o \mathcal{P}_L(d,\lambda)}{\sum_{i \epsilon \Phi_{\text{LOS+NLOS}}/\{z\}} P_t G_{i->t_r} G_{t_r->i} h_i \mathcal{P}_L(r_i,\lambda) + N_0}, \tag{3.2}$$

where $G_{i->t_r}$ and $G_{t_r->i}$ are the antenna gains between the interferers and the *typical* receiver, as explained in detail in Chapter 2.

The coverage probability is the likelihood that the received SINR is greater than a specified threshold $\mathcal{T}$. For simplicity, all interference related terms are represented by I. The coverage probability is defined as

$$\mathbb{P}_c = \mathbb{P}\left(\frac{P_t G_m G_m h_o \mathcal{P}_L(d,\lambda)}{\sum_{i \epsilon \Phi_{\text{LOS+NLOS}}/\{z\}} P_t G_{i->t_r} G_{t_r->i} h_i \mathcal{P}_L(r_i,\lambda) + N_0} > \mathcal{T}\right), \tag{3.3}$$

which could be rewritten as where $I = \sum_{i \epsilon \Phi_{\text{LOS+NLOS}}/\{z\}} P_t G_{i->t_r} G_{t_r->i} h_i \mathcal{P}_L(r_i,\lambda)$

$$\mathbb{P}_c = \mathbb{P}\left(h_o > \frac{\mathcal{T}}{P_t G_m G_m \mathcal{P}_L(d,\lambda)}(I + N_0)\right), \tag{3.4}$$

which can be translated into

$$\mathbb{P}_c = 1 - \mathbb{P}\left(h_o < \frac{\mathcal{T}}{P_t G_m G_m \mathcal{P}_L(d,\lambda)}(I + N_0)\right). \tag{3.5}$$

In the model, small-scale fading is defined to be Nakagami fading as described in Chapter 2, which implements a gamma-distributed random variable as it is regarded as the most appropriate candidate model for small-scale fading [39]. Alzer's lemma [57], which is introduced in Chapter 2, is used in order to calculate the probability term in (3.5), which states that when $h_0 \sim \Gamma(m, 1/m)$ for an integer m, the probability term is tightly bounded with

$$[1 - e^{-azm}]^m < \mathbb{P}(h_0 < z), \qquad \text{where } a = (m!)^{-1/m}. \tag{3.6}$$

Hence, by applying Alzer's lemma and the expected value operation, the following is obtained,

$$\mathbb{P}_c < \mathbb{E}_\Phi\left(1 - \left(1 - e^{\frac{-a\mathcal{T}m}{P_t G_m G_m \mathcal{P}_L(d,\lambda)}(N_0+I)}\right)^m\right). \tag{3.7}$$

Equation (3.7) can then be written as

$$\mathbb{P}_c \overset{(a)}{<} \sum_{n=1}^{m} \binom{m}{n} (-1)^{n+1} \mathbb{E}_\Phi\left(e^{\frac{-an\mathcal{T}m}{P_t G_m G_m \mathcal{P}_L(d,\lambda)}(N_0+I)}\right), \tag{3.8}$$

where (a) is the binomial expansion of the terms in the expected value. Equation (3.8) can be written as

$$\mathbb{P}_c \overset{(b)}{<} \sum_{n=1}^{m} \binom{m}{n} (-1)^{n+1} \underbrace{\mathbb{E}_{I_H}\left(e^{-snI_H}\right)}_{\text{Own Road and } \mathcal{L}_H} \underbrace{\mathbb{E}_{V_1}\left(e^{-snI_{V_1}}\right)}_{\text{Left Vertical Road and } \mathcal{L}_{V_1}} \underbrace{\mathbb{E}_{V_2}\left(e^{-snI_{V_2}}\right)}_{\text{Right Vertical Road and } \mathcal{L}_{V_2}} \underbrace{\left(e^{-snN_0}\right)}_{\text{Noise Term}}, \tag{3.9}$$

where (b) in (3.9) is extending the terms in the expected value for each path, i.e. the horizontal and vertical roads at both sides of the *typical* receiver. $\mathbb{E}_{I_H}$, $\mathbb{E}_{V_1}$ and $\mathbb{E}_{V_2}$ are the expected value operators for interferences of horizontal, left and right vertical roads, respectively. Note that the same notation is applied for their Laplace transforms. Similarly, I_H, I_{V_1}, I_{V_2} represent the aggregate (sum) interference of the horizontal, left and vertical roads, respectively. For simplicity, the product operator is included for each antenna gain case, and the Laplace transform for horizontal road interferers is represented as

$$\begin{aligned}\mathcal{L}_H = & \underbrace{\mathbb{E}_{I_H}\left(\prod_{\Phi_H} \mathbb{E}_{h_i}\left(e^{-snP_t h_i G_m G_m \mathcal{P}_L(r,\lambda)}\right)\right)}_{\text{Main-to-Main Lobe Alignment Interference}} \\ & \cdot \underbrace{\mathbb{E}_{I_H}\left(\prod_{\Phi_H} \mathbb{E}_{h_i}\left(e^{-snP_t h_i G_m g_s \mathcal{P}_L(r,\lambda)}\right)\right)}_{\text{Main-to-Side Lobe Alignment Interference}} \\ & \cdot \underbrace{\mathbb{E}_{I_H}\left(\prod_{\Phi_H} \mathbb{E}_{h_i}\left(e^{-snP_t h_i g_s g_s \mathcal{P}_L(r,\lambda)}\right)\right)}_{\text{Side-to-Side Lobe Alignment Interference}}.\end{aligned} \tag{3.10}$$

Equation (3.10) distributes the expected values for each antenna gain case and small-scale fading random variables, with $s = \frac{a\mathcal{T}m}{P_t G_m G_m \mathcal{P}_L(d,\lambda)}$. Equation (3.10) can then be written as

$$\mathcal{L}_H \overset{(c)}{=} \underbrace{\mathbb{E}_{I_H}\left(\prod_{\Phi_H}\left(1+snP_tG_mG_m\mathcal{P}_L\left(r,\lambda\right)m^{-1}\right)^{-m}\right)}_{\text{Main-Main Lobe Alignment Interference}}$$
$$\underbrace{\cdot\,\mathbb{E}_{I_H}\left(\prod_{\Phi_H}\left(1+snP_tG_mg_s\mathcal{P}_L\left(r,\lambda\right)m^{-1}\right)^{-m}\right)}_{\text{Main-Side Lobe Alignment Interference}}$$
$$\underbrace{\cdot\,\mathbb{E}_{I_H}\left(\prod_{\Phi_H}\left(1+snP_tg_sg_s\mathcal{P}_L\left(r,\lambda\right)m^{-1}\right)^{-m}\right)}_{\text{Side-to-Side Lobe Alignment Interference}}, \tag{3.11}$$

where (c) is the Moment Generating Function, which is introduced in Chapter 2, of the gamma random variable and Φ_H corresponds to the PPP of the horizontal road. Equation (3.11) can then be written as

$$\mathcal{L}_H \overset{(d)}{=} \underbrace{\prod_{i\,\epsilon\,G_{R_i}} e^{-\mathbb{P}_i\lambda_t\left(\int_R\left(1-\left(1+snP_tG_i\mathcal{P}_L(r,\lambda)m^{-1}\right)^{-m}\right)dr_h\right)}}_{\text{Receiver Side Interference}}$$
$$\underbrace{\cdot\prod_{i\,\epsilon\,G_{O_i}} e^{-0.5\lambda_t\left(\int_R\left(1-\left(1+snP_tG_i\mathcal{P}_L(r,\lambda)m^{-1}\right)^{-m}\right)dr_h\right)}}_{\text{Other Side Interference}} \tag{3.12}$$

where (d) is the Probability Generating Functional of the PPP that is introduced in Chapter 2. $G_{R_i} = \{G_mG_m, G_mg_s\}$ are the antenna gain cases from the interferers that are located at the receiver beam side, see Fig. 3.1, with a probability of $\mathbb{P}_i = \{\mathbb{P}_{G_mG_m}, 1-\mathbb{P}_{G_mG_m}\}$. $G_{O_i} = \{G_mg_s, g_sg_s\}$ are the antenna gain cases from the interferers that are located at the other side of the receiver beam with a probability of 0.5 in each case. Note that the interference of interferers that are located at the receiver beam side are multiplied by the main lobe gain of the *typical* receiver in all cases. Hence, the g_sg_s case does not exist at the receiver beam side. Furthermore, the probability of $\mathbb{P}_{G_mG_m}$ is shaped by (2.6) and characterized by the σ parameter. Since the beamwidth of the side lobe is typically much wider than the beamwidth of the main lobe, it is assumed that the interferences that are located at the other side of the receiver beam will be multiplied by the side lobe gain of the *typical* receiver which eliminates the probability of main-to-main lobe interference from the other side of the receiver beam, see Fig. 3.1. Hence, the probability of interferers at the other side of the receiver beam, which also point their antenna beams towards

the *typical* receiver, and accordingly their complementary probability, is 0.5. Therefore, by integrating (3.12), Laplace transforms of *LOS-NLOS* (case 1) and *LOS-always* (case 2) of a horizontal road are given as

$$\mathcal{L}_{H_{C_1}} \overset{(e)}{=} \prod_{i \epsilon G_{R_i}} e^{\mathbb{P}_i \lambda_t \left(Q\left(r_h;\alpha_L,r_{\min},\lambda^{-1}\right)+Q\left(r_h;\alpha_N,\lambda^{-1},r_{\max}\right)\right)} \cdot \prod_{i \epsilon G_{O_i}} e^{0.5\lambda_t \left(Q\left(r_h;\alpha_L,r_{\min},\lambda^{-1}\right)+Q\left(r_h;\alpha_N,\lambda^{-1},r_{\max}\right)\right)}, \tag{3.13}$$

$$\mathcal{L}_{H_{C_2}} = \prod_{i \epsilon G_{R_i}} e^{\mathbb{P}_i \lambda_t Q(r_h;\alpha_L,r_{\min},r_{\max})} \prod_{i \epsilon G_{O_i}} e^{0.5\lambda_t Q(r_h;\alpha_L,r_{\min},r_{\max})}. \tag{3.14}$$

Operation (e) in (3.13) is the integration of the binomial expansion and following some algebra where $Q(r;\alpha,r_1,r_2)$, can thus be given as

$$Q(r;\alpha,r_1,r_2) = r\left({}_2F_1\left(\frac{-1}{\alpha},m;\frac{\alpha-1}{\alpha};-snm^{-1}P_tG_iAr^{-\alpha}\right)-1\right)\Bigg|_{r_1}^{r_2}, \tag{3.15}$$

where ${}_2F_1$ is the hyper-geometric series and formulated with dummy variables for $|z|<1$ as

$${}_2F_1\left(a,b;c;z\right) = \sum_{n=0}^{\infty} \frac{(a)_n (b)_n}{(c)_n} \frac{z^n}{n!}, \tag{3.16}$$

where $(a)_n, (b)_n, (c)_n$ are the rising Pochhammer symbols, which are given by

$$(a)_n = \begin{cases} 1, & n=1, \\ a(a+1)\cdots(a+n-1), & n>1 \end{cases}. \tag{3.17}$$

Even though ${}_2F_1$ is known as an infinite series, it is observed that after four iterations it quickly converges to a final value. Hence, the Q function can be approximated by

$$\begin{aligned} Q_{\text{Approx.}}(r;\alpha,r_1,r_2) = r\Bigg(1 &+ \frac{-\alpha^{-1}m}{1-\alpha^{-1}} \frac{\left(-snm^{-1}P_tG_iAr^{-\alpha}\right)}{1!} \\ &+ \frac{-\alpha^{-1}(1-\alpha^{-1})m(m+1)}{(1-\alpha^{-1})(2-\alpha^{-1})} \frac{\left(-snm^{-1}P_tG_iAr^{-\alpha}\right)^2}{2!} \\ &+ \frac{-\alpha^{-1}(1-\alpha^{-1})(2-\alpha^{-1})m(m+1)(m+2)}{(1-\alpha^{-1})(2-\alpha^{-1})(3-\alpha^{-1})} \frac{\left(-snm^{-1}P_tG_iAr^{-\alpha}\right)^3}{3!} - 1\Bigg)\Bigg|_{r_1}^{r_2}. \end{aligned} \tag{3.18}$$

It is observed that the most dominant terms in (3.18) are the first two terms. The resulting terms of $r^{-2\alpha}$ and $r^{-3\alpha}$ cause significantly smaller multipliers in the 3-rd and 4-th terms, even for short distances. Hence, it is possible to

process (3.18) by substituting s resulting as

$$Q_{\text{Intuitive}}(r;\alpha,r_1,r_2)=\left(\frac{m(m!)^{-1/m}n\mathcal{T}G_iAr^{1-\alpha}}{(\alpha-1)G_mG_m\mathcal{P}_L(d,\lambda)}\right)\Bigg|_{r_1}^{r_2}. \tag{3.19}$$

Equation (3.19) can be shortened to make it more insightful for the main-to-main lobe interference scenario, with $r_2 > d$ and $m = 1$ in the *LOS-always* case such as

$$Q_{\text{Intuitive}}(r;\alpha,r_1,r_2)=\left(\frac{\mathcal{T}r}{\alpha-1}\left(\frac{d}{r}\right)^{\alpha}\right)\Bigg|_{r_1}^{r_2}. \tag{3.20}$$

Considering that Q is the exponential term in the Laplace transforms, its small fluctuations cause large variations in the resulting probability. Note that, the ratio of $\left(\frac{d}{r}\right)^{\alpha}$ acts as a break point in order to hold the requirement of $r_1 > d$ or $r_2 > d$ in (3.18). Equation (3.20) shows that the Q function is independent of the path loss intercept A. Furthermore, the SINR threshold, $\mathcal{T}$, has a large impact on the system design, and the path loss exponent has a very large impact on Q in addition to being exponentially dependent on distance related parameters.

Similarly, by applying the same steps for vertical roads, $\mathcal{L}_{V_{1_{C_1,C_2}}}$ and $L_{V_{2_{C_1,C_2}}}$ are the Laplace transforms of the vertical roads for both the *LOS-NLOS* and *LOS-always* cases, and are represented as

$$\mathcal{L}_{V_{1_{C_1,C_2}}}=\prod_{i\,\epsilon\,G_{v_{1_i}}} e^{2\lambda_t 0.5Q\left(r_{h_1}+r_{v_1};\alpha_N,r_{\min},r_{\max}\right)}, \tag{3.21}$$

$$L_{V_{2_{C_1,C_2}}}=\prod_{i\,\epsilon\,G_{v_{2_i}}} e^{2\lambda_t 0.5Q\left(r_{h_2}+r_{v_2};\alpha_N,r_{\min},r_{\max}\right)}, \tag{3.22}$$

with r_{h_1} and r_{h_2} being the horizontal random variable distances between the *typical* receiver and the vertical roads at both sides of it, and r_{v_1} and r_{v_2} representing the vertical fixed distances between NLOS interferers and the road on which the *typical* receiver is located, as visualized in Fig. 3.1. $G_{v_{1_i}} = \{G_mG_m, G_mg_s\}$ and $G_{v_{2_i}} = \{G_mg_s, g_sg_s\}$ correspond to the antenna gain combinations from the left and right vertical roads, respectively, with a probability of 0.5. If the beams of the interferer vehicles that are located on vertical roads are pointed towards the horizontal road, then it is assumed that they interfere with their main lobe gain, otherwise with their side lobe gain. Note that the probability of vehicles communicating with a vehicle in front of them or to their rear is assumed to be 0.5. Furthermore, $r_{\min}$ and $r_{\max}$ are the integration limits of the communications distance, and it is assumed that the minimum distance is 1 m and the maximum distance is 250 m as the mmWave signal will be highly attenuated after several hundred meters. The

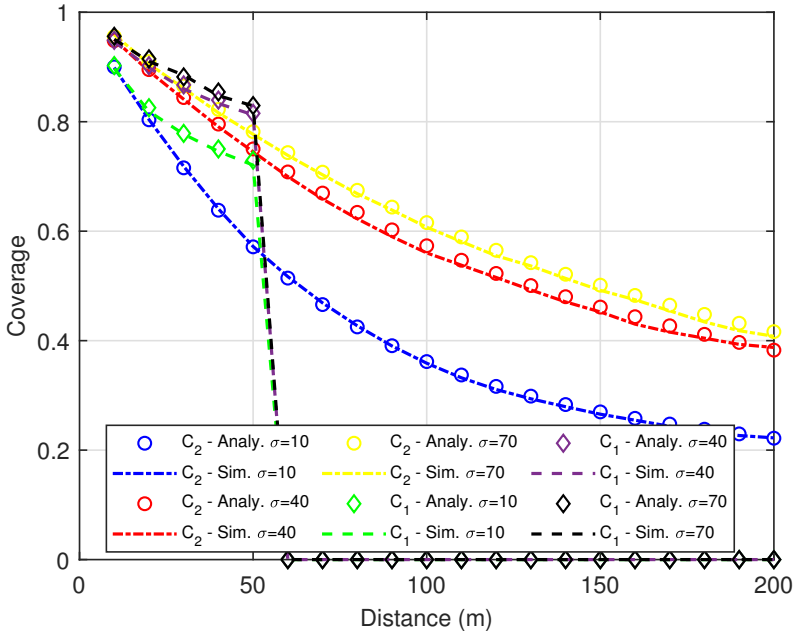

Figure 3.2: Dependence of the coverage probability on the distance for various σ, with markers and lines representing the results from mathematical models and simulations, respectively. Parameters used: $\mathcal{T} = 5\,\text{dB}$, $\lambda_t = 0.01$, $\lambda = 0.02$, $P_t = 1$, $r_{v_1} = 80\,\text{m}$, $r_{v_2} = 20\,\text{m}$, $\phi = \pi/6$, $g_s = 0.1$ [62], $f_c = 60\,\text{GHz}$, $\alpha_L = 2$ and $\alpha_N = 4.5$ [48].

thermal noise and bandwidth are $-174\,\text{dBm/Hz}$ and $500\,\text{MHz}$ for all results. $\mathcal{L}_{H_{C_1}}$ and $\mathcal{L}_{H_{C_2}}$ are Laplace transforms for the horizontal roads for *LOS-NLOS* and *LOS-always*, where the density of active transmitters on horizontal and vertical roads, λ_t, is assumed to be half of λ, as there are equal number of transmitters and receivers.

The final coverage analysis equation for *LOS-NLOS* is obtained after insertion of (3.13), (3.21) and (3.22) into (3.9). Similarly, the final equation for *LOS-always* is obtained after insertion of (3.14), (3.21) and (3.22) into (3.9).

3.4 Simulation Results

A comparison of the obtained analytical equation with Monte Carlo simulations is shown in Fig. 3.2, 3.4, 3.5 displaying a good match between both methods with a mean squared error smaller than 10^{-4}, and providing additional insight in the coverage of mmWave vehicular communication. The simulations are carried out by distributing random nodes on grid-lines and calculating the SINR for each case more than 10^6 times. The limit of the simulation varies between $[-250\,\text{m}\ 250\,\text{m}]$ for all roads.

The results in Fig. 3.2 represent dense traffic with an interferer vehicle at every $100\,\text{m}$, and display the d-dependence of both the analytical models and the Monte Carlo simulations for various σ. The Probability Density Functions

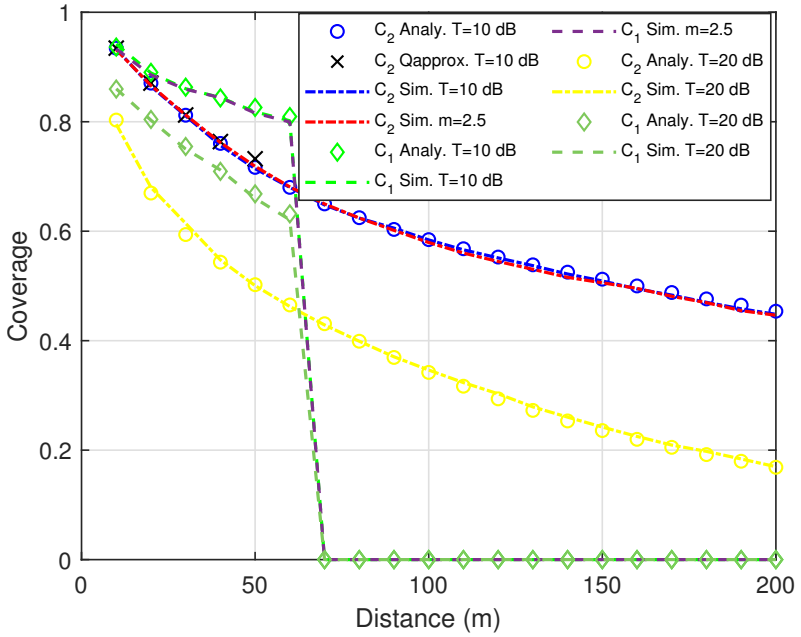

Figure 3.3: Dependence of the coverage probability on the distance for various σ, with markers and lines representing the results from mathematical models and simulations, respectively. Parameters used: $\lambda_t = 0.0075$, $\lambda = 0.015$, $P_t = 1$, $r_{v_1} = 80\,\text{m}$, $r_{v_2} = 20\,\text{m}$, $\phi = \pi/18$, $g_s = 0.1$ [62], $f_c = 60\,\text{GHz}$, $\alpha_L = 2$ and $\alpha_N = 4.5$ [48].

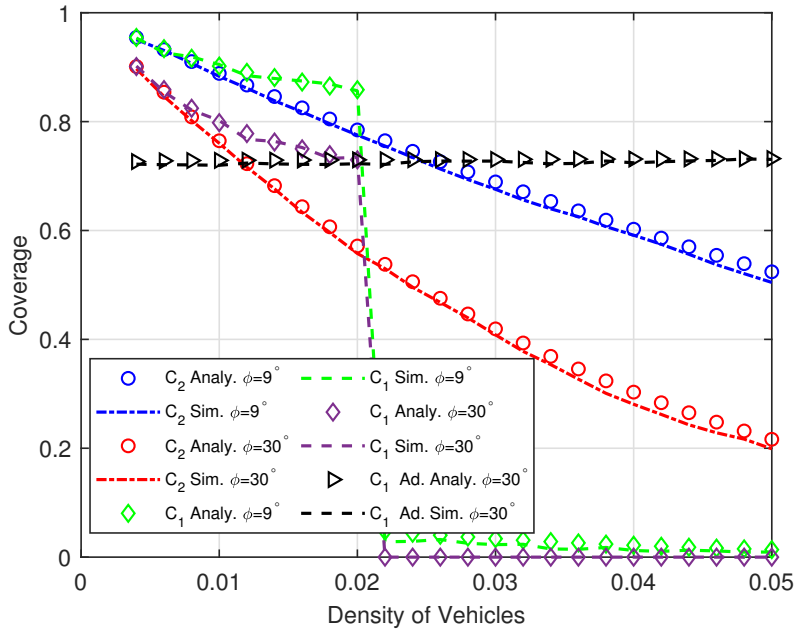

Figure 3.4: Dependence of the coverage probability on the density of vehicles for two beamwidths with markers and lines representing the results from mathematical models and simulations, respectively. Parameters used: $\mathcal{T} = 5\,\text{dB}$, $P_t = 1$, $m = 3$, $d = 50\,\text{m}$, $r_{v_1} = 20\,\text{m}$, $r_{v_2} = 80\,\text{m}$, $g_s = 0.1$ [62], $f_c = 60\,\text{GHz}$, $\sigma = 10$, $\alpha_L = 2$ and $\alpha_N = 4.5$ [48].

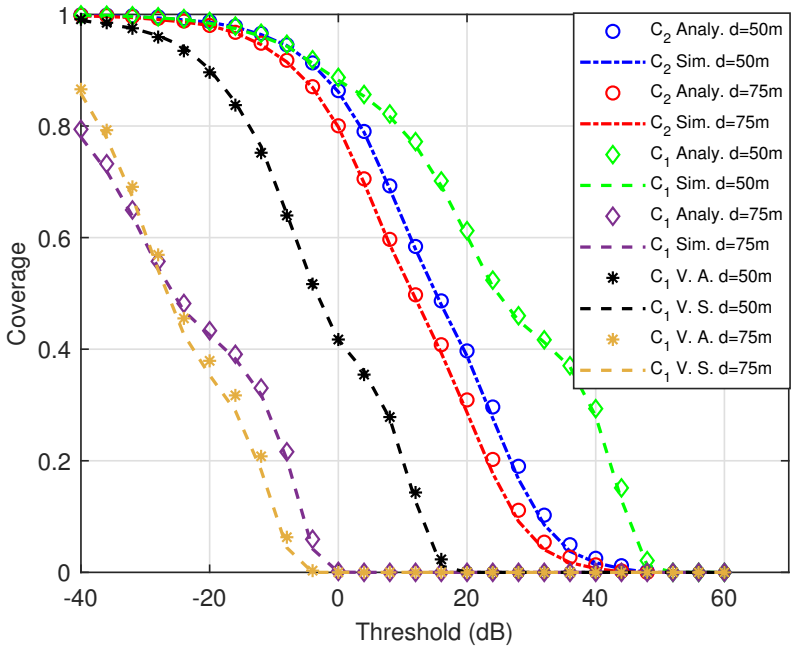

Figure 3.5: Dependence of the coverage probability on the SINR threshold for various distances with markers and lines representing the results from mathematical models and simulations. Parameters used: $\lambda_t = 0.01$, $\lambda = 0.02$, $P_t = 1$, $m = 3$, $r_{v_1} = 20\,\text{m}$, $r_{v_2} = 80\,\text{m}$, $\phi = \pi/18$, $\sigma = 10$, $f_c = 60\,\text{GHz}$ and $g_s = 0.1$ [62]. Path loss exponents for mmWave and VANET are $\alpha_L = 2$, $\alpha_N = 4.5$ [48], $\alpha_L = 2$, $\alpha_N = 3$, respectively.

of the azimuthal angle for three chosen σ values are also displayed in Fig. 2.6 in Chapter 2. The steep decrease of the *LOS-NLOS* results for distances larger than 50 m is due to the transition from LOS to NLOS communications at λ^{-1}, after which the coverage rapidly approaches zero. The *LOS-always* results display a gradually decreasing coverage with distance, with the highest coverage obtained when the largest σ is used for $\mathbb{P}_{G_m G_m}$ in (2.6). In addition, for all cases it is apparent, that interferences from vertical roads only have a limited effect on the coverage, with the largest NLOS interference occurring for small r_{v_1} or r_{v_2}, and the smallest interference occurring when the typical receiver is located at equal distances to both vertical roads. As expected, it is evident that for $d \leq \lambda^{-1}$ the *LOS-NLOS* case outperforms the *LOS-always* case for all d, because of the reduced number of LOS-interferers.

The plots in Fig. 3.3 represents the inter-vehicular distance between the *typical* transceiver pair and coverage for less dense traffic, narrower beam and higher SINR thresholds. As the decrease in density causes larger inter-vehicular distance, the LOS-NLOS transition of C_1 takes place at 66.6 m which is 50 m in Fig.3.2. In addition, the accuracy of $Q_{\text{Approx.}}$ function for the valid convergence interval of hyper-geometric function is illustrated. Finally, it is shown that the system performance is not dependent on being m an integer for C_1 and C_2.

Fig. 3.4 displays the dependence of the coverage probability on the density of interferers for two beamwidths ϕ, with the highest coverage being obtained for smallest ϕ. Increasing the beamwidth results in a reduced gain and a higher interferer beam alignment probability, which both decrease the quality of the communications link. The black markers and line represent the scenario in which the distance between typical transmitter and receiver is parametrized as $d = \lambda^{-1}$; when vehicles between the typical transmitter and receiver are absent. Thus, the increase in density causes a shorter link distance between consecutive vehicles. Hence, in this scenario, a good communications link is always present and slightly density-insensitive, because the positive effect on the quality of the communications link by the exponentially decreasing path loss with decreasing d overcomes the negative effect of increased interference due to increased density, λ.

The results in Fig. 3.5 present the SINR threshold dependence of the coverage probability for various d and for mmWave communications, *LOS-NLOS* and *LOS-always*, and VANET. The latter comparison was made by assigning $m = 1$, lower path loss exponent α_L and α_N [71], 10 MHz bandwidth for noise power calculation, equal lobe alignment probabilities and assigning $G_m = g_s = 1$ due to omnidirectionality. These results show, that in dense vehicular communications networks, due to large α_L and α_N, mmWave communications significantly outperform lower carrier frequency communications protocols, such as VANET, because of the reduced effect of nearby interferers. NLOS mmWave communications only show poorer coverage performance compared to NLOS VANET communications when $d \geq \lambda^{-1}$.

3.5 Conclusions

In this chapter, a tractable coverage model for urban mmWave ad hoc vehicular networks is presented for two different cases. It is shown that line processes can be used to model vehicular networks, which simplifies the analysis. The mathematical model, verified by Monte Carlo simulations, shows that urban mmWave ad hoc vehicular networks could potentially support fully connected traffic, unlike VANET which is more sensitive to an increase in density of transmitters. The analysis shows that by using mmWave, it is possible to fulfill the connectivity needs of a dense traffic scenario, under the condition that communications takes place with vehicles on the same road.

Further, this chapter has shown that mmWave V2V communications are much more sensitive to surrounding LOS interferers, which means that interferers that are located at the adjacent lane of the *typical* receiver will have a significant impact on the coverage performance. Hence, narrowing the focus of research into the effects of interferers surrounding the *typical* receiver, and

eliminating the interferences from vertical roads from the model will provide a significantly simpler model as well as fairly accurate results. In addition, this chapter has shown that how vehicles route and point their antenna beams, and how their manufacturer places mmWave antennas on vehicles, has a significant impact on system performance, due to resulting blockage effects. This will be addressed in the following chapters.

Chapter 4

Connectivity Analysis for mmWave V2V Networks: Exploring Critical Distance and Beam Misalignment

In this chapter, an analytical analysis is presented on the connectivity performance of Vehicle-to-Vehicle communications by using millimeter wave carrier frequencies, by taking into account its challenges of high path loss and beam misalignment. In comparison to Chapter 3, where the link quality of selected transmitter and receiver pairs is analysed, this chapter models the number of connections within a set of vehicles in a single lane. It thus focuses on the probability of reliably sharing the vision of the front vehicle of an autonomous platoon or fleet to the rear vehicle.

The connectivity analysis is carried out in two dimensions; first, an analytical and parametric critical transmission range is developed based on system parameters such as, vehicle density and Signal-to-Interference-Plus-Noise (SINR) ratio threshold, and second, the beam misalignment probability caused by the in-lane lateral displacement of vehicles is determined . The analysis is carried out for antennas with half power beamwidths of 3°, 6°, 10°, 20°, and 45°, resulting in different beamwidth regimes depending upon road curvature and vehicle density. For low/medium vehicle density on low-curvature roads, the sensitivity of the network connectivity to the beamwidth is relatively small. On the other hand, the narrowest beamwidth is the best performer in terms of maximizing connectivity in low/medium vehicle density scenarios on high-curvature roads, and the wider beamwidth is the best performer for high vehicle density on low-curvature roads.

4.1 Introduction

Cooperative driving in the context of connected and autonomous vehicles (CAVs) is a leading automotive research theme within both academia and industry due to its significant and timely potential to enhance and improve safety, traffic flow, fuel consumption and emissions [72]. Fundamentally, cooperative driving is built on the capability to exchange inertia, LIDAR, radar and video, sensor data amongst the vehicles through a wireless channel, with typical implementations as platooning and cooperative adaptive cruise control [73]. Thus a situational, real-time, beyond line of sight awareness is enabled without equipping the vehicles with high-cost, long-range sensors or installing frequent roadside units.

The key metric for the reliability of cooperative driving is *connectivity*, the number of connected/disconnected links between a set of vehicles. In V2V communications, disconnected links can occur frequently due to the high-speed mobility of the nodes, thus rapidly changing the network topology and the dynamic node population [74]. The body of literature has investigated V2V connectivity in the frame of 802.11.p and other sub-6 GHz protocols [3] and builds on distance-shortcomings, i.e. the distance between successive vehicles being longer than the critical transmission range, which is the maximum distance that can enable a reliable link between a transceiver pair

The exchange of giga-byte quantities of data created by LiDAR and cameras is an overwhelming requirement for the aforementioned protocols. Therefore, one of the primary solutions to provide higher data rates, is to use millimeter wave (mmWave) carrier frequencies and directional antenna beams [75]. In addition to distance-based disconnectivity, the use of directional beams will introduce beam misalignment disconnectivity due to the vehicles' mobility

Disconnectivity of sparse vehicular ad hoc networks based on empirical data was studied in [76] and the critical transmission range for connectivity was studied in [77]. In [78], the mean cluster size and probability of forming single clusters for vehicular ad hoc networks was investigated. In [79] the effect of headway distance, acceleration, association time (i.e. connection setup time), relative speed of vehicles, transmission range and message/data size on V2V connectivity was investigated. Moreover, [80] studied multi-hop vehicular connectivity in an urban scenario utilizing GPS traces extracted from San Francisco Yellow cabs. Furthermore, [81] analyzed the relationship between connectivity probability of V2V network, transmission distance and threshold. In [82] analysed the connectivity characteristics and proposed a connectivity-aware MAC protocol for platoon-based VANETs. In addition, [83] investigated the influence of the user behavior and other system parameters on the connectivity probability of V2X networks. Plus, [84] designed a dynamic

cooperation scheme to generate an adaptive multi-hop V2V for maintaining connectivity and throughput when a vehicle located outside of the RSU's coverage region. In [85], a routing decision algorithm to optimize connectivity of V2V networks by taking into account locations of RSU is proposed. Finally, [86] investigated the effect of adverse weather on connectivity probability of V2V networks.

However, mmWave communications has not been considered in these works as the focus was on developing an analytical model for a system based on sub-6 GHz communication systems. Hence, [87] considered mmWave communications and used the obstacle size and route relay window relationships to obtain the best connectivity between hops. In vehicular mmWave communications, [88] studied the performance of dual-hop vehicle-to-vehicle (V2V) communications and the best cooperative vehicular relay selection, however, this work was not specifically designed for vehicular connectivity. Nevertheless, [89] investigated interference impact of intra-cluster vehicles network on mmWave V2V connectivity and proposed dual-slot transmission scheme to maximize connectivity.

Connectivity through mmWave V2V communications has several trade-offs. For example, an increase in vehicle density results in shorter distances for multi-hop communications and thereby improves connectivity, but at the same time it increases the overall interference and deteriorates connectivity performance. In addition, wider beamwidths imply less beam misalignment and thereby improves connectivity, but at the same time it reduces the antenna gain and results in a weaker signal strength, which worsens connectivity. On the other hand, decreasing the beamwidth makes misalignment more likely and thereby worsens the connectivity, but at the same time it increases the antenna gain which causes more powerful signal reception, which results in better connectivity.

To reveal the effective factors on connectivity of mmWave V2V networks, the contributions of this chapter, which has been peer-reviewed by the IEEE community, can be summarized as

- An analytical model is presented and validated by Monte Carlo simulations, which shows the reaction of connectivity performance according to a change of vehicle density, beamwidth, SINR threshold and antenna gain.

- A two-dimensional connectivity probability is introduced that includes a variable critical transmission range based on SINR-threshold and beam misalignment probability caused by the in-lane lateral displacement of vehicles.

- Beamwidth optimization strategies are introduced which show that; (i) the narrowest beam is not the best performer for high-density traffic and low-curvature roads, (ii) connectivity performance has a minor dependence on beamwidth for low and medium vehicle density on low curvature roads, (iii) significant changes in connectivity performance typically occur only for beams narrower than 10°.

4.2 System Model

In this chapter, a unidirectional, and single-lane, vehicular traffic flow is taken into account between two adjacent road side units (RSUs) which are located at the road intersections. The separation distance, D, between two RSUs is illustrated in Fig. 4.1. The primary purpose of this set-up is the enabling of cooperative driving through the passing of LIDAR and other sensor data between each vehicle in the network and the RSUs by implementing multi-hop data transmission. It is assumed that each vehicle is equipped with two mmWave transceiver antennas with corresponding directional-beamforming-providing capabilities. It is assumed that the array antennas that provides directional beams can be modelled as single antenna from system point of view. For convenience, the package of array antennas are mentioned as singular antenna throughout the thesis. One of the antennas is assumed to be the transmitter, and the other a receiver at any moment. It is assumed that each vehicle passes data packages to the closest vehicle at its rear and located in the same lane. Differing from Chapter 3, the direction of data propagation is now one-way, i.e. from front to rear. Furthermore, each vehicle behaves both as a transmitter and a receiver at any moment, as illustrated in Fig. 4.1.

The CI path loss model [90] is used in this chapter, which is introduced in Chapter 2. The path loss exponent is found to be approximately 2 in the most recent measurements [91] when the carrier frequency is set to 60 GHz.

Empirical Vehicular Ad Hoc Networks (VANET) studies have shown that the number of vehicles that passes an observer point follows a Poisson distribution [76, 92]. Given that a road segment is defined by $\mathcal{D} = [0\ D]$ where a vehicle enters the network at position $x = 0$ and leaves at $x = D$. By using order statistics and conditional distributions [93], it is revealed that the positions of each vehicle on the road segment $[0\ D]$ forms as a PPP, in particular for sparse vehicular traffic.

The curvature of road, beamwidth and density of vehicles strongly affects the probability of vehicles interfering with each other. Fig. 4.1 shows the distribution of interferers for the same road curvature and beamwidth, with a lower number of interfered vehicles in Fig. 4.1a compared to Fig. 4.1b, due to fact that the former has a lower vehicle density.

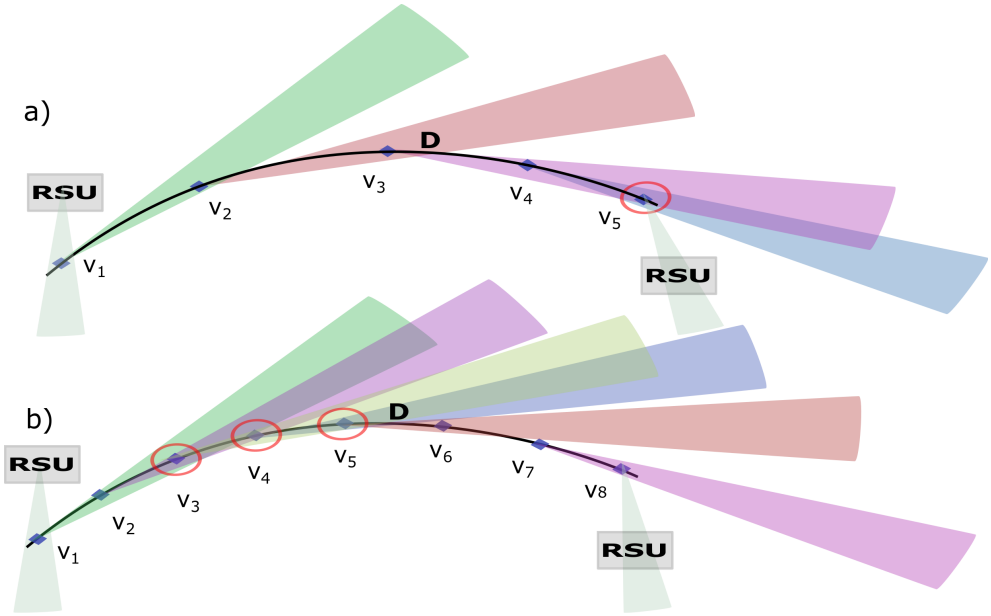

Figure 4.1: Graphical representation of vehicles distributed on a curvy road. The intended receiver for the transmitter vehicle, v_i, is v_{i+1}. In (a), note that v_5, the vehicle in the red circle, is an interfered node as it also stays in the propagation region of beam of v_3. In (b), 3 vehicles are interfered.

Intuitively, vehicles travelling on a straight road will interfere with each other as they will likely stay in the beam propagation region. Also, it is clear that an increased beamwidth will cause higher interference to other vehicles as can be visualized from the comparison of Fig. 4.2 and Fig. 4.1, in which the number of vehicles is the same, but the road curvature is different. Thus, the σ parameter is introduced in order to model the aforementioned issues where σ and the probability of being interfered with, are inversely proportional.

Since the interference of the main lobe and side lobe gains are different, it is necessary to thin the density of transmitter/interferers. $\mathbb{P}_{G_mG_m}$, $\mathbb{P}_{G_mg_s}$, and $\mathbb{P}_{g_sg_s}$ are the probability of main-to-main, main-to-side, and side-to-side lobe gain interferers, respectively. In addition, the aforementioned probabilities are dependent on whether the interfering beams propagate towards the receiver's beam side or its other side. For instance, $\mathbb{P}_{G_mG_m}$ can only be formed by

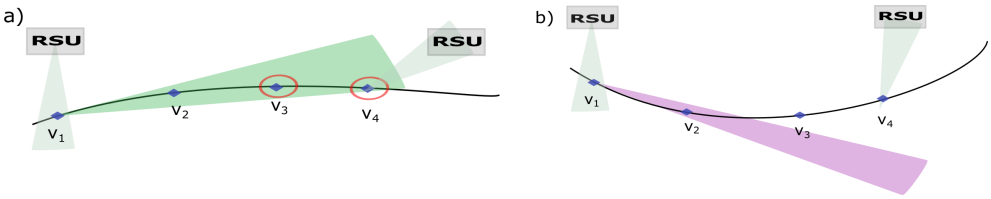

Figure 4.2: Graphical representation of the relationship between interference, beamwidth and road curvature. Note that in (a) the antenna beam of v_1 interferes with v_3 and v_4, whereas in (b) it does not interfere with any vehicles.

the vehicles that are located on the receiver vehicle's beam side as both the interferer and receiver beams have to align. The thinning probability of main-to-side lobe interference from the receiver beam side is modeled as $1 - \mathbb{P}_{G_m G_m}$ whereas the thinning probability of side-to-side lobe interference from the other side is modeled as 0.5. This is due to the assumption of unidirectional data flow, leading to half of the interferers being located at the other side of the receiver's beam and directing their beams towards the other side of the receiver vehicle. Thus, $\mathbb{P}_{G_m G_m}$ is modelled as a two-peak truncated Gaussian random variable as in Chapters 2 and 3, and other gain combinations are given as $\mathbb{P}_{G_m g_s} = 1 - \mathbb{P}_{G_m G_m}$, $\mathbb{P}_{g_s g_s} = 0.5$. The relationship between the main lobe gain and beamwidth is modelled as in (2.4). In Chapter 3, (2.6) is used to model V2X communications, hence employs much larger σ values. In this chapter, (2.6) represents beam alignment probabilities based on the road curvature. Considering that most road curvatures are relatively small due to safety concerns for driving, this chapter uses much smaller σ parameters accordingly.

4.2.1 Distance-based Connectivity

The connectivity analysis in this chapter is built on two fundamental branches, namely distance and beam alignment. To be able to connect two consecutive vehicles over a mmWave channel, the receiver vehicle must be located in the critical transmission range of the transmitter vehicle. For the distance-based connectivity analysis, the critical transmission range of transmitter vehicles, r_c, is modelled based on a pre-set SINR. In other words, if the receiver SINR is greater than some pre-set threshold, $\mathcal{T}$, then the maximum distance between consecutive transmitter and receiver pairs that provides a robust and reliable link for SINR $\geq \mathcal{T}$ is set as the critical transmission range. The expected value of SINR is given as

$$\mathbb{E}\left(\frac{P_t G_m G_m A r_c^{-\alpha}}{I + N_0}\right) \geq \mathcal{T}, \tag{4.1}$$

where P_t, A, α, N_0 are transmitter power, path loss intercept, path loss exponent, and zero-mean Gaussian noise magnitude, respectively. Also, I is the sum of all interferences and defined as $\sum_{i \epsilon \Phi / \{z\}} P_t G_{i->t_r} G_{t_r->i} A r_i^{-\alpha}$ excluding the corresponding transmitter that is located at z. Note that small scale fading is ignored for the purpose of analytical simplification. Also, the blockage effect of obstructing vehicles is omitted due to fact that the transmitter and receiver antennas are placed on the roof of the vehicles. By extracting the transmitter power, antenna gain and path loss from the expected value in (4.1),

the following is obtained,

$$P_t G_m G_m A r_c^{-\alpha} \mathbb{E}\left(\frac{1}{I+N_0}\right) \geq \mathcal{T}. \tag{4.2}$$

After rearranging (4.2) by converting the inequality to equality, the critical transmission range is defined as

$$r_c = \left(\frac{P_t G_m G_m A \mathbb{E}(\frac{1}{I+N_0})}{\mathcal{T}}\right)^{1/\alpha}. \tag{4.3}$$

To calculate the expected value in (4.3), by means of moving the integral into the expected value, it is rewritten as

$$\mathbb{E}\left(\frac{1}{I+N_0}\right) = \mathbb{E}\left(\int_0^\infty e^{-s(I+N_0)} ds\right), \tag{4.4}$$

where the expected value can be moved into the integral as

$$\mathbb{E}\left(\frac{1}{I+N_0}\right) = \int_0^\infty \mathbb{E}\left(e^{-sI}\right) e^{-sN_0} ds. \tag{4.5}$$

Thereafter applying the probability generating functional (PGFL) which is introduced in Chapter 2, results in

$$\begin{aligned}\mathbb{E}\left(\frac{1}{I+N_0}\right) = \int_0^\infty e^{-sN_0} e^{\lambda \mathbb{P}_{G_m G_m} \int_R \left(e^{-sP_t G_m^2 A r^{-\alpha}} - 1\right) dr} \\ \times e^{\lambda \mathbb{P}_{G_m g_s} \int_R \left(e^{-sP_t G_m g_s A r^{-\alpha}} - 1\right) dr + \lambda \mathbb{P}_{g_s g_s} \int_R \left(e^{-sP_t g_s^2 A r^{-\alpha}} - 1\right) dr} ds.\end{aligned} \tag{4.6}$$

Finally, the expected value of the inverse of the interference and noise is rewritten and presented as

$$\mathbb{E}\left(\frac{1}{I+N_0}\right) = \int_0^\infty e^{-sN_0} \prod_{i \in \Phi_G} F_i ds, \tag{4.7}$$

where Φ_G set corresponds to $\{G_m G_m, G_m g_s, g_s g_s\}$ for antenna gains and $\{\mathbb{P}_{G_m G_m}, \mathbb{P}_{G_m g_s}, \mathbb{P}_{g_s g_s}\}$ for their probabilities in

$$F_i = e^{\lambda \mathbb{P}_i \left(r_{\max.} \left(\frac{\mathcal{E}_{1+\frac{1}{\alpha}}\left(\frac{sP_t G_i A}{r_{\max.}^\alpha}\right)}{\alpha} - 1 \right) - r_{\min.} \left(\frac{\mathcal{E}_{1+\frac{1}{\alpha}}\left(\frac{sP_t G_i A}{r_{\min.}^\alpha}\right)}{\alpha} - 1 \right) \right)},$$

where $\mathcal{E}_{1+\frac{1}{\alpha}}$ is the exponential integral and can be expressed as

$$\mathcal{E}_{1+\frac{1}{\alpha}}\left(\frac{sP_t G_i A}{r_{\max.}^\alpha}\right) = \int_1^\infty \frac{e^{-t\frac{sP_t G_i A}{r_{\max.}^\alpha}}}{t^{1+\frac{1}{\alpha}}} dt,$$

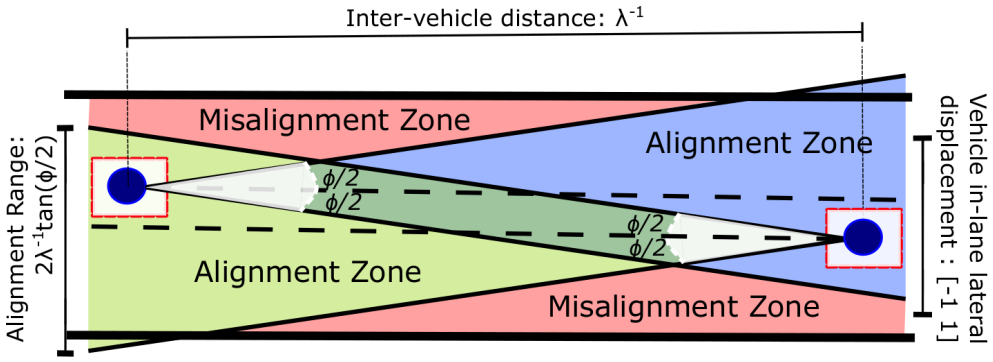

Figure 4.3: Characterization of alignment and misalignment regions of vehicular antenna beams in a single-lane road layout.

and $r_{\text{max.}}$ is chosen as a high number, such as $10D$, in order to take into account the interference of vehicles outside the connectivity region, $\mathcal{D}$, whereas $r_{\text{min.}}$ is chosen as 1 m. Insertion of (4.7) into (4.3) finalizes the critical transmission range. Note that by presenting a solution for the inverse of the sum of interferences in (4.7), this also provides a generic solution for the inverse of sum of random variables which is a variant of Campbell's Theorem that is presented in Chapter 2.

4.2.2 Misalignment-based Connectivity

The beam misalignment of the transceiver pair can only be caused by in-lane instantaneous lateral displacement of the vehicles. It is assumed that the average lane-width is 3.65 m, and the average car width is 1.7 m. Since the transceiver antennas are placed at the centre-top of the vehicles, the lateral displacement range of the antennas is modelled as $\left[-\left(\frac{3.65-1.7}{2}\right) \quad \left(\frac{3.65-1.7}{2}\right)\right]$, which approximately corresponds to $[-1 \quad 1]$. Lateral displacement measurements of [94] have a similar range as shown in Fig. 4.3. In addition, [95] has measured lateral distribution of vehicles on UK highways and formed 23 bins. Therefore, the probability distribution of this lateral displacement is modelled as Gaussian with mean $\mu = 0$ and standard deviation $\gamma = 0.32$. In this set-up, the probability of the centre of the vehicle to be located at the position of -1 or 1 is 0.009. Since the PPP is applied, the average distance between two consecutive vehicles is λ^{-1}. Thus, half of the width of the transmitter beam's alignment zone at the receiver's location is $\lambda^{-1} \tan\left(\frac{\phi}{2}\right)$ due to the fact that the alignment zone of the beam widens with distance, as is shown in Fig. 4.3. Therefore, the probability of the receiver antenna to be located in the alignment

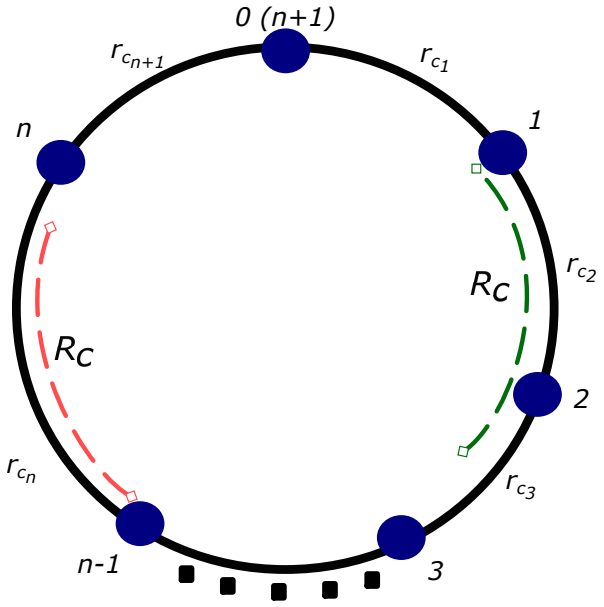

Figure 4.4: Graphical representation of the circular distribution of vehicular distances. The red arc, R_c, shows the case where critical transmission range is shorter than the required distance to satisfy SINR threshold. On the other hand, the green arc, R_c, represents the case in which the required distance is shorter than the critical transmission range.

zone of the transmitter beam is given as

$$\mathbb{P}_A = \int_{-1}^{1} \frac{e^{\frac{-y_t^2}{2\gamma^2}}}{\sqrt{2\pi\gamma^2}} \left(\int_{y_t-\lambda^{-1}\tan\left(\frac{\phi}{2}\right)}^{y_t+\lambda^{-1}\tan\left(\frac{\phi}{2}\right)} \frac{e^{\frac{-y_r^2}{2\gamma^2}}}{\sqrt{2\pi\gamma^2}} dy_r \right) dy_t, \tag{4.8}$$

where y_t and y_r are the locations of transmitter and receiver, respectively and (4.8) can be simplified as

$$\mathbb{P}_A = \frac{1}{2} \int_{-1}^{1} \frac{e^{\frac{-y_t^2}{2\gamma^2}}}{\sqrt{2\pi\gamma^2}} \left(\operatorname{erf}\left(\frac{y_t + \lambda^{-1}\tan\left(\frac{\phi}{2}\right)}{\gamma\sqrt{2}} \right) - \operatorname{erf}\left(\frac{y_t + \lambda^{-1}\tan\left(\frac{\phi}{2}\right)}{\gamma\sqrt{2}} \right) \right) dy_t. \tag{4.9}$$

It is geometrically straightforward to prove that if the receiver is located in the alignment region of the transmitter, then the transmitter is located in the alignment region of the receiver.

4.3 Connectivity Analysis

The probability of entirely covering a unit circle with finite arcs of equal length, where the arcs are uniformly and independently distributed, has been studied thoroughly in the literature [96, 97], also providing the distribution of the gaps, i.e. any point that is not covered by arcs. Interestingly, the resulting

mathematical models can be used as a base for V2V connectivity, in which the clockwise initial points of any arc can be modelled as the locations of the transmitter vehicles, and the length of the arcs can be modelled as the critical transmission ranges. Moreover, the occurrence of any gaps can be modelled as disconnected links. By adding misalignment probabilities to the analytical model in order to make it suitable for mmWave V2V networks, a two dimensional connectivity model is obtained. The arc-based analytical conversion is carried out as follows. First, the distance between two consecutive vehicles at any moment t as shown in Fig. 4.1 is normalized by D and redistributed on a circle as shown in Fig. 4.4. In other words, the locations of vehicles in Fig. 4.1 are mapped onto a unit circle, and hence inter-vehicle distance between consecutive vehicles in Fig. 4.1 are transformed into curve segments in Fig. 4.4. Accordingly, the distance threshold, r_c defined in (4.3) for the given SINR threshold $\mathcal{T}$, is also mathematically transformed. Then, the consecutive inter-vehicle distance is scaled by D for each vehicle, thus $n+1$ links is given as

$$r_{c_i}(t) \triangleq \frac{r_{v_i}(t)}{D},\ i = 1, 2, ..., n+1. \tag{4.10}$$

Similarly, the scaled SINR-based critical transmission range, R_c, is obtained by using r_c/D. The probability of the i-th arc in Fig. 4.4 to be longer than the scaled critical transmission range, which causes disconnectivity regardless of the connection state of other links, is represented as

$$\mathbb{P}_n(i) \triangleq \mathbb{P}\left(r_{c_i}(t) > R_c, i = 1, 2, ..., n+1 | N(t) = n\right). \tag{4.11}$$

Since disconnectivity can occur due to failure to reach the critical transmission range and due to beam misalignment, it is necessary to examine them individually. The probability that the i-th link is solely disconnected by failure to reach critical transmission distance is given as [96]

$$\mathbb{P}_d(i) = (1 - iR_c)^n \ \text{ for } i \leq \lfloor R_c^{-1} \rfloor. \tag{4.12}$$

The probability of misalignment-based disconnectivity between two consecutive vehicles in a network of n vehicles is given as

$$\mathbb{P}_m(i) = (1 - \mathbb{P}_A)^i \, \mathbb{P}_A^{n+1-i}. \tag{4.13}$$

By combining (4.12) and (4.13), the probability of the i-th link to be discon-

nected is given as

$$\mathbb{P}_n(i) = \begin{cases} \sum_{j=0}^{i} \binom{i}{j} (1-\mathbb{P}_A)^j \, \mathbb{P}_A^{i-j} (1-(i-j)R_c)^n, & \text{if} \quad i-j \leq \lfloor R_c^{-1} \rfloor \\ 0, & \text{if} \quad i-j > \lfloor R_c^{-1} \rfloor \end{cases} . \tag{4.14}$$

The probability of exactly i disconnected links in the whole network is modelled [97] as

$$\widehat{\mathbb{P}}_n(i) = \binom{n+1}{i} \sum_{j=0}^{n+1-i} \binom{n+1-i}{j} (-1)^j \, \mathbb{P}_n(i+j) . \tag{4.15}$$

Finally, by changing the upper limit of the sum operators [74], the probability of i disconnected links caused by failure to reach the critical transmission range and/or caused by misalignment is summarized as

$$\widehat{\mathbb{P}}_n(i) = \begin{cases} \binom{n+1}{i} \sum_{j=0}^{\lfloor R_c^{-1} \rfloor - i} \binom{n+1-i}{j} (-1)^j \, \mathbb{P}_n(i+j), & \\ & \text{if} \quad i \leq \lfloor R_c^{-1} \rfloor \\ 0, & \text{if} \quad i > \lfloor R_c^{-1} \rfloor \end{cases} . \tag{4.16}$$

4.4 Analysis and Discussion

In this section, the connectivity performance, validated by Monte Carlo simulations with more than 10^6 iterations, is analytically analysed by means of counting the number of disconnected links in a network by changing parameters such as vehicle density, curvature based interference rate, SINR threshold and beamwidth. In addition, the effect of beamwidth is investigated for 5 different angles, $3°, 6°, 10°, 20°, 45°$ in order to sample from narrow to wide beamwidth. The parameters of the analysis are set as follows: $g_s = 0.1$, $P_t = 1\,\text{W}$, and $N_0 = -86.86\,\text{dBm}$ for 500 MHz. The vehicle density per lane is gradually increased from Fig. 4.5, Fig. 4.6, and Fig. 4.7. Accordingly, the number of links are calculated by using $\lambda D + 1$ which includes both RSU links. as links of two RSU. Zero disconnected links means that the vehicular network is end-to-end connected.

The σ, which is implemented in (2.6) in order to control main-to-main lobe gain interference probability, $\mathbb{P}_{G_m G_m}$, is used accordingly to shape the probability of main-to-side and side-to-side lobe interferences. A lower σ implies that a vehicle's beam is more likely to propagate in the same lane, which results in more interference to vehicles in the lane. On the other hand, a higher σ implies that the vehicle's beam is more likely to propagate out of the lane, which results in less interference for those vehicles. In order to analyze two cases, σ is set as 1 or 5, which simulates low- and high curvature roads, respectively. For instance, in the $\sigma = 1$ case, the main-to-main lobe interference

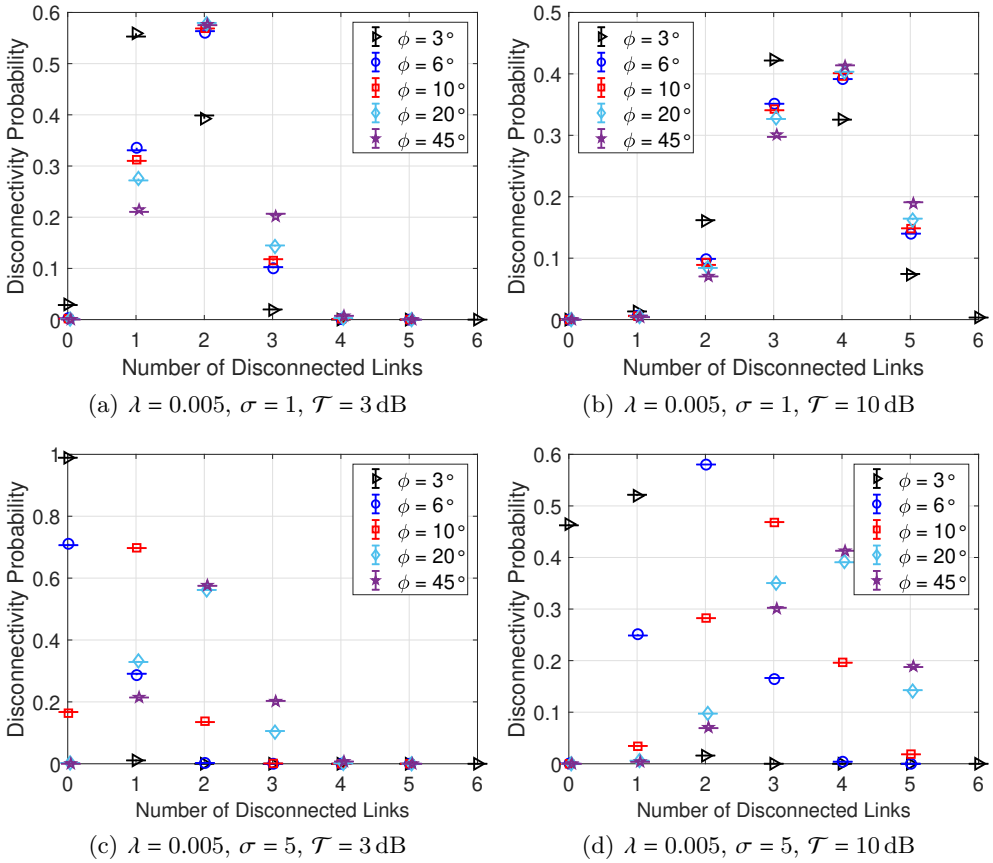

(a) $\lambda = 0.005$, $\sigma = 1$, $\mathcal{T} = 3\,\text{dB}$ (b) $\lambda = 0.005$, $\sigma = 1$, $\mathcal{T} = 10\,\text{dB}$

(c) $\lambda = 0.005$, $\sigma = 5$, $\mathcal{T} = 3\,\text{dB}$ (d) $\lambda = 0.005$, $\sigma = 5$, $\mathcal{T} = 10\,\text{dB}$

Figure 4.5: Low vehicle density case where triangle markers and horizontal lines show the analytical and simulation results, respectively. Average inter-vehicle distance is 200 m where $D = 1000\,\text{m}$.

probabilities of $3°, 6°, 10°, 20°, 45°$ beamwidth scenarios, $\mathbb{P}_{G_m G_m}(\sigma)$, are 0.43, 0.49, 0.5, 0.5, and 0.5, whereas, in the $\sigma = 5$ case they are 0.12, 0.23, 0.34, 0.47, 0.5, respectively. Because of the assumption that beams propagate towards the vehicles only from the front, the maximum probability of main-to-main lobe interference is set as 0.5. Also, since the road curvature and vehicle density have a stronger effect for narrow beamwidths, a higher variance is implemented for $3°$ and $6°$.

Fig. 4.5 illustrates the connectivity performance for 6 links in a scenario in which the average distance between consecutive vehicles is 200 m, which results in a wide alignment zone that covers most of the lateral displacement of the receiver vehicle. It can be noticed that the probability is almost zero to have 0, 4, 5, or 6 disconnected links, whereas there is a finite probability to have 1, 2, or 3 disconnected links. When the SINR threshold is increased to be 10 dB, the probability values change and shift towards a higher number of disconnected links, which is represented in Fig. 4.5b. It can be observed that such a shift occurs for all cases in which the SINR threshold is increased.

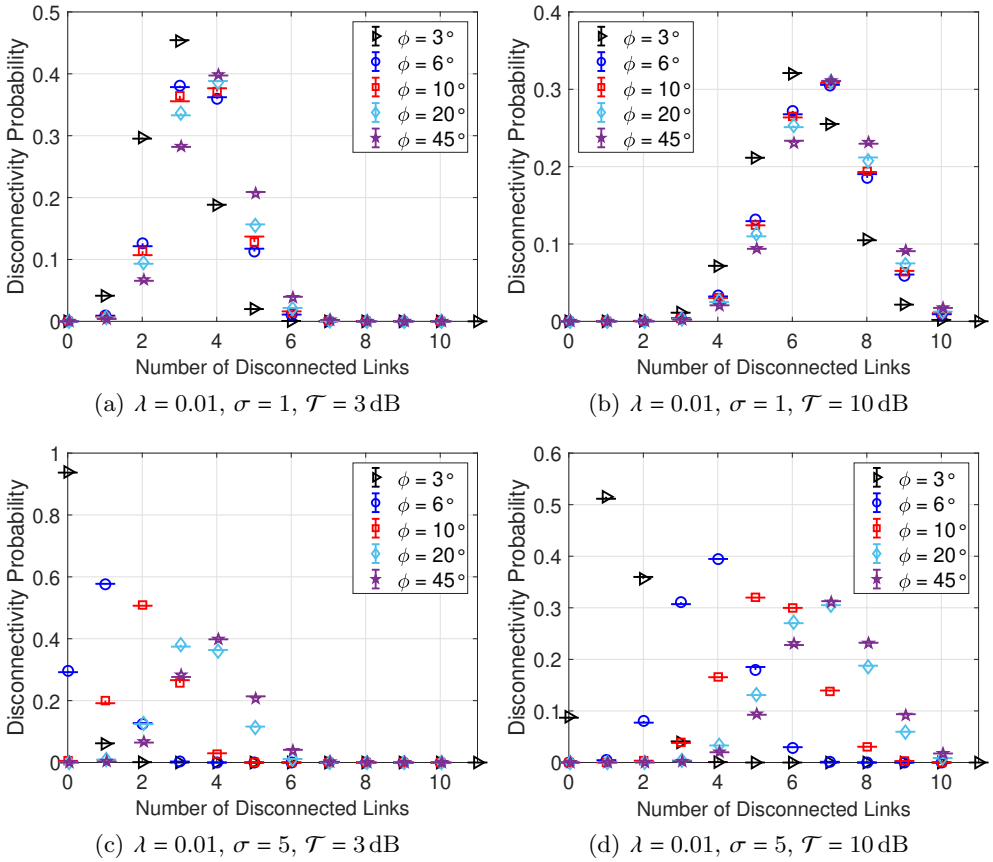

(a) $\lambda = 0.01$, $\sigma = 1$, $\mathcal{T} = 3\,\text{dB}$ (b) $\lambda = 0.01$, $\sigma = 1$, $\mathcal{T} = 10\,\text{dB}$

(c) $\lambda = 0.01$, $\sigma = 5$, $\mathcal{T} = 3\,\text{dB}$ (d) $\lambda = 0.01$, $\sigma = 5$, $\mathcal{T} = 10\,\text{dB}$

Figure 4.6: Medium vehicle density case where triangle markers and horizontal lines show the analytical and simulation results, respectively. Average inter-vehicle distance is 100 m where $D = 1000\,\text{m}$.

Figs. 4.5a and 4.5b illustrate that connectivity performance has a low sensitivity to beamwidth regardless of SINR threshold. However, in Figs. 4.5c and 4.5d, the implementation of higher σ results in less interference, thus narrowing the beams clearly maximizes the connectivity. Interestingly, in Fig. 4.5c, 3° beamwidth almost provides an entirely end-to-end connected network as the probability for zero disconnected links is almost 1. Furthermore, the difference in connectivity performance between different beamwidths becomes more distinct for higher SINR threshold as is shown in Fig. 4.5d. Also note that the deteriorated connectivity performance in Figs. 4.5b and 4.5d in comparison to Figs. 4.5a and 4.5c is mostly caused by the shorter critical transmission range due to the higher SINR threshold; the beam misalignment probability is of minor importance.

In general, increase in the number of vehicles on the road increases the total interference for each vehicle, and subsequently causes a decrease in critical transmission range and an increase in the number of disconnected links. Fig. 4.6 shows the connectivity performance for medium vehicular density and in

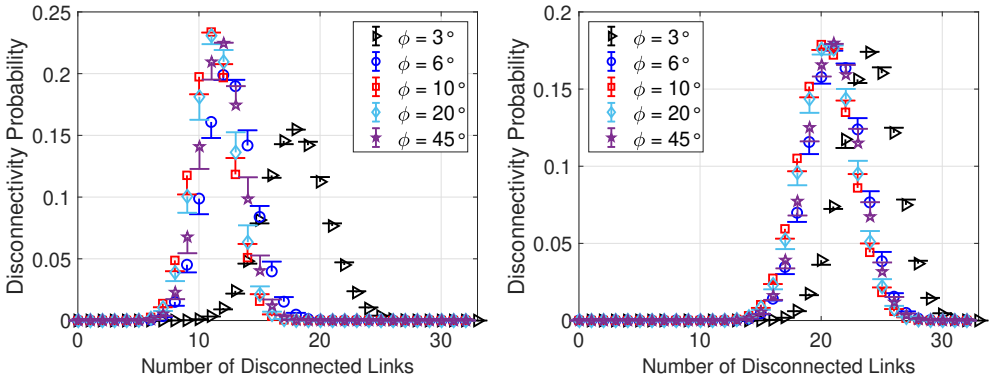

(a) $\lambda = 0.065$, $\sigma = 1$, $\mathcal{T} = 3\,\text{dB}$ (b) $\lambda = 0.065$, $\sigma = 1$, $\mathcal{T} = 10\,\text{dB}$

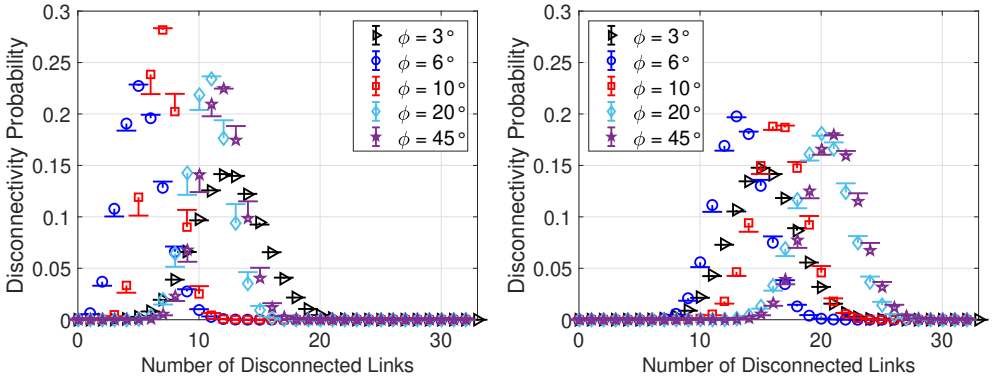

(c) $\lambda = 0.065$, $\sigma = 5$, $\mathcal{T} = 3\,\text{dB}$ (d) $\lambda = 0.065$, $\sigma = 5$, $\mathcal{T} = 10\,\text{dB}$

Figure 4.7: High vehicle density case where triangle markers and horizontal lines show the analytical and simulation results, respectively. Average inter-vehicle distance approximately is 15 m where $D = 500\,\text{m}$.

general, presents similar results as Fig. 4.5. However, note that due to an increased number of vehicles the plots in Fig. 4.6 have maximum disconnectivity probabilities for a higher number of disconnected links in comparison to Fig. 4.5 due to the increase in the number of vehicles. In other words, introducing more hops into the network increases the number of disconnected links and decreases their absolute probabilities. Note that the narrowest beamwidth provides the best connectivity in low/medium vehicle density scenarios regardless σ and $\mathcal{T}$.

In Fig. 4.6c and 4.6d it can be noticed that decreasing the beamwidth increases both the signal power and the interference component in SINR. Interestingly, in low and medium vehicle density cases, the results imply that most of the disconnected links are caused by failure to reach the critical transmission range rather than by misalignment. For instance, in the set-up of Fig. 4.6c, the critical transmission range for beamwidths of 3°, 6°, 10°, 20°, and 45° are approximately 430 m, 230 m, 150 m, 110 m, and 99 m, respectively. Thus, under the conditions of this scenario, only the critical transmission range of a 3° or 6° wide beam is substantially greater than the average inter-vehicle

distance, $\lambda^{-1} = 100\,\text{m}$.

Fig. 4.7 presents results of the high vehicle density case, which could be an implementation of platooning, and provides different inferences compared to Fig.4.5 and Fig. 4.6. For instance, in Fig. 4.7a, 3° provides the worst connectivity, whereas a 20° beamwidth provides the best connectivity, with marginal differences to 10° and 45°, which illustrates the scope for beamwidth optimization. This phenomenon is caused by the closest consecutive vehicle being too close to enable transmitter beam expansion, hence not all in-lane lateral displacements of the receiver vehicles can be compensated for. Similarly, in Fig. 4.7b, the 6°, 10°, 20°, and 45° beamwidth scenarios display an almost identical connectivity performance, in contrast to the worst performance of the 3° beamwidth.

The 6° beamwidth is the best performer in Fig. 4.7c. In this scenario, the critical transmission ranges for 3°, 6°, 10°, 20°, and 45° are approximately 66 m, 36 m, 24 m, 17 m, and 16 m, respectively, and the average consecutive vehicle distance is 15 m. Nevertheless, the misalignment probabilities are 45° are 0.37, 0.075, 0.0043, 0.0018, and 0.0018, respectively. This phenomenon implies that with increasing beamwidth the cause of the disconnected links changes from misalignment to failure in reaching the critical transmission range. Hence, even though 3° provides a substantially greater critical transmission range, its tendency to misalignment hence makes a 6° beamwidth a better choice. Also, note that in some cases there is a trade-off between the number of disconnected links and their probabilities. For instance, in Fig. 4.7d the 6° beamwidth provides less disconnected links with a higher probability, whereas the 3° beamwidth provides more disconnected links with a lower probability. As a comparison, [89] has also investigated the four-lane connectivity of mmWave V2V networks with graphical approach. Their finding is that neutralizing intra-cluster interference significantly improves the performance which is also compatible with finding of this thesis.

4.5 Conclusions

In this chapter, an analytical connectivity analysis of mmWave V2V networks was presented. The resulting analytical model was based on a parametric critical transmission range and a beam misalignment probability caused by the lateral displacement of vehicles, and was validated by Monte Carlo simulations. In addition to stochastic geometry, geometric probability tools were used, that had been developed to calculate the probability of covering all gaps of a circle by uniformly and independently distributed arcs. In order to maximize connectivity, it has been shown that there are different beamwidth regimes depending upon road curvature and vehicle density. In general terms, on low curvature

roads and for low/medium vehicle densities, the connectivity performance is nearly independent of the beamwidth. Moreover, for high vehicle density and low-curvature roads, wide beamwidths outperform narrow beamwidths. For other scenarios the best performance is obtained with narrowest beams. Plus, the system performance varies slightly when beamwidths larger than 10° are employed. Furthermore, increase in vehicle density causes more number of disconnected links, yet with less probability of occurrence. Finally, the trade-off between critical transmission range and misalignment probability has been characterized such that, increase in beamwidth results less misalignment based disconnectivity, yet more failure to reach critical range disconnectivity.

Chapter 5

Routing-Based Mean-Interference Analysis of mmWave V2V Networks

As it is discussed in Chapters 2 and 3, the performance of mmWave V2V communications significantly depends on routing behaviour and the probability of being interfered by surrounding vehicles. Further, the models presented in the previous Chapters 3 and 4 are limited to single-lane traffic. In this chapter, in order to provide a higher degree of fidelity and bring the model closer to reality, the number of lanes in the model is gradually increased. In addition to coverage and connectivity, the mean-interference affecting the *typical* receiver is analysed to present an alternative perspective.

In this chapter, an angle-dependent, mean-interference model for two-lane traffic is presented, based on a shifted and hardcore distance-separated Poisson point process, that compares two baseline routing schemes, namely in-lane and closest vehicle routing. It is revealed that closest vehicle routing outperforms the in-lane routing scheme in every scenario, with smallest differences for low vehicle density and wide antenna beamwidths. Although this Chapter assumes that all the interferences are attenuated by LOS path loss, the in-lane routing scheme can be substantially improved if in-lane interferences are attenuated by NLOS path loss due to the metallic body of vehicles.

It is also found that the probability of the closest vehicle being located in the adjacent lane, approximately follows $\frac{e^{-\lambda h_c}}{2}$ where λ and h_c are the density of vehicles and the hardcore distance between vehicles designated by platooning rules, i.e. minimum headway distance. In addition, it is found that the impact of main-to-side and side-to-side antenna lobe gains on the mean-interference is minor compared to the main-to-main antenna lobe gain. Hence neglecting the former cases provides a significant simplification to the model, without losing much accuracy.

5.1 Introduction

Vision-sharing through wireless communications amongst vehicles is a continuous process rather than event-triggered, such as a red traffic light. Given that mmWave communications are dependent on constant beam searching, steering and alignment, and thus sensitive to blockages [45], mmWave links tend to be fragile. Moreover, the unpredictable movement of vehicles and accordingly, the dynamically changing network topology is another beam alignment challenge to overcome.

Beam optimization and performance analysis of mmWave communications in the vehicular domain has recently received a lot of interest from the academic community. For instance, [98] proposes a dynamic beam management framework for V2I communications utilizing traffic signals and road topology. Furthermore, [99] presents a stochastic geometry framework that models the performance of mmWave V2I communications for a mixture of traffic consisting of platoon-autonomous and manned vehicles, in which only platoon-autonomous vehicles use mmWave. Additionally, [100] proposes a 3D-beam alignment-based routing scheme for mmWave V2X communications. Furthermore, [101] presents a latency and reliability analysis for various relaying schemes of mmWave V2V communications, and [102] proposes a low-latency scheme that focuses on an information-centric methodology, in which frequently used packages are cached at the edge of the network. In addition, [103] presents a mathematical analysis for a proactive V2V- or V2I-mode selection, in order to overcome dynamic blockages in vehicular traffic.

Yet, the aforementioned routing schemes tend to be too complicated to sustain in high mobility traffic, considering the requirements of constant beam alignment. In addition, difficulties due to the speed difference between vehicles, overtaking, and lane changing, require adjustments of the network topology beyond the capabilities of current methods. Furthermore, high path loss caused by blockages of mmWave communications will be a problem if the vehicles need to communicate through a blocking vehicle.

So far, there are two baseline routing [104] schemes that easily provide LOS links which are considerably simple to sustain in the dynamic network topologies for mmWave vehicular connectivity. The first scheme is In-Lane Routing (ILR) which sends information packages to nearest vehicles in the own lane, and the second scheme is Closest-Vehicle Routing (CVR) which establishes links with the nearest vehicle regardless of the lane [104]. In terms of stability and lifetime of links, both routing schemes have inherent advantages and disadvantages. For instance, the network topology in the ILR scheme occasionally changes, which solely happens if a vehicle changes its lane, whereas changes in the network topology of the CVR scheme take place more frequently.

In addition, typically the traffic flow in the (UK's) right lane flows faster than in the left lane. Hence, a link between a vehicle in the faster lane that is paired with a vehicle in front of it in a slower lane will be broken after the slower vehicle has been overtaken, and the faster vehicle has become the new front vehicle. Thus, compared to CVR, the ILR scheme provides better stability and better link lifetime performance. However, as can be observed from Fig. 5.1, the CVR scheme causes less interference compared to the ILR scheme, as a considerable part of the interferer's antenna beams are directed away from the road's direction, after a point at which the closest vehicle is located in the adjacent lane. On the contrary, the interferer's beams in the ILR schemes always remain directed along the road which results in a stronger interference for other vehicles. Thus, ILR provides a more stable network topology and longer link lifetime, whereas CVR provides a better signal quality. The purpose of this chapter is to investigate the behaviour of the mean-interference in both schemes, and to discover the regime in which one scheme outperforms the other for various vehicular densities and antenna beamwidths. The contributions of this chapter are,

- It is observed that CVR outperforms ILR in all cases, but the difference in performance decreases with increasing beamwidth. Additionally, the mean-interference of ILR is much more sensitive to increased vehicular density. Also, the impact of main-to-side and side-to-side lobe alignments is minor, so neglecting these alignment cases significantly simplifies the analytical model.

- The strongest interfering vehicles are located in the own lane if the ILR scheme is applied. The ILR scheme can be improved significantly with the application of advanced interference management techniques, with the allocation of orthogonal resource blocks to in-lane interferers, and with the conversion of LOS interferers to NLOS interferers through antenna placement on a vehicles such that signals are attenuated by their metallic bodies. This sustainability potentially makes ILR preferable over the CVR scheme.

- Unlike the main body of the existing literature in which the probability of main-to-main, main-to-side, and side-to-side lobe alignments are hypothetically and roughly modelled, in this work an angle-dependent beam alignment probability model is given for mmWave V2V networks. Even though the model is presented for two-lane roads only to enhance the readability of this chapter, it will be explained how the model can be extended to more lanes.

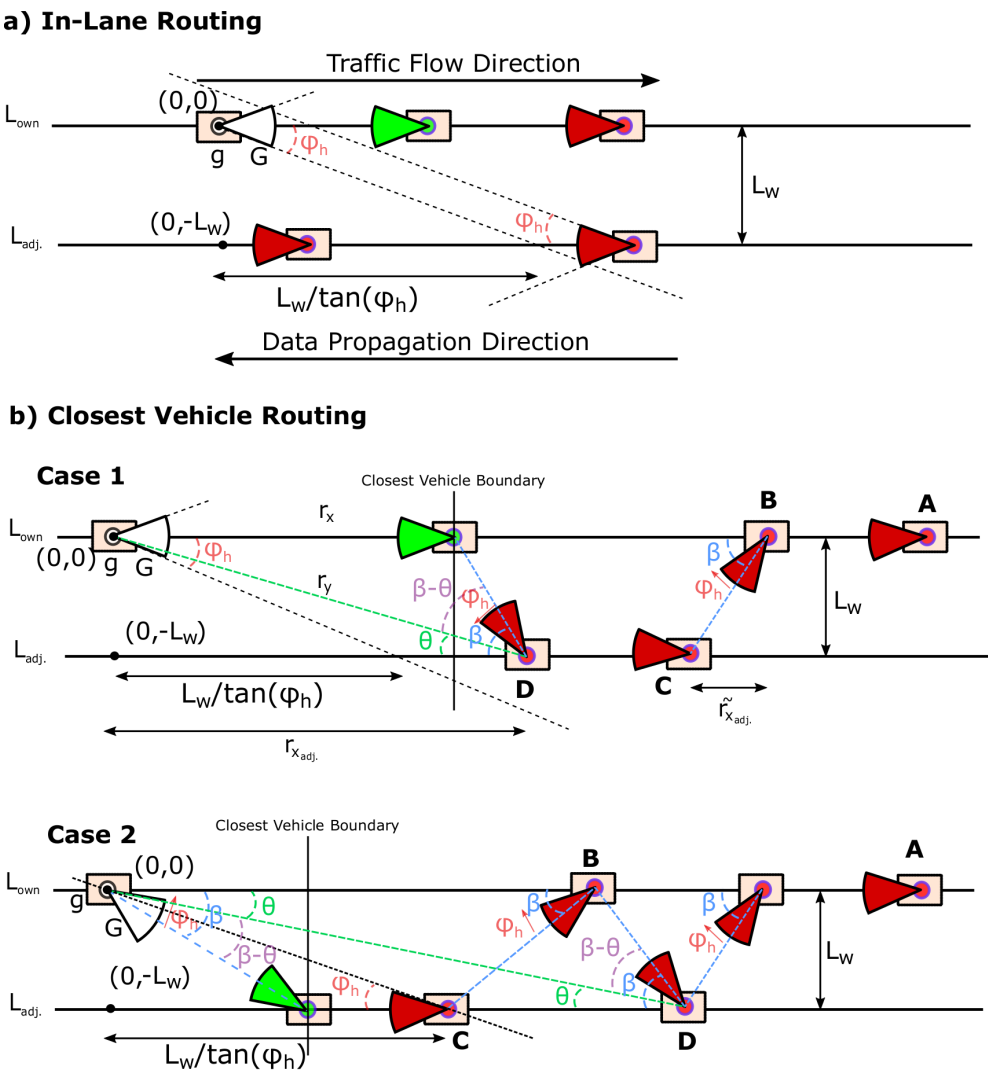

Figure 5.1: Graphical representation of a) the ILR and b) the CVR routing scheme, and the angle-dependence of the interferences in them. Case 1 and 2 in b) classify the scenarios in which the transmitter (green) to the typical receiver (white) is either in the own lane or the adjacent lane, respectively. Vehicle types A and B represent own lane interferer vehicles (red) that are paired with receivers in the own lane or adjacent lane, respectively. Similarly, vehicle types C and D represent adjacent-lane interferer vehicles that are paired with receivers in the adjacent lane or the own lane (w.r.t. to the typical receiver), respectively.

5.2 System Model

It is assumed that each vehicle is equipped with two antennas, one at the front and one at the back. The front and back antennas act as a receiver and a transmitter, respectively, in order to provide a continuous vision-sharing data stream between vehicles. In both routing schemes, it is assumed that the direction of data propagation is always from front to back following the traffic flow, as the vision of the front vehicle is most important to the following vehicles. It is also defined that the *typical* receiver is located in the lane named 'own lane', L_{own}, which is placed at the origin $\{0, 0\}$, as shown in Fig. 5.1. The corresponding *typical* transmitter can be located in either of the lanes, depending upon its location and employed routing scheme.

The main lobe gain, G_m, of any transmitter is given as

$$G_{i->j} = \begin{cases} G_m = \frac{2\pi-(2\pi-\phi)g_s}{\phi} \\ g_s \end{cases}, \tag{5.1}$$

where g_s and ϕ are side lobe gain and half-power beamwidths respectively, and where $0 < g_s \leq 1$. Note that (5.1) is a version of (2.5) without restrictions by $\theta_{i->j}(\sigma)$. The mean-interference notation is $\mathbb{E}\left(I_{\text{own}} + I_{\text{adj.}}\right)$, in which I_{own} and $I_{\text{adj.}}$ are the sum of interferences caused by vehicles that are located in their own and adjacent lanes, respectively.

The sums of own and adjacent lane interferences are given as

$$I_{\text{own}} = \sum_{i \epsilon \Phi_{\text{own}}} P_t h_i G_{i->t_r} G_{t_r->i} A x_i^{-\alpha_L}, \tag{5.2}$$

$$I_{\text{adj.}} = \sum_{i \epsilon \Phi_{\text{adj.}}} P_t h_i G_{i->t_r} G_{t_r->i} A y_i^{-\alpha_L}, \tag{5.3}$$

where Φ_{own}, $\Phi_{\text{adj.}}$, P_t, h_i, A, α_L, x_i, and y_i are the set of interferers at each lane, transmitter power, small-scale fading, path loss intercept, LOS path loss exponent, distance to the *typical* receiver from its own lane, and adjacent lane interferers, respectively, and $G_{t_r->i}$ and $G_{i->t_r}$ are the reciprocal antenna gains of the typical receiver and interferer. Since it is assumed that I_{own} and $I_{\text{adj.}}$ are independent, $\mathbb{E}\left(I_{\text{own}} + I_{\text{adj.}}\right)$ can be written as $\mathbb{E}\left(I_{\text{own}}\right) + \mathbb{E}\left(I_{\text{adj.}}\right)$.

The small scale fading is modelled as Nakagami Chapter 2 and follows $h_i \sim \Gamma(m, 1/m)$. Moreover, since h_i is an independent random variable, the expected value can be written as

$$\mathbb{E}\left(I_{\text{own}}\right) = \mathbb{E}\left(\sum_{i \epsilon \Phi} P_t \mathbb{E}\left(h_i\right) G_{i->t_r} G_{t_r->i} A x_i^{-\alpha_L}\right) \tag{5.4}$$

and $\mathbb{E}(h_i) = m\frac{1}{m} = 1$ because of the gamma distribution. Thus, the sums of the own and adjacent lane interferences are simplified as

$$I_{\text{own}} = P_t A \sum_{i \epsilon \Phi_{\text{own}}} G_{i->t_r} G_{t_r->i} x_i^{-\alpha_L}, \tag{5.5}$$

$$I_{\text{adj.}} = P_t A \sum_{i \epsilon \Phi_{\text{adj.}}} G_{i->t_r} G_{t_r->i} y_i^{-\alpha_L}. \tag{5.6}$$

In the original homogeneous PPP, the points can fall onto each other or be located very close to each other. However, due to the physical dimensions of vehicles and the headway distance, a homogeneous PPP does not reflect the distribution of vehicles very accurately. Therefore, in this chapter the distribution of vehicles is modelled with a variant of PPP, which shifts the positions of vehicles if they are within a set hardcore distance from the *typical* receiver. Commonly, a traffic flow follows a *2-second rule*, which is defined as being the headway distance that a vehicle will travel within 2 seconds at its current speed. Hence, the average headway distance is defined as $2v$, where v is the speed of vehicles in m/s. Then, the density of the distribution, λ, is modelled as $\frac{1}{2v}$. Hence, in the following simulations, the speed components at the x-axis are transformation from density of vehicles. For instance, the case for the of speed 90 km/h, i.e. 25 m/s, corresponds a simulation of PPP for a density of 0.02, in practice. Accordingly, the analytical and simulation results do not include speed-related phenomenons such as Doppler spread.

Nevertheless, it is assumed that the distance of the closest vehicle to the *typical* receiver has to be larger than a set hardcore distance, h_c, depending upon the headway distance between consecutive vehicles. Accordingly, h_c is calculated as $h_t v$ where h_t is minimum headway time between consecutive vehicles. As future traffic flows of autonomous vehicles will include platooning, a 0.5 second headway time is allocated for safe truck platooning [105]. For example, given that the speed of the traffic flow is 90 km/h, i.e. 25 m/s, the average headway distance, density, and h_c are 50 m, 0.02 and 12.5 m for 0.5 second minimum headway time, respectively. Note that this approach offers a conversion between speed and density, which is applied throughout this chapter. Thus, in the following numerical simulations, if the distance between two consecutive vehicles is shorter than h_c, then this distance is increased to h_c by shifting the positions of the vehicles, whereas in the analytical model, only the closest vehicle is shifted by h_c. In this chapter's discussion, it is shown that the distribution of future autonomous traffic can be modelled with a simple shifted homogeneous PPP without the use of more complex repulsive point processes, such as Matérn hard-Core point process [106].

5.2.1 In-Lane Routing Based Mean-Interference

As is depicted in Fig. 5.1a, for ILR the corresponding transmitter of the *typical* receiver will always be located in the receiver's own lane. So, the receiver beam of the *typical* receiver will be aligned in a direction along its own lane. This also implies that any interference must also originate from its own lane, and thus the interferences will be multiplied by the main lobe of the *typical* receiver. Similarly, the beams of their own lane interferers will be multiplied by the interferer's main lobe gain due to the ILR scheme.

Note that since the *typical* transmitter is located within the receiver's own lane, this has an impact on the distribution of the vehicles in that lane. Given that the distribution of the *typical* transmitter's position located in the own lane is $\lambda e^{-\lambda(r_x - h_c)}$, where r_x is the distance between the *typical* receiver and transmitter, then the own lane interference has to be calculated for each r_x. Note that the distance of the closest point to the center follows exponential distribution when homogeneous PPP is employed. As shifted homogeneous PPP is employed, resulting distribution corresponds to $\lambda e^{-\lambda(r_x - h_c)}$. Similarly, the mean interference of the vehicles located in the own road, $\mathbb{E}\left(\sum_{\Phi_{\text{own}}} x_i^{-\alpha_L}\right)$, is calculated as $\int_{r_x}^{\infty} \lambda x^{-\alpha_L} dx$ by using Campbell's theorem [106]. Accordingly, the mean-interference of I_{own} can be expressed as

$$\mathbb{E}\left(I_{\text{own}}|r_x\right) = P_t A G_m G_m \int_{h_c}^{\infty} \lambda e^{-\lambda(r_x - h_c)} \int_{r_x}^{\infty} \lambda x^{-\alpha_L} dx dr_x. \tag{5.7}$$

Assuming that the LOS path loss exponent for mmWave communications is $\alpha_L = 2$ [45], (5.7) can be modified as

$$\mathbb{E}\left(I_{\text{own}}|r_x\right) = P_t A G_m G_m \lambda^2 e^{\lambda h_c} \Gamma\left(0, \lambda h_c\right), \tag{5.8}$$

where Γ is the incomplete gamma function [107]. From (5.8) it can be observed that $\mathbb{E}\left(I_{\text{own}}|r_x\right)$ scales with λ^2. Since λ is inherently smaller than 1 for vehicular networks due to the dimensions of the vehicles and the headway distance, λ^2 causes a smaller coefficient than λ which decreases the interference. On the contrary, $e^{\lambda h_c}$ is a coefficient that represents the shift of the vehicle distribution, and displays that an increase in vehicle density increases the interference exponentially. Also, note that (5.8) is not specifically dependent on beamwidth, excluding the impact of beamwidth on antenna gains as in (5.1).

The mean-interference of vehicles that are located in the adjacent lanes has to be separated depending upon the locations of the interferers. Referring to Fig. 5.1a, if any interferer is located in the expansion region of the beam with an angle of ϕ_h, which is half of the beamwidth ϕ, then its interference is multiplied with the main lobe gain. Note that this relationship is reciprocal from the interferer's point of view and the location corresponding *typical*

transmitter has no impact on the distribution of adjacent lane vehicles.. Then the resulting antenna gain is $G_m G_m$ if the location of the interferer is beyond $\frac{L_w}{\tan(\phi_h)}$, otherwise it is $g_s g_s$. By utilizing Campbell's theorem [106] as in (5.7), the resulting mean-interference of vehicles located in the adjacent lane is

$$\mathbb{E}\left(I_{\text{adj.}}\right) = \int_0^{\frac{L_w}{\tan(\phi_h)}} \frac{P_t A g_s g_s \lambda}{\left(x^2 + L_w^2\right)^{\frac{\alpha_L}{2}}} dx + \int_{\frac{L_w}{\tan(\phi_h)}}^{\infty} \frac{P_t A G_m G_m \lambda}{\left(x^2 + L_w^2\right)^{\frac{\alpha_L}{2}}} dx, \tag{5.9}$$

where L_w is the lane width. For $\alpha_L = 2$, (5.9) becomes

$$\mathbb{E}\left(I_{\text{adj.}}\right) = \frac{P_t A g_s g_s \lambda \tan^{-1}\left(\frac{x}{L_w}\right)}{L_w}\Bigg|_0^{\frac{L_w}{\tan(\phi_h)}} + \frac{P_t A G_m G_m \lambda \tan^{-1}\left(\frac{x}{L_w}\right)}{L_w}\Bigg|_{\frac{L_w}{\tan(\phi_h)}}^{\infty}. \tag{5.10}$$

By inserting the limits of the integral, and given that

$$\tan^{-1}\left(\frac{1}{\tan\left(\phi_h\right)}\right) = \frac{\pi}{2} - \phi_h \text{ for } \phi_h \leq \frac{\pi}{2}, \tag{5.11}$$

(5.10) can be written as

$$\mathbb{E}\left(I_{\text{adj.}}\right) = \frac{\lambda P_t A}{L_w}\left(\overbrace{g_s g_s(\frac{\pi}{2} - \phi_h)}^{\text{Minor Impact}} + G_m G_m \phi_h\right). \tag{5.12}$$

It is shown in (5.12) that $\mathbb{E}\left(I_{\text{adj.}}\right)$ is a simple closed-form equation. Furthermore, $\mathbb{E}\left(I_{\text{adj.}}\right)$ is inversely proportional to the lane width, and it scales with λ instead of λ^2. Interestingly, the $\frac{\pi}{2} - \phi_h$ term in (5.12) is decreasing with increasing beamwidth, accordingly reducing the impact of the side-to-side lobe interference and increasing the effect of main-to-main lobe interference. Yet, it is observed in (5.1) that the change in main lobe gain is more dominant, thus the increase in beamwidth will eventually reduce the total interference. Note that this method can be applied for any number of lanes, by applying nL_w instead of L_w for the n-th lane. Eventually, the total mean-interference of the ILR scheme can be expressed as

$$\mathbb{E}_{\text{ILR}}\left(I|r_x\right) \approx P_t A G_m G_m \lambda \left(\lambda e^{\lambda h_c} \Gamma\left(0, \lambda h_c\right) + \frac{\phi_h}{L_w}\right). \tag{5.13}$$

5.2.2 Closest-Vehicle Routing Based Mean-Interference

The mean-interference of the CVR scheme is heavily dependent on the location of the *typical* transmitter in terms of its lane and its distance to the receiver. The probability distribution function of the distance of the closest vehicle to

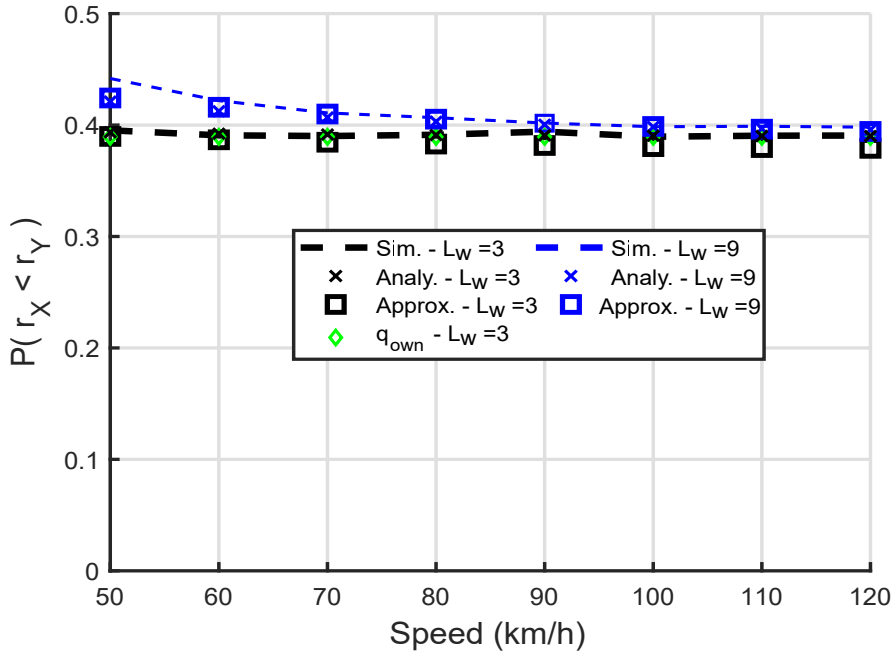

Figure 5.2: Probability of the closest vehicle being located in the own lane versus the speed of the traffic.

the *typical* receiver in its own lane is

$$f_{r_X}(r_x) = \lambda e^{-\lambda(r_x - h_c)}, \tag{5.14}$$

where r_X and r_x represent the random variable and its sample. Note that the probability distribution of the closest vehicle in the adjacent lane, from the typical receiver's point of view, can be modelled with a homogeneous PPP, as the typical receiver has no impact on the distribution of vehicles in the adjacent lane in terms of headway distance. Hence, the probability distribution of the vehicles closest to the location $\{0, -L_w\}$ is given as

$$f_{r_{X_{\text{adj.}}}}\left(r_{x_{\text{adj.}}}\right) = \lambda e^{-\lambda r_{x_{\text{adj.}}}}, \tag{5.15}$$

and the random variable that represents the distance of the vehicle closest to the *typical* receiver is given as $r_Y = \sqrt{r_{x_{\text{adj.}}}^2 + L_w^2}$. The cumulative distribution function of r_Y under the assumption of $r_y \geq L_w$, can then be written as

$$\mathbb{P}\left(r_y > r_Y\right) = \mathbb{P}\left(\sqrt{r_y^2 - L_w^2} > r_{x_{\text{adj.}}}\right). \tag{5.16}$$

Thus, the CDF of r_Y becomes

$$\mathbb{P}\left(\sqrt{r_y^2 - L_w^2} > r_{x_{\text{adj.}}}\right) = \int_0^{\sqrt{r_y^2 - L_w^2}} \lambda e^{-\lambda r_{x_{\text{adj.}}}} dr_{x_{\text{adj.}}}, \tag{5.17}$$

which results in

$$F_{r_Y}\left(r_y\right) = 1 - e^{-\lambda\sqrt{r_y^2 - L_w^2}} \longleftrightarrow f_{r_Y}\left(r_y\right) = \frac{\lambda r_y e^{-\lambda\sqrt{r_y^2 - L_w^2}}}{\sqrt{r_y^2 - L_w^2}}, \tag{5.18}$$

where $F_{r_Y}\left(r_y\right)$ and $f_{r_Y}\left(r_y\right)$ are the CDF and PDF of r_Y respectively. Thereafter, the probability of the closest vehicle being located within the *typical* receiver's own lane is calculated as

$$\mathbb{P}\left(r_Y > r_X\right) = \int_{L_w}^{\infty} f_{r_Y}\left(r_y\right) \int_{h_c}^{r_y} f_{r_X}\left(r_x\right) dr_x dr_y. \tag{5.19}$$

Changing the variable $r_y = \sqrt{r_x^2 + L_w^2}$, (5.19) can be written as

$$\mathbb{P}\left(r_Y > r_X\right) = \int_{h_c}^{\infty} \lambda e^{-\lambda r_x} \left(1 - e^{-\lambda\sqrt{{r_x}^2 + L_w^2}} e^{\lambda h_c}\right) dr_x, \tag{5.20}$$

which includes an analytically unsolvable integral due to the square root term. However, $\sqrt{{r_x}^2 + L_w^2}$ can be approximated as $a_g r_x + a_s L_w$ with a very high accuracy if $r_x \geq L_w$ [108], which requirement holds since the threshold distance, h_c, is typically larger than L_w. For example, the minimum headway distance for a 50 km/h traffic flow is approximately 6 m[109], and the typical lane width is 3 m. Even in the extreme case that the corresponding transmitter is located in the 4-th lane, which means that the total lane separation between the pair is three lane widths and equal to 9 m, and thus larger than h_c, then the approximation error for the distance between the *typical* receiver and the vehicle closest to it, is only 1 m. Therefore (5.20) can be approximated as

$$\mathbb{P}\left(r_Y > r_X\right) \approx e^{-\lambda h_c} - \frac{e^{-\lambda a_g h_c - \lambda a_s L_w}}{a_g + 1}, \tag{5.21}$$

where $a_g = 0.9343$ and $a_s = 0.4269$ are approximation constants that were obtained through multiple regression in [108]. Moreover, (5.21) can be enhanced with a corresponding transmitter that is located in the n-th lane by means of replacing L_w with $(n-1)L_w$. In (5.21) it is observed that for a two-lane network, $\mathbb{P}\left(r_Y > r_X\right)$ can be approximated further as

$$q_{\text{own}} = \frac{e^{-\lambda h_c}}{2}. \tag{5.22}$$

Thus, the probability of the closest vehicle being located within the *typical* receiver's own lane follows (5.22). Hence, the probability of the closest vehicle being located in its own lane exponentially decreases with an increase in vehicle density. Fig. 5.2 shows $\mathbb{P}\left(r_Y > r_X\right)$ for different lane widths and speeds. Moreover, the probability of the closest vehicle being located in the adjacent

lane of the *typical* receiver is $\overline{q_{\text{own}}} = 1 - q_{\text{own}}$, where the over-line notation represents the complementary probability.

As is depicted in Fig. 5.1b, the antenna gain combinations $G_m G_m$, $G_m g_s$ and $g_s g_s$ are dependent upon the angles between the transmitter-receiver pairs and their antenna beamwidths. In Fig. 5.1b, β represents the angle between a pair of one transmitter and one receiver if the pair is located in an adjacent lane to the *typical* receiver. For instance in Case 1, if half of the beamwidth, ϕ_h, is wider than β of the B-C pair, then the beam of vehicle B will interfere with the *typical* receiver with its main lobe antenna gain. Furthermore, θ in Fig. 5.1b represents the angle between adjacent lane interferers and the *typical* receiver. Similarly for Case 1, if ϕ_h is larger than the angle difference $\beta - \theta$ for vehicle D, then the beam of vehicle D will interfere with the *typical* receiver with main lobe gain. Thus, a stochastic characterization of the distributions of the angles is required. The CDFs of β and $\beta - \theta$ describe the probabilities of the antenna gain combinations. The CDF of β can be written as $\mathbb{P}(\phi_h > \beta)$, which becomes

$$\mathbb{P}\left(\phi_h > \sin^{-1}\left(\frac{L_w}{\sqrt{\tilde{r_{x_{\text{adj.}}}}^2 + L_w^2}}\right)\right) = \mathbb{P}\left(\tilde{r_{x_{\text{adj.}}}} > L_w \cot(\phi_h)\right), \tag{5.23}$$

where $\tilde{r_{x_{\text{adj.}}}}$ is the in-lane, inter-vehicle distance. Since it is an exponentially distributed random variable, (5.23) becomes

$$F_\beta = e^{-\lambda L_w \cot(\phi_h)} \longleftrightarrow f_\beta = \frac{\lambda L_w}{\sin^2(\beta)} e^{-\lambda L_w \cot(\beta)}, \tag{5.24}$$

where F_β and f_β are the CDF and PDF of β, respectively. It can be seen that (5.24) shows the probability of being interfered with by the main lobe from any own lane vehicles that establish inter-lane links with adjacent lane vehicles, such as vehicle B in Fig. 5.1b. Furthermore, note that this probability is closed-form, increasing with beamwidth and exponentially decreasing with vehicle density.

In addition to β, the CDF of θ can be written as $\mathbb{P}(\phi_h > \theta)$ which becomes

$$\mathbb{P}\left(\phi_h > \sin^{-1}\left(\frac{L_w}{\sqrt{r_{x_{\text{adj.}}}^2 + L_w^2}}\right)\right) = \mathbb{P}\left(r_{x_{\text{adj.}}} > L_w \cot(\phi_h)\right), \tag{5.25}$$

where $r_{x_{\text{adj.}}}$ is the distance of any adjacent lane vehicle to $\{0, -L_w\}$. As $r_{x_{\text{adj.}}}$ is uniformly distributed because of the homogeneous PPP, (5.25) becomes

$$F_\theta = 1 - \frac{L_w \cot(\phi_h)}{R} \longleftrightarrow f_\theta = \frac{L_w}{R \sin^2(\theta)}, \tag{5.26}$$

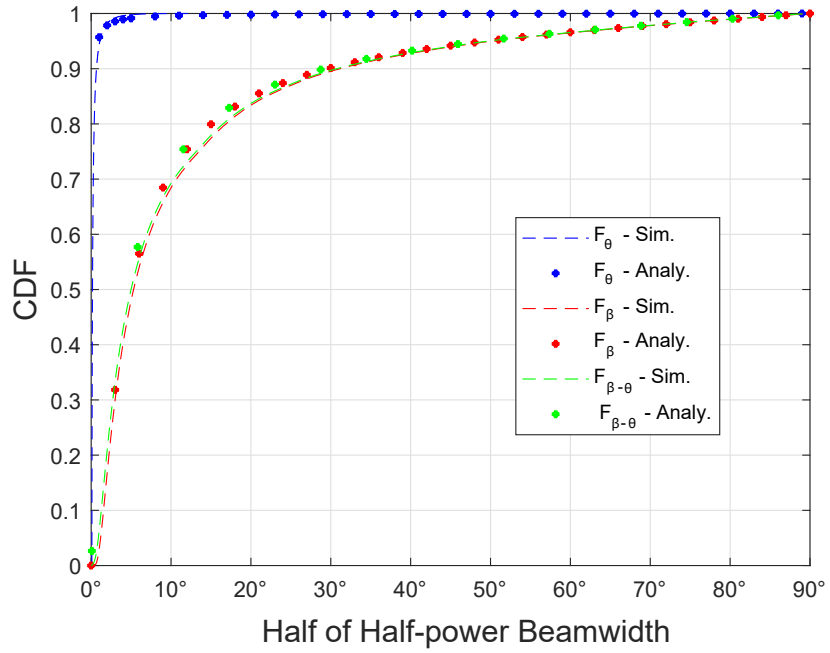

Figure 5.3: CDFs of the angle between adjacent lane interferers and the *typical* receiver, θ; the angle between a pair of one transmitter and receiver if they are located in an adjacent lane to the *typical* receiver, β; and their difference $\beta - \theta$ versus the beamwidth, where $L_w = 3\,\text{m}$ and $v = 90\,\text{km/h}$.

where R is an arbitrary large number to limit the uniform distribution and simulation. The CDF of $\beta - \theta$, $F_{\beta-\theta}$, can be expressed as $\mathbb{P}(\phi_h > \beta - \theta)$ which can be written in terms of f_β and f_θ as

$$F_{\beta-\theta} = \int_{\sin^{-1}\left(\frac{L_w}{R}\right)}^{\pi/2} \frac{L_w}{R\sin^2(\theta)} \int_0^{\phi_h+\theta} \frac{\lambda L_w e^{-\lambda L_w \cot(\beta)}}{\sin^2(\beta)} d\beta d\theta, \tag{5.27}$$

which becomes

$$F_{\beta-\theta} = \int_{\sin^{-1}\left(\frac{L_w}{R}\right)}^{\pi/2} \frac{L_w}{R\sin^2(\theta)} e^{-\lambda L_w \cot(\phi_h+\theta)} d\theta, \tag{5.28}$$

Plots of F_β, F_θ, $F_{\beta-\theta}$ are shown in Fig. 5.3, from which it can be observed that θ is always smaller than ϕ_h, excluding very narrow beams. Furthermore, as F_β and $F_{\beta-\theta}$ perform very similarly, F_β can be used instead of $F_{\beta-\theta}$ in a two-lane road layout, as it is closed-form.

The calculation of the mean-interference of the CVR scheme is carried out in the form of $\mathbb{E}\left(I_{\text{own, adj.}}|r_k\right)_i^{V_j}$ where $k\epsilon\{x, y\}$, $i\epsilon\{1, 2\}$, $j\epsilon\{A, B, C, D\}$. r_k represents the distance between a *typical* transmitter and receiver pair under the condition that the closest vehicle, i.e. the *typical* transmitter, is in the *typical* receiver's own lane ($k = x$, $i = 1$) or the adjacent lane ($k = y$, $i = 2$).

i depicts the case number of the CVR scheme, and j represents the type of vehicle based on its location and routing as shown in Fig. 5.1b. Then, the final mean-interference of the CVR scheme, $\mathbb{E}\left(I_{\text{own}} + I_{\text{adj.}}\right)$, becomes

$$\mathbb{E}\left(I_{\text{own}} + I_{\text{adj.}}\right) = \mathbb{E}\left(I_{\text{own}}|r_x\right)_1^{V_A} + \mathbb{E}\left(I_{\text{own}}|r_x\right)_1^{V_B} + \mathbb{E}\left(I_{\text{adj.}}|r_x\right)_1^{V_C} + \mathbb{E}\left(I_{\text{adj.}}|r_x\right)_1^{V_D}$$

$$+\mathbb{E}\left(I_{\text{own}}|r_y\right)_2^{V_A} + \mathbb{E}\left(I_{\text{own}}|r_y\right)_2^{V_B} + \mathbb{E}\left(I_{\text{adj.}}|r_y\right)_2^{V_C} + \mathbb{E}\left(I_{\text{adj.}}|r_y\right)_2^{V_D} \tag{5.29}$$

.

Case 1

The mean-interference calculation causes by own lane vehicles for Case 1 of the CVR scheme is similar to the ILR scheme. $\mathbb{E}\left(I_{\text{own}}|r_x\right)_1^{V_A}$ can be developed as in (5.8),

$$\mathbb{E}\left(I_{\text{own}}|r_x\right)_1^{V_A} = P_t A q_{\text{own}} q_{\text{own}} G_m G_m \lambda^2 e^{\lambda h_c} \Gamma\left(0, \lambda h_c\right), \tag{5.30}$$

where the first q_{own} term represents the probability that the typical transmitter is located in the own lane, i.e. Case 1. The second q_{own} term models A-type vehicles, i.e. interferers that are located in the own lane.

For Case 1, a B-type vehicle interferes with its main lobe antenna gain with a probability of F_β, and with its side lobe gain with a probability of $\overline{F_\beta}$, thus the mean-interference for such vehicles is

$$\mathbb{E}\left(I_{\text{own}}|r_x\right)_1^{V_B} = P_t A q_{\text{own}} \overline{q_{\text{own}}} \lambda^2 e^{\lambda h_c} \Gamma\left(0, \lambda h_c\right) \left(F_\beta G_m G_m + \overbrace{\overline{F_\beta} G_m g_s}^{\text{Minor Impact}}\right). \tag{5.31}$$

A C-type vehicle in the adjacent lane interferes with the typical receiver with its main lobe gain if its beam covers the location of the *typical* receiver as in the ILR scheme. Note that if this condition is satisfied, then automatically the received interference will be multiplied by the main lobe gain of the *typical* receiver. Hence, the $G_m G_m$ state will hold if the location of a C-type interferer is beyond $\frac{L_w}{\tan(\phi_h)}$ as shown in (5.32). Then (5.33) depicts $\mathbb{E}\left(I_{\text{adj.}}|r_x\right)_1^{V_C}$ for $\alpha_L = 2$.

$\mathbb{E}\left(I_{\text{adj.}}|r_x\right)_1^{V_D}$ is calculated similar to $\mathbb{E}\left(I_{\text{adj.}}|r_x\right)_1^{V_C}$. However, the probability of D-type vehicles interfering with the *typical* vehicle with their main lobe gain is characterized by $F_{\beta-\theta}$, and the main lobe gain multiplication at the *typical* receiver's side depends on the area covered by its antenna beam. If ϕ_h is larger than $\beta - \theta$ at the interferer side, then the resulting antenna gain at the interferer side is G_m, and otherwise it is g_s. Similarly, if its location is beyond $\frac{L_w}{\tan(\phi_h)}$, the resulting gain at the *typical* receiver's side is G_m, and otherwise it

$$\mathbb{E}\left(I_{\text{adj.}}|r_x\right)_1^{V_C} = P_t A q_{\text{own}} q_{\text{own}} \left(\int_{h_c}^{\infty} \lambda e^{-\lambda(r_x - h_c)} \int_{r_x}^{\frac{L_w}{\tan(\phi_h)}} \frac{g_s g_s \lambda}{\left(x^2 + L_w^2\right)^{\frac{\alpha_L}{2}}} dx dr_x + \int_{\frac{L_w}{\tan(\phi_h)}}^{\infty} \frac{G_m G_m \lambda}{\left(x^2 + L_w^2\right)^{\frac{\alpha_L}{2}}} dx \right) \tag{5.32}$$

$$\mathbb{E}\left(I_{\text{adj.}}|r_x\right)_1^{V_C} = \frac{P_t A q_{\text{own}} q_{\text{own}} \lambda}{L_w} \left(G_m G_m \phi_h + \overbrace{g_s g_s (\frac{\pi}{2} - \phi_h) - \int_{h_c}^{\infty} \lambda e^{-\lambda(r_x - h_c)} g_s g_s \tan^{-1}\left(\frac{r_x}{L_w}\right) dr_x}^{\text{Minor Impact}} \right) \tag{5.33}$$

$$\mathbb{E}\left(I_{\text{adj.}}|r_x\right)_1^{V_D} = \frac{P_t A q_{\text{own}} \overline{q_{\text{own}}} \lambda}{L_w} \left(F_{\beta-\theta} G_m G_m \phi_h + \overbrace{\overline{F_{\beta-\theta}} G_m g_s \phi_h}^{\text{Minor Impact}} + \overbrace{F_{\beta-\theta} G_m g_s \left(\frac{\pi}{2} - \phi_h - \int_{h_c}^{\infty} \lambda e^{-\lambda(r_x - h_c)} \tan^{-1}\left(\frac{r_x}{L_w}\right) dr_x\right)}^{\text{Minor Impact}} + \overbrace{\overline{F_{\beta-\theta}} g_s g_s \left(\frac{\pi}{2} - \phi_h - \int_{h_c}^{\infty} \lambda e^{-\lambda(r_x - h_c)} \tan^{-1}\left(\frac{r_x}{L_w}\right) dr_x\right)}^{\text{Minor Impact}} \right) \tag{5.34}$$

---

is g_s. Thus, four different outcomes exist in terms of antenna gains, $G_m G_m$, $G_m g_s$, $g_s G_m$ and $g_s g_s$, as shown in (5.34) when $\alpha_L = 2$.

Case 2

Since the antenna gain and the distance of the own lane interferers to the *typical* receiver are independent random variables in Case 2, the distance component of the mean-interference in the expected value can be extracted and evaluated separately. First,the distance component of the mean-interference is calculated as

$$\mathbb{E}\left(\sum_{i \epsilon \Phi_{\text{own}}} x_i^{-\alpha_L} | r_y \right)_2 = \int f_{r_Y}\left(r_y\right) \int f_{r_X}\left(r_x\right) dr_x dr_y. \tag{5.35}$$

With the change of variable $r_y = \sqrt{r_x^2 + L_w^2}$, the mean-interference can written as

$$\mathbb{E}\left(\sum_{i \epsilon \Phi_{\text{own}}} x_i^{-\alpha_L} | r_{\text{y}}\right)_2 = \int_0^\infty \lambda e^{-\lambda r_x} \int_{\max\left(\sqrt{h_c^2+L_w^2}, r_x\right)}^\infty \lambda x^{-\alpha_L} dx dr_x. \tag{5.36}$$

As the closest vehicle in the *typical* receiver's own lane cannot be closer than r_x, because it is already conditioned that the closest vehicle is in the adjacent lane, the limit of the internal integral has to start from either $\sqrt{h_c^2 + L_w^2}$ or r_x whichever is larger. After algebraic operation, (5.36) becomes for $\alpha_L = 2$

$$\mathbb{E}\left(\sum_{i \epsilon \Phi_{\text{own}}} x_i^{-2} | r_{\text{y}}\right)_2 = \lambda^2 \left(\frac{1 - e^{-\lambda\sqrt{h_c^2+L_w^2}}}{\lambda\sqrt{h_c^2 + L_w^2}} + \Gamma\left(0, \lambda\sqrt{L_w^2 + h_c^2}\right)\right). \tag{5.37}$$

Interference of A-type vehicles that are located in the own lane, conditioning that the closest transmitter is located in the adjacent lane, can be expressed as

$$\mathbb{E}\left(I_{\text{own}} | r_{\text{y}}\right)_2^{V_A} = P_t A \overline{q_{\text{own}}} q_{\text{own}} \left(G_m G_m F_\beta + g_s G_m \overline{F_\beta}\right) \mathbb{E}\left(\sum_{i \epsilon \Phi_{\text{own}}} x_i^{-2} | r_y\right)_2. \tag{5.38}$$

Similarly, the interference of B-type vehicles that are located in the own lane, can be expressed as

$$\mathbb{E}\left(I_{\text{own}} | r_y\right)_2^{V_B} = P_t A \overline{q_{\text{own}}}^2 \left(G_m^2 F_\beta^2 + 2 g_s G_m F_\beta \overline{F_\beta} + g_s^2 \overline{F_\beta}^2\right) \mathbb{E}\left(\sum_{i \epsilon \Phi_{\text{own}}} x_i^{-\alpha_L} | r_{\text{y}}\right)_2. \tag{5.39}$$

The calculation of the mean-interference of C-type vehicles for Case 2, $\mathbb{E}\left(I_{\text{adj.}} | r_{\text{y}}\right)_2^{V_C}$, needs to be handled differently depending on whether the vehicle closest to the *typical* receiver is located beyond $\frac{L_w}{\tan(\phi_h)}$ or not. If the closest transmitter is located before $\frac{L_w}{\tan(\phi_h)}$, then the C-type interferers between the closest vehicle and $\frac{L_w}{\tan(\phi_h)}$ will impact the *typical* receiver with g_s. Additionally, if the closest vehicle is located beyond $\frac{L_w}{\tan(\phi_h)}$, then all the interferers beyond the location of the closest vehicle will impact the *typical* receiver with G_m. Similarly, $F_{\beta-\theta}$ controls the probability of the *typical* receiver multiplying its interference with

G_m or g_s. The following shows the general equation for $\mathbb{E}\left(I_{\text{adj.}}|r_y\right)_2^{V_C}$,

$$\mathbb{E}\left(I_{\text{adj.}}|r_y\right)_2^{V_C} = P_t A\overline{q_{\text{own}}}q_{\text{own}}\Bigg(\left(F_{\beta-\theta}g_s G_m + \overline{F_{\beta-\theta}}g_s g_s\right) \cdot \int_0^{\frac{L_w}{\tan(\phi_h)}} \lambda e^{-\lambda r_x} \int_{r_x}^{\frac{L_w}{\tan(\phi_h)}} \frac{\lambda}{\left(x^2+L_w^2\right)^{\frac{\alpha_L}{2}}} dx dr_x + \left(F_{\beta-\theta}G_m G_m + \overline{F_{\beta-\theta}}g_s G_m\right)\int_{\frac{L_w}{\tan(\phi_h)}}^{\infty} \frac{\lambda\left(1-e^{-\lambda x}\right)}{\left(x^2+L_w^2\right)^{\frac{\alpha_L}{2}}} dx\Bigg), \quad (5.40)$$

and (5.41) is the algebraically simplified version of (5.40), stated as

$$\mathbb{E}\left(I_{\text{adj.}}|r_y\right)_2^{V_C} = P_t A\overline{q_{\text{own}}}q_{\text{own}}\Bigg(F_{\beta-\theta}G_m G_m\lambda\int_{\frac{L_w}{\tan(\phi_h)}}^{\infty}\frac{1-e^{-\lambda x}}{x^2+L_w^2}dx + \overbrace{\overline{F_{\beta-\theta}}g_s G_m\lambda\int_{\frac{L_w}{\tan(\phi_h)}}^{\infty}\frac{1-e^{-\lambda x}}{x^2+L_w^2}dx}^{\text{Minor Impact}}$$

$$+\overbrace{\frac{\lambda^2\left(F_{\beta-\theta}g_s G_m + \overline{F_{\beta-\theta}}g_s g_s\right)}{L_w}\int_0^{\frac{L_w}{\tan(\phi_h)}} e^{-\lambda r_x}\left(\frac{\pi}{2}-\phi_h-\tan^{-1}\left(\frac{r_x}{L_w}\right)\right)dr_x}^{\text{Minor Impact}}\Bigg). \quad (5.41)$$

The mean-interference of D-type vehicles for Case 2, $\mathbb{E}\left(I_{\text{adj.}}|r_y\right)_2^{V_D}$, is dependent on, $\mathbb{E}\left(\sum_{i\epsilon\Phi_{\text{adj.}}}\left(\sqrt{x_i^2+L_w^2}^{-\alpha_L}\right)|r_y\right)_2$ which can be expressed as

$$\mathbb{E}\left(\sum_{i\epsilon\Phi_{\text{adj.}}}\left(\sqrt{x_i^2+L_w^2}^{-\alpha_L}\right)|r_y\right)_2 = \int_0^{\infty}\lambda e^{-\lambda r_x}\int_{r_x}^{\infty}\frac{\lambda}{\left(x^2+L_w^2\right)^{\alpha_L/2}}dx dr_x, \quad (5.42)$$

which becomes after algebraic manipulation

$$\mathbb{E}\left(\sum_{i\epsilon\Phi_{\text{adj.}}}\left(\sqrt{x_i^2+L_w^2}^{-\alpha_L}\right)|r_y\right)_2 = \int_0^{\infty}\lambda^2 e^{-\lambda r_x}\left(\frac{\pi}{2}-\tan^{-1}\left(\frac{r_x}{L_w}\right)\right)dr_x. \quad (5.43)$$

When (5.43) is combined with $F_{\beta-\theta}$ from both the *typical* receiver and interferer

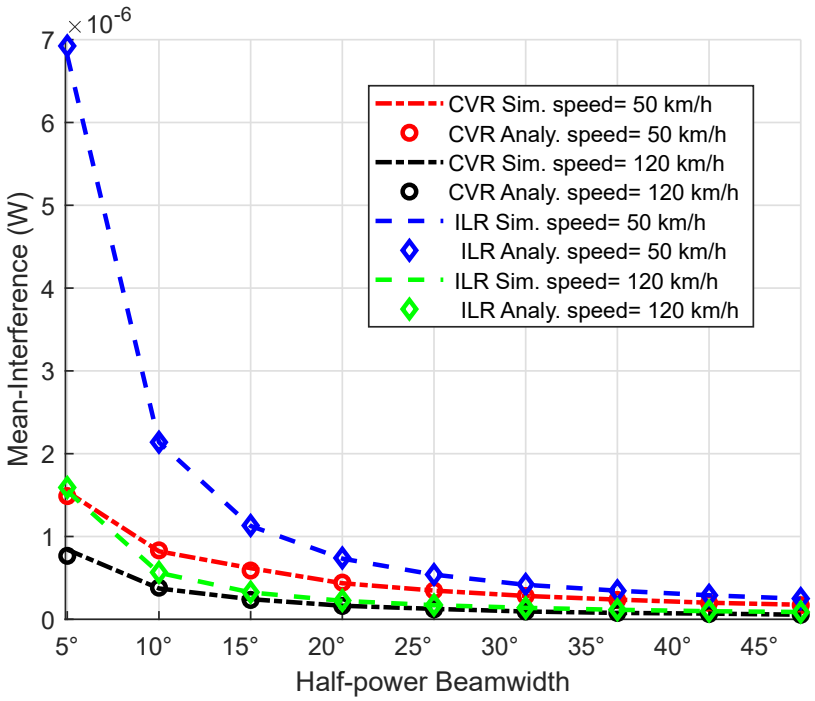

Figure 5.4: Mean-interference versus the half-power beamwidth for various vehicular speeds, where $L_w = 3\,\mathrm{m}$, $g_s = 0.1$, $m = 3$, $h_t = 0.5\,\mathrm{s}$.

point of view, $\mathbb{E}\left(I_{\text{adj.}}|r_x\right)_2^{V_D}$ results as

$$\mathbb{E}\left(I_{\text{adj.}}|r_x\right)_2^{V_D} = \frac{P_t A \overline{q_{\text{own}}}^2}{L_w}\left(F_{\beta-\theta}^2 G_m G_m + \overbrace{2F_{\beta-\theta}\overline{F_{\beta-\theta}} G_m g_s + \overline{F_{\beta-\theta}}^2 g_s g_s}^{\text{Minor Impact}}\right) \cdot \lambda^2 \int_0^\infty e^{-\lambda r_x}\left(\frac{\pi}{2} - \tan^{-1}\left(\frac{r_x}{L_w}\right)\right) dr_x. \tag{5.44}$$

Finally, the total mean-interference of the CVR scheme can be approximated as follows

$$\mathbb{E}_{\text{CVR}}\left(I\right) \approx P_t A G_m G_m \lambda \Bigg(\lambda e^{\lambda h_c} \Gamma\left(0, \lambda h_c\right)\left(q_{\text{own}} q_{\text{own}} + q_{\text{own}}\overline{q_{\text{own}}} F_\beta\right) + \frac{q_{\text{own}} q_{\text{own}}}{L_w}\phi_h + \frac{q_{\text{own}}\overline{q_{\text{own}}}}{L_w} F_\beta \phi_h + \left(\overline{q_{\text{own}}} q_{\text{own}} F_\beta \lambda + \overline{q_{\text{own}}}^2 F_\beta^2 \lambda\right)\left(\frac{1 - e^{-\lambda\sqrt{h_c^2 + L_w^2}}}{\lambda\sqrt{h_c^2 + L_w^2}} + \Gamma\left(0, \lambda\sqrt{L_w^2 + h_c^2}\right)\right) + \overline{q_{\text{own}}} q_{\text{own}} F_\beta \int_{\frac{L_w}{\tan(\phi_h)}}^\infty \frac{1 - e^{-\lambda x}}{x^2 + L_w^2} dx + \frac{\overline{q_{\text{own}}}^2}{L_w} F_\beta^2 \lambda \int_0^\infty e^{-\lambda r_x}\left(\frac{\pi}{2} - \tan^{-1}\left(\frac{r_x}{L_w}\right)\right) dr_x \Bigg). \tag{5.45}$$

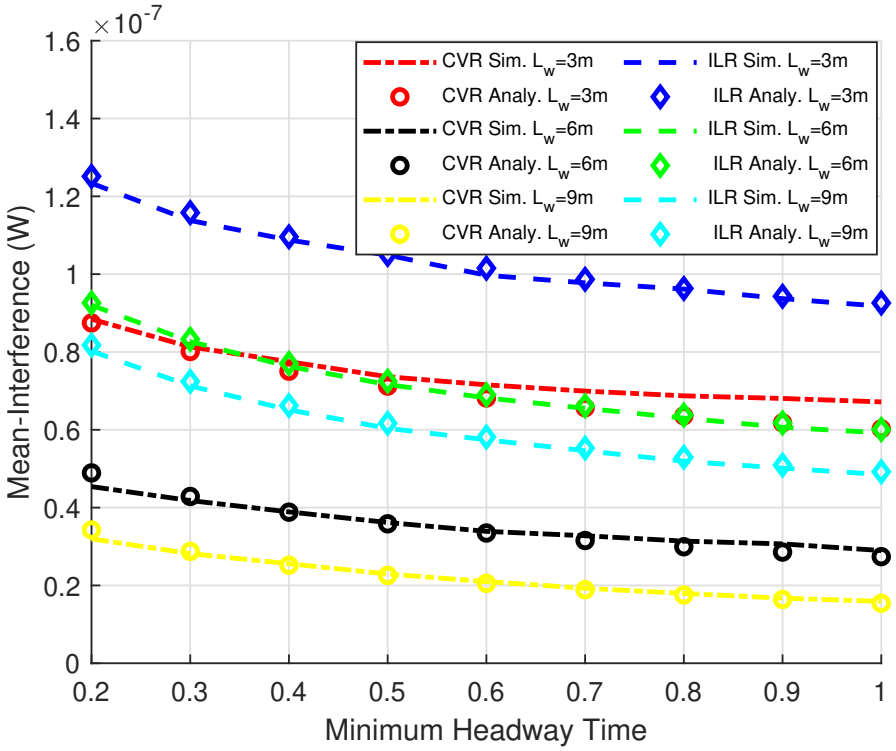

Figure 5.5: Mean-interference versus the minimum headway time for various lane widths, where $\phi = 15°$, $g_s = 0.1$, $m = 3$, $v = 90\,\text{km/h}$.

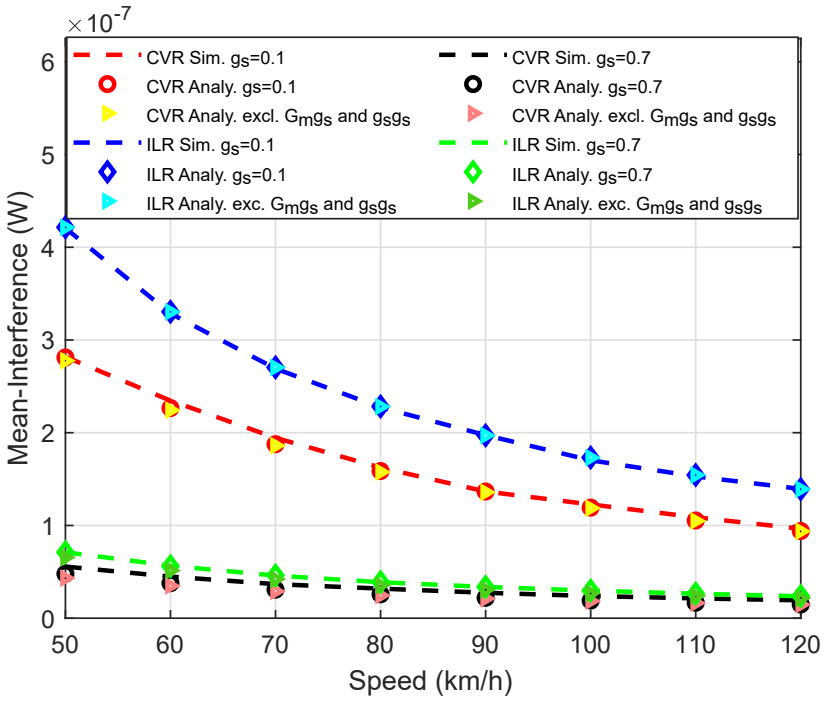

Figure 5.6: Mean-interference versus the vehicular speed for different side lobe gains, where $L_w = 3\,\text{m}$, $\phi = 30°$, $h_t = 0.5\,\text{s}$ and $m = 3$.

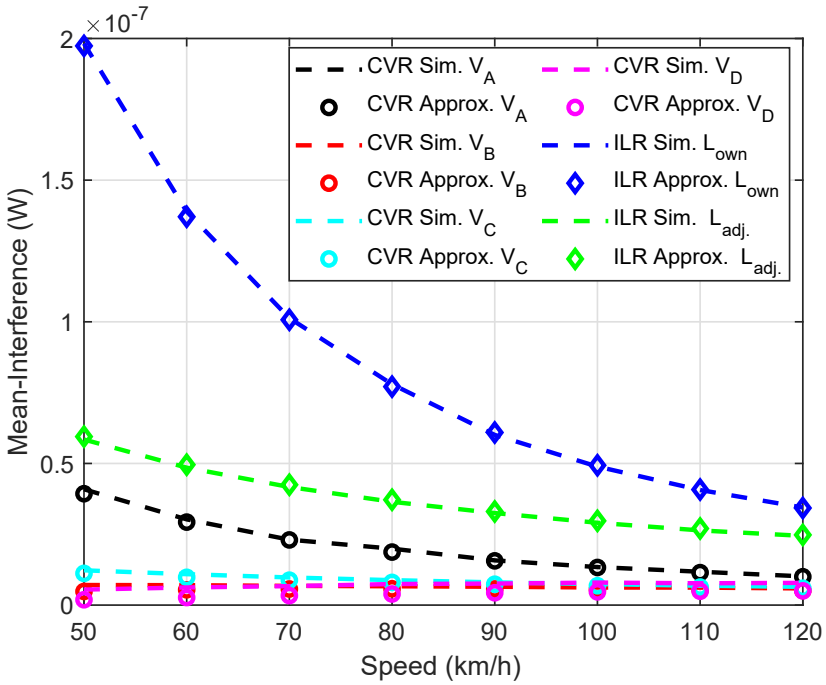

Figure 5.7: Mean-interference versus the vehicular speed for different vehicle and lane types, where $g_s = 0.5$, $\phi = 15°$, $m = 3$, , $h_t = 0.5\,\text{s}$, and the lane separation distance is 9 m.

5.3 Discussion

The results obtained through analytical modelling and Monte Carlo simulations are presented in Fig. 5.4, 5.6 and 5.7, and display only minor differences between both methods. The Monte Carlo simulations are carried out by means of a random distribution of nodes on two lines as an application of shifted PPP. In each case, the mean-interference is calculated for more than 10^5 times, and the typical simulation limit is set at 5 km. Note that the presented mean-interference results in Figures 5.4- 5.7 are in Watt.

In Fig. 5.4, it is observed that the half-power beamwidth and mean-interference are inversely proportional for both the ILR and CVR schemes. Intuitively, one might expect that increasing the beamwidth increases the probability of being interfered for the *typical* receiver, thus, the resulting interference should be higher when the beamwidth is increased. Even though an increase in beamwidth increases the probability of being interfered, conversely, this causes a decrease in G_m which has a dominant effect on the system's performance. Moreover, in Fig. 5.4, the transition from a low vehicle density, $\lambda = 0.015$, to a high density, $\lambda = 0.036$, and the relation between vehicle density and speed explained earlier, causes a significant mean-interference increase in the ILR scheme especially for narrow beamwidths, whereas this transition causes a much smaller increase in the mean-interference when the CVR scheme

is employed. In other words, the CVR scheme is much more resistant to changes in beamwidth and vehicular density. Intuitively, if the receiver of any transmitter is located in the adjacent lane, which is only possible in the CVR scheme, then the antenna beam of that transmitter will be directed away from the the road's direction after some point, which can be observed from the relationship of B- and C-type vehicles in Case 1, Fig. 5.1b. On the other hand, the beam of any transmitter/interferer in the ILR scheme will always remain directed along the road as in Fig. 5.1a.

In Fig. 5.5, the relationship between mean-interference and minimum headway time relationship for different lane widths is examined. In this setup, the hardcore distance between two consecutive points from point processes point of view can be travelled by minimum headway time in x-axis of Fig. 5.5 given that speed of vehicles is 90 km/h. It is observed that the mean-interference is increasing with decrease in minimum headway time. The reason of this phenomenon is that shorter minimum headway time reduces the distance between interferer and *typical* receiver, hence causes higher interference. Additionally, this trend is valid for both routing schemes. Remember that the analytical model implements the shifted homogeneous PPP and the simulation implements hard-core PPP. Accordingly, those two methods produce similar results for minimum headway time requirements typically less than 0.6s. As an illustration of this phenomenon, there is a diversion between analytical and simulation results of CVR scheme after 0.6s in Fig. 5.5.

In Fig. 5.6, it can be clearly observed that an increased vehicle density increases the mean-interference. Even though the CVR scheme outperforms the ILR scheme under all conditions, a comparison of Fig. 5.4 and 5.6 reveals a strategy in which a transition from the CVR scheme to the ILR scheme is meaningful. Considering that in the CVR scheme it is harder to sustain a link for a long duration due to the fundamental behaviour of traffic patterns, and that the scheme causes a topologically more complex network, if the difference in performance between CVR and ILR is small, then switching to the ILR scheme is the smarter and simpler choice. Hence, as is inferable from Fig. 5.4 and 5.6, for low density and wide beamwidths the ILR scheme is the preferred choice.

Additionally, Fig. 5.6 illustrates that in comparison to main-to-main antenna beam alignment, $G_m G_m$, both main-to-side alignment, $G_m g_s$, as well as side-to-side alignment, $g_s g_s$, have a minor impact on the system performance, even for considerably wide beamwidths and large side lobe gain. Whereas for $\phi = 30°$ and $g = 0.7$ the ratio of G_m/g_s is only 6.14, and for $g = 0.1$ and $\phi = 30°$ this ratio is 109, the arrow markers in Fig. 5.6 show that the analytical results for these parameters, neglecting all $G_m g_s$ and $g_s g_s$ cases and replacing $F_{\beta-\theta}$ with F_β, match very well with the simulation and analytical results that

include them. Hence, the system designers should focus on interferences that arise from main-to-main alignments. Moreover, this enables discarding all main-to-side and side-to-side alignment components from the analytical results, and using the closed-form F_{β} instead of $F_{\beta-\theta}$, which results in a significantly simpler analytical model.

Finally, Fig. 5.7 depicts the system performance in the dependence of the mean-interference on the speed of the vehicle types. In this analysis, the employed analytical model is an approximation for $3L_w$, the fourth lane case; $g_s g_s$ and $G_m g_s$ alignments are discarded; $F_{\beta-\theta}$ and q_{own} are replaced by F_{β} and (5.21). The good match between the simulation results and the analytical approximation shows that the shifted PPP-like model and the discarding of $G_m g_s$ and $g_s g_s$ alignments are appropriate. Furthermore, Fig. 5.7 illustrates that the presented model can be extended for a larger number of lanes. In the CVR scheme, A-type and C-type vehicles are the most interference generating vehicles, whereas the largest difference between the simulation and analytical approximation occurs for D-type vehicles. However, since the impact of D-type vehicles is minor, the resulting total interference does not change significantly. Noticeably, the own lane interferers in the ILR scheme are more powerful than the adjacent lane interferers. Likewise, the interferers which *typical* transmitter and receiver pair is located in the same lane cause more interference when the CVR scheme is employed.

5.4 Conclusions

In this chapter, the performances of two baseline routing schemes, namely, In-lane Routing and Closest Vehicle Routing, for mmWave V2V communications are analytically modelled in terms of their mean-interference. Moreover, it is shown that under the platooning based headway requirements the shifted homogeneous PPP can fairly produce accurate model to represent distribution of autonomous vehicles on roads. Furthermore, it is found that the impact of main-to-side and side-to-side lobe gain interference is shown to be negligible. That leaded a significantly simpler analytical model which is verified by Monte Carlo simulations. Furthermore, it is show that the probability of the closest vehicle being located in the own lane under CVR scheme is simply exponentially decreasing with multiplication of vehicular density and minimum headway distance. Plus, It is found that the CVR scheme outperforms the ILR scheme in all investigated scenarios, yet, the difference is minor for low density and wide beamwidth regimes. Furthermore, the ILR scheme can be substantially improved by limiting the in-lane interference through orthogonal resource allocation or utilizing the sensitivity of mmWave communications to blockages by appropriate antenna placement on vehicles.

Chapter 6

Multi-Lane Urban mmWave V2V Networks: A Path Loss Behaviour Dependent Coverage Analysis

In this chapter, a tractable analytical model for an in-lane routing scheme that approximates the coverage, rate coverage, and road spectral efficiency of mmWave urban Vehicle-to-Vehicle networks is proposed. The analytical model is proposed for three different path loss behaviour scenarios, namely, Line-of-Sight, Non-Line-of-Sight, and Obstructed-Line-of-Sight. Each scenario is based upon corresponding, previously reported, experimental mmWave measurements and path loss models. Building upon Chapter 3, a 4-lane road layout is considered, hence the impact of inter-lane blockage and adjacent lanes interferers are taken into account. It is shown that Non-Line-of-Sight behaviour provides the best performance in coverage, but the lowest reliability. Moreover, the careful choice of link distances, i.e. forcing communication to be limited to the nearest vehicle, removes the sensitivity of the system to interferences from increased vehicle density, which is an important result to be considered in dense urban networks. Additionally, it is found that narrowing the beamwidth significantly improves the performance, which is the result of eliminated interferences, rather than a corresponding increase in antenna gain. The results of this research will impact both communications systems infrastructure designers and vehicle manufacturers looking to balance system performance in the investigated scenarios.

6.1 Introduction

The inertia behind measuring and modelling the mmWave channel is growing within the research community. For instance, radar applications are being developed at 77 GHz [110]. V2V and in-vehicle channel models, and their corresponding path loss exponent and delay spread are presented in [91] and [44] for 60 GHz. V2V excess loss and delay spread when the transceiver antennas are located near the vehicular headlight in an engine bay are presented in [75] for a carrier frequency range of 25-84 GHz. Furthermore, [111] measured the contact time of V2I links at 60 GHz, whereas [112] investigated the blockage effect of a single vehicle in an open area at 28 GHz. Further, [113] studied the time-variance of the vehicular infrastructure-to-infrastructure channel for 60 GHz. Additionally, [114] measured the effect of multipath and direct interference from side lanes for V2V communications at 79 and 300 GHz with a 30° beamwidth, and states that even for short distances, up to 20 m, interferences caused by scattering from metallic, plastic, and glass vehicular surfaces are marginal. In addition, [115] proposed a switching framework between mmWave and terahertz V2X communications.

As it has been introduced in Chapter 2, the 3rd Generation Partnership Project (3GPP) models ranging from 0.5 to 100 GHz [116], and the Close-In (CI) and alpha-beta-gamma (ABG) models [44, 117] are the mainstream channel models utilized in the literature. Each model is known to have its advantages and disadvantages. For instance, the ABG model underestimates or overestimates the path loss under specific circumstances where the link distance is considerably short or long. The 3GPP and CI models perform similarly with subtle differences [90].

In addition, [69] characterized the 60 GHz V2V channel model by placing a transmitter antenna at a height of 1.03 m, which is approximately the windshield region of the vehicle, while the receiver antenna was positioned in the height range from 0.4 m to 1.8 m for a varying number of obstructing vehicles in-between the transmitter and receiver. Furthermore, [118] modelled the channel characterization of V2V communications in the presence of vehicle blockages for 6.75 , 30 , 60 , and 73 GHz. It was found that the position of the blockage relative to the transmitter/receiver antennas plays a crucial role and that the frequency dependence of the channel response is limited. This point reveals that the overall network performance will be substantially different depending upon the position of the antennas. Accordingly, this chapter aims to aid the vehicle manufacturing and telecommunications industry by exploring the system level performance of mmWave V2V communications for different path loss behaviours depending upon the antenna position. As is inferable from Table 2.1 in Chapter 2, existing models have considered neither multi-lane

mmWave V2V communications nor the impact of antenna placement. Hence, this chapter, which is under review in Elsevier Vehicular Communications, addresses this by characterizing the potential path loss behaviours and their expected performance to help vehicle manufacturers to optimize the network performance.

Throughout this chapter, it is assumed that: there is a *typical* receiver [119], which is located at the centre of the network; there is a corresponding *typical* transmitter located at another pre-set location in the same lane; all vehicles are located at the centre of their lanes; and the overall system performance is measured through the quality of the link between the transmitter-receiver pair. The aim of this work is to enhance the characterization of the performance of urban mmWave V2V networks. In meeting this aim, the following contributions are made:

- The coverage probability, rate coverage probability, and road spectral efficiency are characterized for multi-lane mmWave V2V networks through a stochastic geometry model that is built on a time-independent mono-dimensional Poisson Point-like Process (PPP-like), where each node is separated from the closest node by some set distance h_c, and validated numerically. Specifically, the final model presents the impact on performance of link distance, density of interferers and their distributions for varying numbers of lanes, beamwidth, and antenna gain.

- The proposed model is extended with various path loss behaviours and corresponding propagation characteristics, in order to provide design insights to optimize the performance of mmWave V2V networks, such as finding the best-performing path loss behaviour. The coverage, rate coverage, and road spectral efficiency are stochastically modelled with the transceiver antennas subjected to the following path loss behaviours: (i) LOS path loss behaviour except for large vehicles; and (ii) NLOS path loss behaviour for all vehicles; and (iii) OLOS (Obstructed-Line-of-Sight) path loss behaviour, with path loss depending on the number of vehicle blockages. Corresponding real-world, measurement-based path loss and blockage model parameters are used for each case.

- A multi-lane model, which is extendable for different numbers of lanes, is proposed. In addition, for each path loss behaviour, the blockage probabilities of the obstructing vehicles that are located in the same, adjacent, and outer lanes are evaluated.

- It is found that the impact of any type of NLOS, main-to-side and side-to-side lobe gain interference is almost negligible. In addition, under the in-lane routing scheme, narrowing the beamwidth significantly

improves coverage for angles typically smaller than 30°. Rather than increasing the antenna gain by narrowing the beamwidth, this improvement mainly comes from the fact that the probability of being interfered decreases. This shows that low-gain, low-energy-consuming antennas can be used instead of high-gain antennas without affecting the performance considerably.

6.2 System Model and Scenarios

The system model proposed in this chapter estimates the coverage performance of mmWave V2V networks in an urbanized environment. Diagrammatically, the path loss behaviour options and the scenarios of interest are shown in Fig. 6.1. The performance depends on the distribution and density of the vehicles, the antenna gain and beamwidth, the path loss, and the blockage. For this reason, the system model that is built on the following assumptions and remarks based on practical knowledge of vehicular-oriented mmWave measurements is characterized.

6.2.1 Node Distribution

Transforming the behaviour of vehicles on the road into a realistic and appropriate stochastic distribution is a fundamental step in building an analytical model. The nodes/vehicles are distributed on infinitesimal lines/lanes in a time-independent, mono-dimensional, hardcore distance separated, PPP-like process with density λ. The average distance between neighbouring nodes is λ^{-1} for a homogeneous PPP. As homogeneous PPP allows nodes to be very close, and considering vehicular dimensions and their tracking distance, nodes/vehicles are separated from each other by a hardcore distance h_c. As future vehicles will become autonomous and apply platooning, the headway time is reduced to 0.5 s instead of 2 s used in previous work [105]. The work in [120] has shown that the string stability of platooning up to six cars is safe for a 0.5 s-0.7 s headway time, when cooperative adaptive cruise control systems are employed. For a given traffic flow at 90 km/h, equivalently 25 m/s, the average headway distance then is 50 m with 2 s travel. Considering that the average distance between neighbouring nodes is λ^{-1} for a homogeneous PPP, this means that $\lambda^{-1} = 50$ m. Hence, h_c is modelled as the headway time of 0.5 s multiplied with the traffic flow speed, that equals to $0.5\lambda^{-1}$, which will be shown to provide a realistic model and a fair match between the Monte Carlo simulations and the analytical results.

In Fig. 6.2, results from a Monte Carlo simulation and the traffic simulator PVT Vissim are compared. For the latter, the simulation was carried out

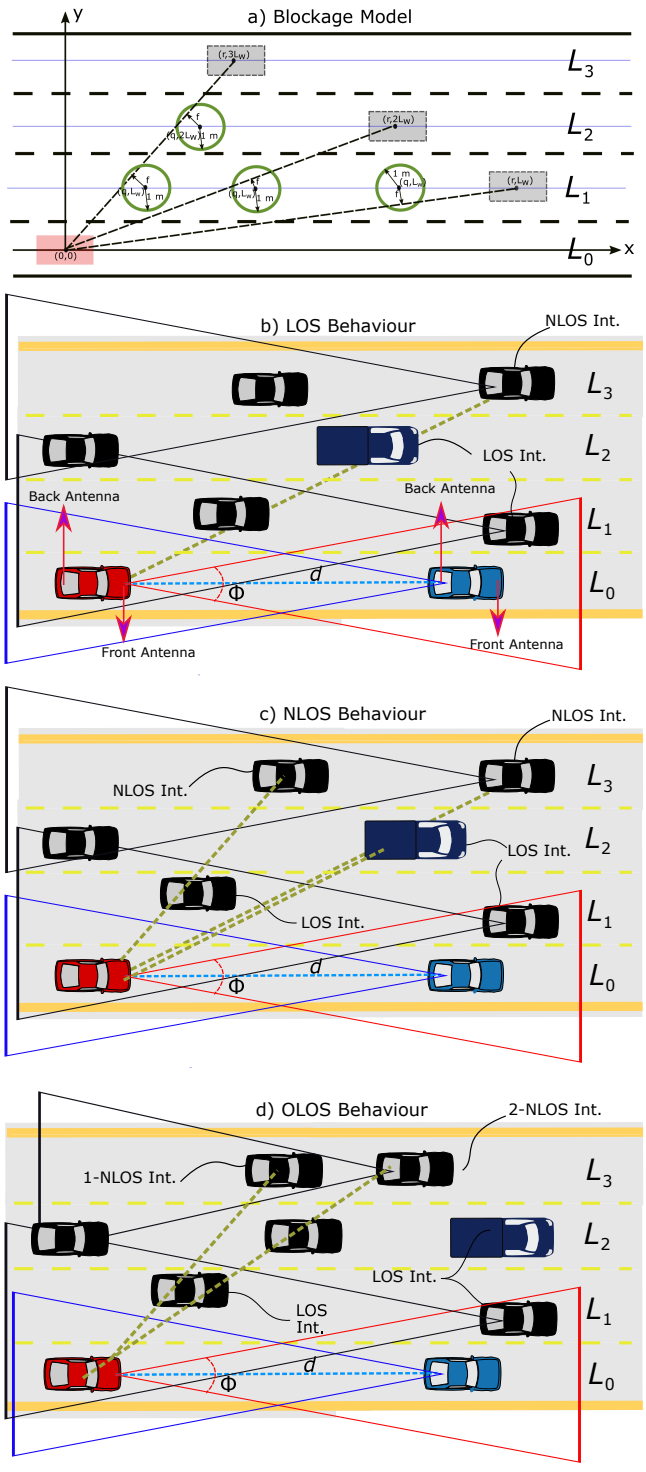

Figure 6.1: Illustrations for (a) the blockage model for adjacent lane vehicles, (b) LOS behaviour, (c) NLOS behaviour, and (d) OLOS behaviour on a 4-lane road layout. The red and light blue vehicles are the *typical* receiver and transmitter, respectively, whereas the black and dark blue vehicles are interferers and large vehicles. If an interferer is inside a *typical* receiver's main antenna beam (triangle), this causes main-to-main lobe interference, else side-to-side lobe interference applies.

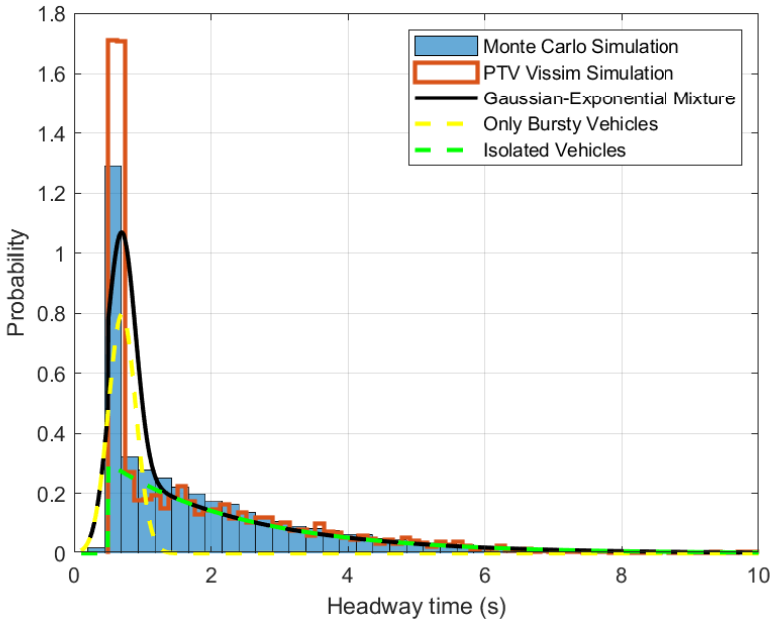

Figure 6.2: Relationship between the average headway time and its probability, for $\lambda = 0.02$ in a Monte Carlo simulation, and for a traffic flow of 1800 vehicles per hour per lane in a PTV Vissim simulation, where the selected parameters for the Gaussian-Exponential models [121] are $w_g = 0.4$, $\mu_g = 0.7$, $\sigma_g =$, $w_e = 0.6$, $\mu_e = 0.7$, and $m_s = 0.5$.

under free lane selection, with the ability to platoon up to seven vehicles, and using the headway time distribution model from [121]. Clearly, there is fair match between both results. In [121], an analytical model has been generated for a headway time distribution that is based on measured data for 4-lane traffic in Madrid, Spain. The model proposed a combination of Gaussian and exponential distributions in which the vehicles that travel close to each other follow a Gaussian distribution and are referred to as *bursty* vehicles, and the vehicles that drive independently follow an exponential distribution and are referred to as *isolated* vehicles. Thereby, Fig. 6.2 illustrates that the shifted PPP-like model matches well with the measurement-based Gaussian-Exponential mixture, including both *bursty* and *isolated* vehicles. Hence, the resulting probability distribution of the headway time is given as

$$f_h(t) = w_g \frac{1}{\sigma_g \sqrt{2\pi}} e^{-\frac{1}{2}\left(\frac{t-\mu_g}{\sigma_g}\right)^2} + w_e \mu_e e^{-\mu_e (t-m_s)}, \tag{6.1}$$

where w_g and w_e are the weights of *bursty* and *isolated* vehicles, μ_g and σ_g are the mean and standard deviation of the Gaussian distribution, and μ_e and m_s are the rate and shifting parameters of the exponential distribution, respectively. Hence, it is shown that the proposed shifted PPP-like model for

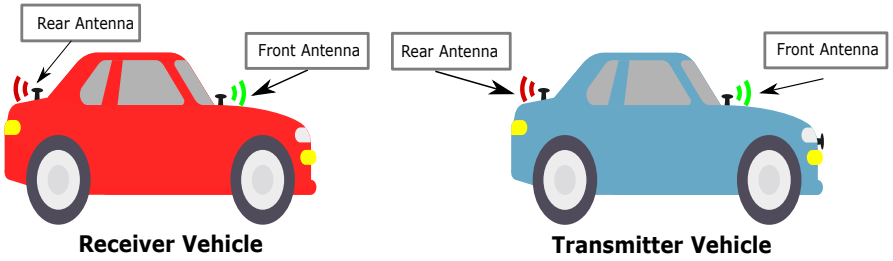

Figure 6.3: The front and rear antenna placements on the transmitter and receiver vehicles.

the traffic of autonomous vehicles has realistic applicability at large extent.

Due to the high path loss experienced in mmWave communication, a threshold distance, R_m, is specified in order to ease computational burden. Any interferer that is located beyond R_m is not considered throughout the analysis. Also, the width of all lanes, L_w, is assumed to be equal. Additionally, lanes are represented by the notation L_0, L_1, L_2 and L_3, with the assumption that 4 lanes exist following the architecture of primary 'A' urban roads in the United Kingdom. For simplicity, it is also assumed that the *typical* receiver is located in L_0 and its location is set as the origin, $\{0, 0\}$, of the coordinate system. Note that this does not cause loss of generality, as explained by Slivnyak's Theorem [106] in Chapter 2.

6.2.2 Path Loss Behaviours

Path loss characterization of mmWave signals is highly dependent upon both the existence of blockages and the material they are made of. For example, the blockage level of the windshield and the entire metallic body of any obstructing vehicle are considerably different. Hence, the blockage of mmWave propagation depends on the location of the transmitter and the receiver antennas on/in the vehicle.

For instance, [122] has measured the antenna location dependent path loss for mmWave V2V communications where the antennas are raised 0.6 m above the ground and the beamwidth of the transmitting antenna is 30°, whereas the receiver antenna is omnidirectional. Their findings state, that if the transmitter vehicle uses its rear antenna and the receiver vehicle uses its front antenna, as shown in Fig. 6.3, the link will be subject to free space path loss only. Whereas if the transmitter vehicle uses its front antenna, and the receiver vehicle uses either of its antennas, the resulting path loss will be 125 dB due to the blockage by the metallic body of the transmitter vehicle, even for a 10 m separation. Thus, one can clearly state, that a signal originating from a front antenna of the transmitter vehicle has no impact on the receiver vehicle.

Table 6.1: Original vehicular path loss parameters

	A_i^o	α_i^o
Obstacle-free (0-LOS)	1.77	70
1 Vehicle (1-NLOS)	1.71	78.6
2 Vehicle (2-NLOS)	0.635	115
3 Vehicle (3-NLOS)	0.362	126

6.2.3 Antenna Gain Model

Main lobe and side lobe antenna gains are modelled as per [62] for Device-to-Device (D2D) communications, and applied in Chapter 5. As it is illustrated in Fig. 6.1, if an interferer vehicle leaves the main beam (triangle) of the *typical* receiver, then the *typical* receiver will leave the transmitter beam triangle of the interferer simultaneously. Hence, main-to-side lobe interference is not possible.

6.2.4 Vehicular Path Loss Models

Two main path loss models are implemented throughout this chapter. Firstly, the CI path loss model, $\mathcal{P}_{A,\alpha_{L/N}}$, as previously introduced in Chapter 2, is specifically designed for general mmWave communications by [90] after a significant number of measurement trials were carried out. Since mmWave propagation is very sensitive to blockages, the path loss exponent in (2.1) will be evaluated for LOS (α_L) and NLOS (α_N) cases.

The second implemented path loss model, named as OLOS in this chapter, is based on V2V-measurements at 60 GHz in [69], and given as

$$\mathcal{P}_{A_i^o,\alpha_i^o} = d^{-A_i^o} 10^{-\frac{\alpha_i^o}{10} - \frac{15d}{10^4}}, \tag{6.2}$$

where A_i^o and α_i^o are the parameters that shape the blockage effect of obstructing vehicles between the *typical* transmitter and receiver. The ratio of the received and transmitted power varies by the number of obstructing vehicles. If there is no obstructing vehicle between the *typical* transmitter and receiver, this is named as 0-LOS, which is different from OLOS, and the A_0^o and α_0^o parameters from Table 6.1 are used. Alternatively, in the cases of 1, 2, or 3 obstructing vehicles, then the A_1^o, α_1^o (1-NLOS); A_2^o, α_2^o (2-NLOS); or A_3^o, α_3^o (3-NLOS) pairs are implemented, respectively. Even though the model can be extended to more than 3 obstructing vehicles by implementing the CI path loss model with NLOS configuration, due to the extremely weakened signals, the path loss of the transmitting nodes for a higher number of obstructing vehicles is considered to be infinite and their interference is ignored in the analysis. The parameters presented in Table 6.1 are obtained from [69] where the cumulative probability distribution plot of the measurements meets 50% in order to provide a mean

value. Note that V2V measurements at 30 GHz, 60 GHz, and 73 GHz carrier frequencies in the presence of vehicle blockages have only shown a limited frequency dependence [118]. Hence, the OLOS path loss model can be used for other mmWave carrier frequencies with minor changes.

6.2.5 Blockage Models

The nature of mmWave communications being very sensitive to blockages, strongly motivates researchers to realistically model the blockages from intermediate vehicles in lanes and between lanes.

In the case where the transceiver antenna is subject to LOS path loss behaviour, it is assumed that all the links within a reasonable communications range, and until blocked by a large vehicle, are accepted as LOS regardless of the lane of the interferer vehicle, as shown in Fig. 6.1b. If the large vehicle is located in the same lane, vehicles beyond the large vehicle will interfere with the *typical* receiver as NLOS. And if the large vehicle is located in one of the adjacent lanes, it is represented as a circle with 1 m radius, i.e. half the width of an average vehicle [123]. Typically, the width of vehicles, including passenger vehicles and buses, ranges from 1.5 m to 2.5 m. Hence, for analytical convenience the circle radius is set as 1 m. If a straight line from the interferer to the *typical* receiver crosses such circle, the link is assumed to experience NLOS interference, as shown in Fig. 6.1a.

The equation of such line from the nearest lane, L_1, is $y = \frac{L_w}{r}x$, where r, x and y are the position of the interferer, the distance between the *typical* receiver and the interferer in the direction of travel, and the width of the lanes/road, respectively. Note that for L_1, if the vehicle nearest to the interferer vehicle located at L_1 does not form a blockage, the corresponding link is LOS. Assuming the location of the nearest vehicle to the interferer in the same lane, $\{q, L_w\}$, the probability of the distance between a line and a point to be shorter than 1 m can be expressed as $\mathbb{P}\left(\frac{rL_w - L_w q}{\sqrt{r^2+L_w^2}} < 1\right)$. Hence, for $p = r - q$, the probability can be written as

$$\mathbb{P}\left(p < \frac{\sqrt{r^2 + L_w^2}}{L_w}\right) = \int_{h_c}^{\frac{\sqrt{r^2+L_w^2}}{l}} \lambda e^{-\lambda(p-h_c)} dp. \tag{6.3}$$

As the distance between adjacent nodes follows an exponential distribution, and applying the hardcore distance h_c, the blockage probability can be expressed as the integral of a shifted exponential distribution. Hence, by taking the complimentary probability, the probability of establishing a LOS link for L_1

interferers is given by

$$f_{L_1}(r) = e^{\frac{-\lambda\eta\sqrt{r^2+L_w^2}}{L_w}} e^{\lambda h_c}. \tag{6.4}$$

Similarly, for the L_2 interferers, the blockage probabilities are caused by vehicles located in L_1. Hence, the blockage probability of L_2 interferers, $\mathbb{P}\left(\frac{rL_w - 2L_w q}{\sqrt{r^2+4L_w^2}} < 1\right)$, can be expressed as $\mathbb{P}\left(p < \frac{\sqrt{r^2+4L_w^2}}{2L_w}\right)$, for $p = r/2 - q$. Thus, the probability of establishing a LOS link for L_2 interferers is given by

$$f_{L_2}(r) = e^{\frac{-\lambda\eta\sqrt{r^2+4L_w^2}}{2L_w}}. \tag{6.5}$$

Using a similar approach, establishing a LOS link for the L_3 interferers is given by

$$f_{L_3}(r) = e^{2\frac{-\lambda\eta\sqrt{r^2+9L_w^2}}{3L_w}}, \tag{6.6}$$

where λ and η are the density of vehicles per lane and the ratio of large vehicles. Because establishing a LOS link for L_3 interferers depends on the vehicles located in both L_1 and L_2, (6.6) is a squared equation.

For the NLOS path loss behaviour, the first/nearest interferer that is located in the *typical* receiver's lane is CI LOS, whereas for the other vehicles located in the same lane the CI NLOS path model is used, as shown in Fig. 6.1c. In the case of OLOS behaviour, the classification of the links are related to the number of obstructing vehicles which the mmWave signal has to propagate through. For an in-lane interferer that is located in the *typical* receiver's lane, L_0, if the mmWave signal has propagated through one, two or three vehicles, then the 1-NLOS, 2-NLOS, or 3-NLOS path loss models are implemented, respectively. Interferences will be ignored if there are more than three vehicles to propagate through, as shown in Fig. 6.1d, because the path loss becomes very high. Finally, Table 6.2 summarizes the relationships of different path loss and blockage models for each lane.

Table 6.2: Path loss models and blockage relationships

	Interferer Location	**Own Lane - L_0**	**Adj. Lanes - L_1-L_2**	**Outer Lane - L_3**
LOS B.	**Receiver antenna side (see Fig 6.1b)**	LOS until first large vehicle then NLOS	LOS w.p. (6.4)-(6.5) and NLOS w.p. complement of (6.4)-(6.5)	LOS w.p. (6.6) and NLOS w.p. complement of (6.6)
LOS B.	**Other side**	No interference due to self isolation/blockage of metallic body of *typical* receiver		
NLOS B.	**Receiver antenna side (see Fig 6.1c)**	First vehicle is LOS others are NLOS	LOS w.p. (6.4)-(6.5) and NLOS w.p. complement of (6.5)-(6.5) for $\eta = 1$	LOS w.p. (6.6) and NLOS w.p. complement of (6.6) for $\eta = 1$
NLOS B.	**Other side**	No interference due to self isolation/blockage of metallic body of *typical* receiver		
OLOS B.	**Receiver antenna side (see Fig 6.1d)**	First vehicle is 0-LOS others are OLOS	0-LOS w.p. (6.4)-(6.5) and 1-NLOS w.p. complement of (6.4)-(6.5) for $\eta = 1$	0-LOS w.p. (6.6) and 1-NLOS w.p. complement of square root of (6.6) 2-NLOS w.p. complement of (6.6) for $\eta = 1$
OLOS B.	**Other side**	No interference due to self isolation/blockage of metallic body of *typical* receiver		

6.3 Coverage and Rate Analysis

The signal-to-interference-plus-noise-ratio (SINR) for a *typical* receiver is given by

$$\text{SINR} = \frac{P_t G_m G_m h_o \mathcal{P}_L(d)}{\sum_{i \epsilon \Phi_{\text{LOS+NLOS+OLOS}}} P_t G_{i->t_r} G_{t_r->i} h_i \mathcal{P}_L(r) + N_0}, \tag{6.7}$$

where P_t is the normalized transmitter power, h_0 and h_i are the small-scale fading at the *typical* receiver for the *typical* transmitters and interferers, respectively, d is the distance between the *typical* transmitter and receiver, r is the distance in the direction of travel between the interferers and the *typical* receiver, and N_0 is the noise power. G_m represents the antenna gains of the *typical* transmitter and receiver, which are assumed to be aligned. In (6.7), the corresponding antenna gains of interferers are represented as $G_{i->t_r}$ and $G_{t_r->i}$. All the interferers in the activity region have a corresponding $\Phi_{\text{LOS+NLOS+OLOS}}$ process, which is the group of all interferers within the activity region. Additionally, $\mathcal{P}_L(d)$ and $\mathcal{P}_L(r)$ represent the path loss models for the *typical* transmitter and interferers which depend on link distance and the path loss models of (2.1), with more details in Chapter 2 and (6.2).

Lemma 1: The coverage probability of multi-lane mmWave V2V communications assuming that $h_0 \sim \Gamma(m, 1/m)$ in which m is an integer, is tightly bounded by

$$\mathbb{P}_c(\mathcal{T}) < \sum_{n=1}^{m} \binom{m}{n} (-1)^{n+1} \mathcal{L}_0 \mathcal{L}_1 \mathcal{L}_2 \mathcal{L}_3 \mathcal{N}, \tag{6.8}$$

where $\mathcal{N} = e^{\frac{-m(m!)^{-1/m} n \mathcal{T}}{P_t G_m G_m \mathcal{P}_L(d)} N_0}$. The proof of (6.8) can be found in Appendix A. $\mathcal{L}_0$, $\mathcal{L}_1$, $\mathcal{L}_2$, and $\mathcal{L}_3$ are Laplace transforms of interferences of vehicles located in the lanes L_0, L_1, L_2, L_3, respectively. The analytical coverage modelling of LOS, NLOS and OLOS path loss behaviours requires the individual treatment for all lanes due to the different path loss behaviours and reactions to blockages. Hence, hereafter the model branches for each lane and path loss behaviour.

6.3.1 LOS Behaviour

In this subsection, the analytical model is specifically characterized for the scenario in which all vehicles are subject to LOS behaviour, excluding large vehicles.

Lemma 2: Assuming $m = 1$ and $\alpha_L = 2$, the Laplace transforms of the own, adjacent and outer lanes of LOS behaviour are approximated as:

$$\mathcal{L}_0^L \approx e^{-\lambda \left(r \left(1 - {}_2F_1\left(-0.5, 1; 0.5; -\frac{\mathcal{T} d^2}{r^2}\right)\right)\Big|_d^{(\lambda\eta)^{-1}+d} \right)}, \tag{6.9}$$

$$\mathcal{L}_1^L \approx e^{-\lambda \int_{\frac{L_w}{\tan(\phi_h)}}^{R_m} \frac{\mathcal{T}d^2}{r^2+L_w^2+\mathcal{T}d^2} f_{L_1}(r)dr}, \tag{6.10}$$

$$\mathcal{L}_2^L \approx e^{-\lambda \int_{\frac{2L_w}{\tan(\phi_h)}}^{R_m} \frac{\mathcal{T}d^2}{r^2+4L_w^2+\mathcal{T}d^2} f_{L_2}(r)dr}, \tag{6.11}$$

$$\mathcal{L}_3^L \approx e^{-\lambda \int_{\frac{3L_w}{\tan(\phi_h)}}^{R_m} \frac{\mathcal{T}d^2}{r^2+9L_w^2+\mathcal{T}d^2} f_{L_3}(r)dr}, \tag{6.12}$$

respectively.

The proof of (6.9)-(6.12) can be found in Appendix B. It can also been seen that the coverage function is independent of the main lobe antenna gain, G_m, excluding its impact on the noise component of the in-lane routing scheme.

6.3.2 NLOS Behaviour

Following (6.8), all transmitter and receiver antennas are subject to NLOS behaviour. It is assumed that the first vehicle will be located at λ^{-1}, which requires the separation of the model into LOS and NLOS links for distances from 0 to λ^{-1}, and for those larger than λ^{-1}. The Laplace transforms of the own, adjacent and outer lane of NLOS behaviour are approximated as

$$\mathcal{L}_0^N \approx 1, \mathcal{L}_1^N = \mathcal{L}_1^L, \mathcal{L}_2^N = \mathcal{L}_2^L, \mathcal{L}_3^N = \mathcal{L}_3^L \text{ for } \eta = 1. \tag{6.13}$$

Since a *typical* transmitter acts as blockage for an L_0 interferer, it is observed that the impact of all L_0 interferers in NLOS behaviour is negligible. Also note that in NLOS behaviour all vehicles will act as large vehicles, hence setting $\eta = 1$ converts the Laplace transforms from LOS behaviour into NLOS behaviour.

6.3.3 OLOS Behaviour

The measurement-based OLOS path loss model (6.2) results in a challenging integral to solve. To simplify the integral of the Laplace transforms, (6.2) is transformed into

$$\bar{\mathcal{P}}_{A_i^t, \alpha_i^t} = A_i^t d^{-\alpha_i^t}, \tag{6.14}$$

through the use of non-linear regression that utilized single-term power series curve fitting tools. Note that typically path loss models are the product of curve fitting tools that utilized field measurement data. Thereby, the original parameters shown in Table 6.1 are replaced by the parameters in Table 6.3.

Note that for OLOS behaviour, the blockage impact of each vehicle is examined individually. Since the vehicles are distributed with mono-dimensional PPP, it is assumed that the vehicles are truncated uniformly distributed. In

Table 6.3: Transformed vehicular path loss parameters

	A_i^t	α_i^t
Obstacle-free (0-LOS)	$1.841 \cdot 10^{-7}$	2.024
1 Vehicle (1-NLOS)	$2.547 \cdot 10^{-8}$	1.964
2 Vehicle (2-NLOS)	$6.3 \cdot 10^{-12}$	0.890
3 Vehicle (3-NLOS)	$4.99 \cdot 10^{-13}$	0.6165

other words, the distribution boundaries of the first, second and third vehicle are $[d \quad 2\lambda^{-1}+d]$, $[2\lambda^{-1}+d \quad 4\lambda^{-1}+d]$, $[4\lambda^{-1}+d \quad 6\lambda^{-1}+d]$, respectively.

Lemma 3: The interference of each vehicle and corresponding Laplace transforms for the own, adjacent and outer lanes are given by:

$$\mathcal{L}_0^O \approx \frac{\lambda}{2} {}_2F_1\left(\frac{-1}{\alpha_1^t}, 1; \frac{\alpha_1^t - 1}{\alpha_1^t}; \frac{-A_1^t \mathcal{T}}{r^{\alpha_1^t} \mathcal{P}_{A_0^o, \alpha_0^o}(d)}\right) r \Bigg|_d^{2\lambda^{-1}+d}, \tag{6.15}$$

$$\mathcal{L}_1^O \approx e^{-\lambda \int_{\frac{L_w}{\tan(\phi_h)}}^{R_m} \frac{\mathcal{T} A_0^t}{\sqrt{r^2+L_w^2}^{\alpha_0} \mathcal{P}_{A_0^o, \alpha_0^o(d)+\mathcal{T}A_0^t}} f_{L_1}(r) dr}, \tag{6.16}$$

$$\mathcal{L}_2^O \approx e^{-\lambda \int_{\frac{2L_w}{\tan(\phi_h)}}^{R_m} \frac{\mathcal{T} A_0^t}{\sqrt{r^2+4L_w^2}^{\alpha_0} \mathcal{P}_{A_0^o, \alpha_0^o(d)+\mathcal{T}A_0^t}} f_{L_2}(r) dr}, \tag{6.17}$$

$$\mathcal{L}_3^O \approx e^{-\lambda \int_{\frac{3L_w}{\tan(\phi_h)}}^{R_m} \frac{\mathcal{T} A_0^t}{\sqrt{r^2+9L_w^2}^{\alpha_0} \mathcal{P}_{A_0^o, \alpha_0^o(d)+\mathcal{T}A_0^t}} f_{L_3}(r) dr}. \tag{6.18}$$

The proof of (6.15) is given in Appendix C, and the proof of (6.16)-(6.18) is very similar to the proof of *Lemma 2*.

For the calculation of the interference from adjacent and outer lanes, the mathematical methodology is very similar to the calculations for the LOS behaviour. The major difference is that for a transmitter in the outer lane, the blockage effect of a vehicle located in the adjacent lane is modelled with 1-NLOS or 2-NLOS parameters. Finally, insertion of (6.15), (6.16), (6.17), (6.18) into (6.8) results in the probabilities for OLOS behaviour.

6.3.4 Rate Coverage and Road Spectral Efficiency

The probability of the maximum achievable data rate, the rate coverage, can be calculated using the coverage probability, $\mathbb{P}_c(T)$, and the Shannon-Hartley Theorem as follows,

$$\mathbb{P}_{\text{Rate}}(R) = \mathbb{P}_c(2^{R/B} - 1) \tag{6.19}$$

where R and B are the maximum achievable data rate and the bandwidth. The rate coverage for each path loss behaviour is then obtained by adapting (6.8) for each case.

The Area Spectral Efficiency (ASE), which is introduced in Chapter 1,

Table 6.4: Main simulation parameters

Symbol	Parameter	Value
$r_{\min}$, R_m	Minimum and maximum interference distance	1 m and 1 km
λ	Vehicle density per lane	0.02 and 0.03
η	Large vehicle ratio in urban UK traffic	0.16 [124]
N_0	Thermal noise power	−174 dBm/Hz
B	Bandwidth	500 MHz
L_w	Average lane width	3 m
α_L and α_N	Path loss exponent for LOS and NLOS	2 and 4.5
f_c	Carrier frequency	60 GHz
g_s	Side lobe gain	0.25
P_t	Transmitter power	30 dBm
m	Small-scale fading factor	1

is given by [18] and represents the average number of bits transmitted per unit time, unit bandwidth and unit area. However, in this chapter, ASE is re-termed as Road Spectral Efficiency (RSE), because, firstly, it is assumed that the operating frequency range of mmWave V2V links is out-of-band to other carrier frequencies, which implies that mmWave V2V signals are only effective throughout the footprint of the road. And secondly, the roads are typically surrounded by buildings, foliage etc. which significantly bounds the mmWave V2V signals. Hence, the area component in ASE is interpreted as a road section in RSE. Plus, density in ASE is typically modelled in 2-D distribution of points. On the contrary, density in RSE is calculated over 1-D distribution of vehicles. As a result, the RSE is defined as

$$\text{RSE} = \frac{\lambda L_l N_L}{L_l N_L L_w} \log_2(1+\mathcal{T})\mathbb{P}_c(\mathcal{T}) \tag{6.20}$$

where N_L is the number of lanes and L_l the cross section of the lane length. The number of active transmitters are calculated in the numerator, whereas the total area of the road section is calculated in the denominator. Since N_L and L_l cancel each other, the final RSE becomes

$$\text{RSE} = \frac{\lambda}{L_w} \log_2(1+\mathcal{T})\mathbb{P}_c(\mathcal{T}). \tag{6.21}$$

Thus, it is shown that RSE is different from ASE due to the division by the lane width.

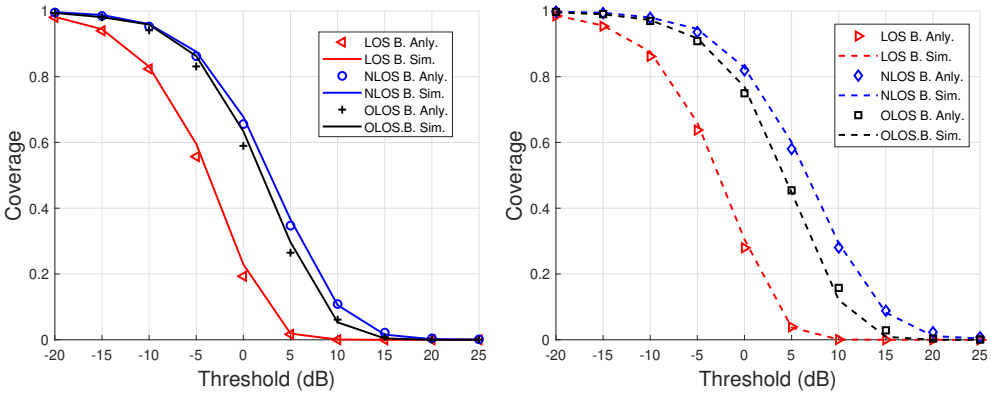

(a) $\lambda = 0.02$ (b) $\lambda = 0.03$

Figure 6.4: Coverage-threshold relationship for two vehicle densities, with $d = \lambda^{-1}$ and $\phi = 15°$, where markers and lines represent analytical and simulation results, respectively.

6.4 Numerical Analysis

A validation of the obtained analytical equations, specifically of the Laplace transforms (6.9)-(6.12), and (6.13), (6.15)-(6.18), for each path loss behaviour, is carried out by means of Monte Carlo simulations, with the number of iterations for each presented case exceeding 10^5. In addition, the parameters of the simulations and analytical models are presented in Table 6.4. In the presented figures, a good match is observed between these simulations and the analytical model.

Fig. 6.4 shows the coverage - SINR threshold performance for the three different path loss behaviours where the density increases from $\lambda = 0.02$ in Fig. 6.4a to 0.03 in Fig. 6.4b, accordingly the link distance decreases from $d = 50\,\text{m}$ to 33.3 m, which corresponds to a trend of $d = \lambda^{-1}$. It is observed that NLOS behaviour provides the best performance as the surrounding vehicles behave as strong isolators in addition to becoming interferers for the *typical* receiver. For similar reasons, OLOS behaviour outperforms LOS behaviour. Yet, this pattern is valid only when each vehicle is equipped with mmWave transceivers and follows in-lane routing. If the communications link needs to be established through an intermediate vehicle that is located between a transmitter and receiver pair other than the closest vehicles in the same lane, then achieving a successful link for NLOS behaviour is challenging. Whereas in this case OLOS behaviour still performs at acceptable coverage levels. Nevertheless, LOS behaviour is the most robust option for such scenarios, because the intermediate vehicles will likely be small, hence not act as blockages.

Conversely, Fig. 6.4 shows that increasing the density from $\lambda = 0.02$ to 0.03 improves the coverage performance for all behaviours. The main reason for this

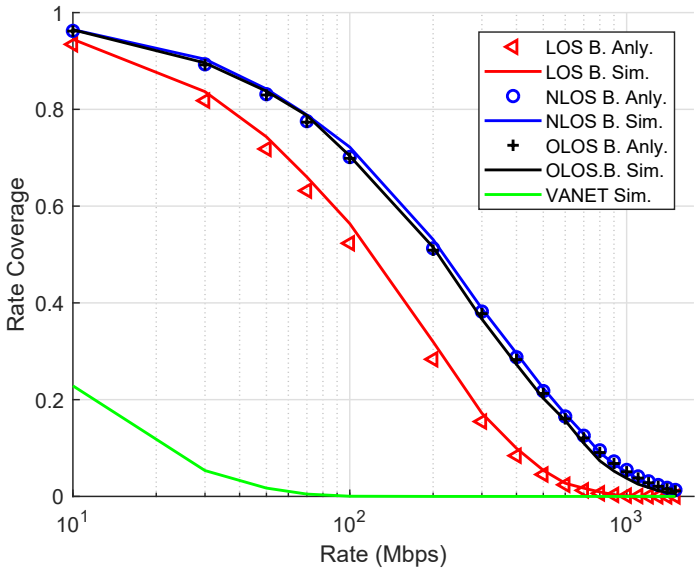

Figure 6.5: Rate coverage-rate relationship for various path loss behaviours, with $\lambda = 0.02$, $d = \lambda^{-1}$ and $\phi = 15°$, where markers and lines represent analytical and simulation results, respectively. The LOS and NLOS exponents for VANET are $\alpha_L^v = 1.77$ and $\alpha_N^v = 2.18$ [71], and the total bandwidth for VANET is 70 MHz.

trend is that the link distance is automatically reduced from $d = 50$ m to 33.3 m, which causes a gain in the signal component of the SINR that overcompensates the gain increase from the overall interference component of the SINR. Also note that the increase is larger for NLOS and OLOS behaviours compared to LOS behaviour. Intuitively, this arises from the fact that higher densities mean more vehicles and accordingly more blockages that act as isolators. Fig. 6.5 displays the relationship of the maximum data rate and its corresponding probability. In addition to three mmWave path loss behaviours, a VANET model is added, that implements a 5.9 GHz carrier frequency. Moreover, the VANET model applies omnidirectional communications and $G_m = g_s = 1$. Further, it is accepted that each vehicle is a transmitter and receiver simultaneously, and only large vehicles can cause an NLOS case. Hence, it is clearly shown that VANET can not achieve the data rate requirements for vision-sharing of CAVs. A comparison of the RSE for each path loss behaviour and different vehicle densities is provided in Fig. 6.6. NLOS behaviour slightly outperforms the OLOS behaviour, whereas they both significantly outperform the LOS behaviour. The reason for the NLOS behaviour being the best performer is that the beams of interferers are heavily blocked by the surrounding vehicles which improves the SINR, and accordingly the RSE. Besides this, a traditional trade-off between link reliability and RSE, typically observed in ad hoc networks, takes places in this model as well. In other words, the highest link reliability occurs at low SINR thresholds as shown in Fig. 6.4, whereas the highest RSE is achieved for

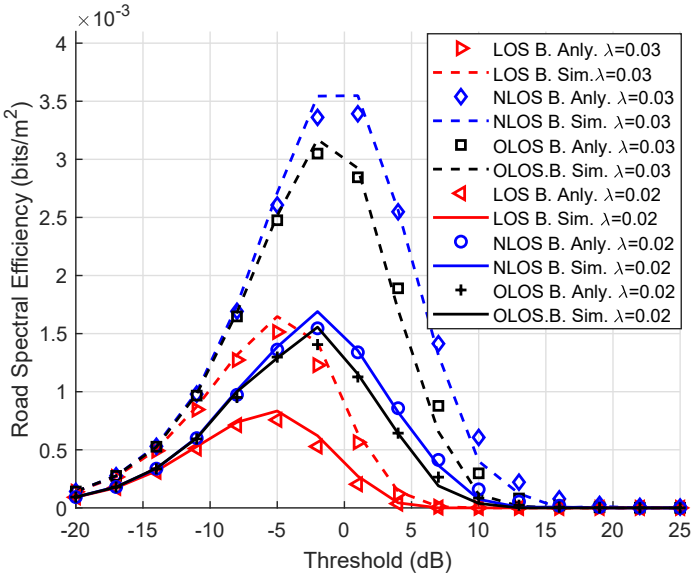

Figure 6.6: RSE-threshold relationship for two vehicle densities, with $d = \lambda^{-1}$ and $\phi = 15°$, where markers and lines represent analytical and simulation results, respectively.

high SINR thresholds as presented in Fig. 6.6. Additionally, the maximum RSE performance for LOS behaviour takes place at smaller SINR thresholds around -5 dB, whereas the RSE maxima of NLOS and OLOS behaviours occur for SINR thresholds around 0 dB. Naturally, the overall RSE performance is better for $\lambda = 0.03$ than for $\lambda = 0.02$, as a higher vehicular density generates a higher number of links.

Similar to the work of [8], which concludes that increasing the beamwidth above 30° does not significantly change the performance of mmWave V2I communications, the beamwidth can be seen as a key factor up to 30°, according to Fig. 6.7. Note that the analytical component of Figs. 6.4, 6.6, 6.7, and 6.8 are approximated functions, hence, they do neither include side-lobe gain nor NLOS interference. Moreover, since the main-lobe gains cancel each other's signal and interference components, the effect of the main lobe gain shows itself only in the noise component of the SINR. Accordingly, it can be stated that the improvement in coverage for decreasing beamwidth does not originate from an increased gain, as previously observed in (5.1) in Chapter 5. Rather, the narrowing beamwidth automatically converts main-to-main lobe interferers into side-to-side lobe gain interferers that are located in the adjacent lanes, as is depicted in Figs. 6.1b-d. Under an in-lane routing scheme, this phenomenon highlights that vehicle component manufacturers should not necessarily increase antenna gain, but should rather optimize its beamwidth.

Fig. 6.8 illustrates the relationship between the coverage and density of vehicles for all path loss behaviours, where different SINR thresholds are

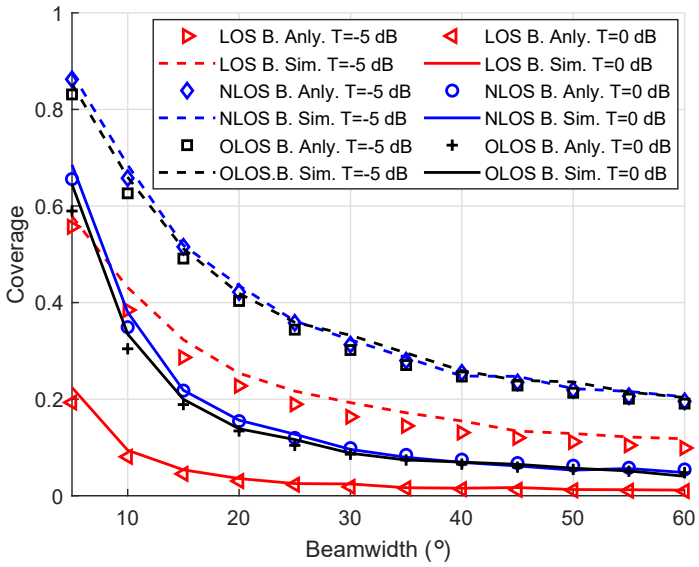

Figure 6.7: Coverage-beamwidth relationship for two SINR thresholds, with $d = \lambda^{-1}$ and $\lambda = 0.02$, where markers and lines represent analytical and simulation results, respectively.

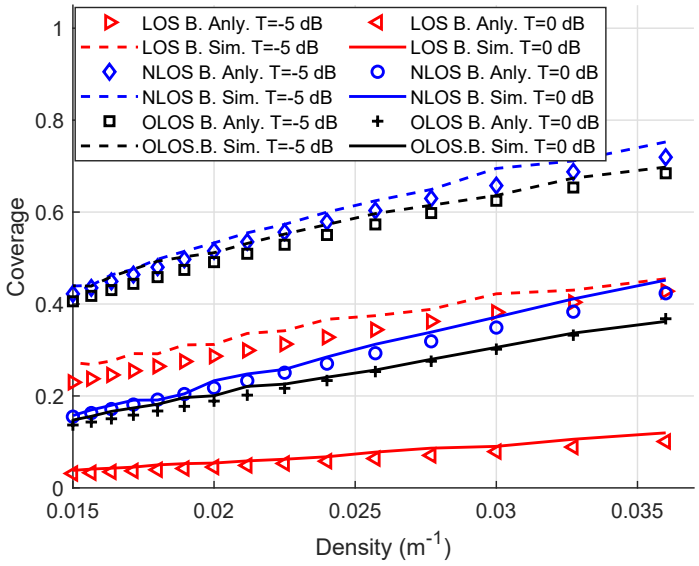

Figure 6.8: Coverage-density relationship for two SINR thresholds, with $d = \lambda^{-1}$ and $\phi = 15$, where markers and lines represent analytical and simulation results, respectively.

employed. It is observed that all three path loss behaviours display a *density-powered* coverage trend. In other words, increasing the vehicular density results in a shorter link distance, namely $d = \lambda^{-1}$. As it is shown in Fig. 6.4, a shorter link distance overcompensates the increase in overall interference. Note that the trend in coverage with respect to density for NLOS behaviour compared to LOS behaviour grows faster, because the increase of all surrounding vehicles of the *typical* receiver act as isolators for NLOS behaviour, whereas only large vehicles act as isolators for LOS behaviour.

Considering that only minor differences appear between simulation and analytical results, it is acceptable to state that side-to-side lobe gain and 1-NLOS, 2-NLOS, and 3-NLOS interferers are negligible. Firstly, the ratio of main-to-main and side-to-side lobe gains is typically large enough to make such simplification. Secondly, the high difference in path loss between 0-LOS and x-NLOS is another reason for this phenomenon. Thus, typically, the interferers that are located far away from the *typical* receiver tend to be NLOS interferers, hence their signal is strongly attenuated by both a large distance as well as a high path loss exponent. Consequently, it is found that NLOS and LOS behaviours provide the best and worst performance, respectively, when the vehicles are forced to communicate with the closest vehicle that is located in the same lane. On the contrary, NLOS and LOS behaviours provide the least and most reliable links, respectively, if vehicles are forced to communicate through blocking vehicles. Whereas, OLOS behaviour is always the secondary performer regardless of whether vehicles communicate through blocking vehicles or not.

6.5 Conclusions

In this chapter, the coverage and road spectral efficiency performance of multi-lane urban mmWave V2V networks are characterized. Underpinned by realistic mmWave channel models, a set of final analytical models was built, which are closed-form under some conditions. The mathematical derivations were expanded for three path loss behaviour scenarios, and the developed model proposes novel and realistic blockage models to represent the effect of obstructing vehicles. The following findings are observed; (i) implementing NLOS behaviour provides the best performance in coverage, but the least link reliability under an in-lane routing scheme; (ii) the impact of side-lobe gains and any NLOS interference is negligible; (iii) the magnitude of the main-lobe antenna gain does not have a major impact on the system performance; and (iv) mmWave V2V communications are density-insensitive if vehicles communicate with the nearest vehicle.

Chapter 7

Conclusions and Future Work

Over the preceding chapters, it has been shown that through the application of stochastic geometry and Monte Carlo simulations, a number of new ideas have been articulated and proven that provide a well-rounded contribution to knowledge in the estimation of the performance of mmWave for CAV applications. The wider impact of which is, that through the provision of better connectivity analysis, this work is able to contribute to technological advances for society through the faster adoption of CAVs. This in turn will allow for a greater number of people, and a higher degree of freedom for safer, greener, transport. This chapter is intended to summarise the main contributions and findings of the research and to complete the discussion, my thoughts and proposals for future work are also presented.

7.1 Conclusions and Contributions

Chapters 1 and 2 presented a background and a framework for the fundamentals of mmWave V2V communications. Specifically, Chapter 1 outlined the necessity to use mmWave carrier frequencies, which are significantly superior than existing V2X channels from a data rate perspective. This will thus satisfy the rising data rate requirements for the autonomy-enabling sensory equipment of future vehicles. Secondly, Chapter 2 deepens the explanation of challenges found in mmWave communications, namely, beam forming, blockage and path loss issues and their models. Finally, it concluded with a description of the fundamental characteristics of stochastic geometry, that have been utilized throughout the thesis.

In Chapter 3 an introductory analytical model was presented to reveal the deficiencies of the incumbent system models. It was found that the lossy nature of mmWave communications makes the interference that originates from roads other than the vehicle's own road, e.g. crossing and parallel roads, negligible. However, it also revealed that the interference from adjacent lanes to the

vehicle's own lane has a severe impact on the system performance. In addition, in this chapter it was proposed to use the Manhattan distance to model path loss in urban environments, rather than the Euclidean distance. This was specifically noted for cases where the signal encompasses the buildings at road junctions. Secondly, it modeled the transition of communications from LOS to NLOS fading, by simply using the inverse of the homogeneous PPP, i.e. λ^{-1}. Moreover, it was shown that the antenna locations on the vehicle significantly change the path loss behaviour due to the fact that blockages by the bodies of surrounding vehicles are a key factor on mmWave propagation. Additionally, the choice of routing scheme has a profound impact on the system performance. Through this introductory analytical model, it was revealed that the coverage is significantly dependent on the adjacent lanes, the antenna location, which is a key parameter of path loss behaviour, the antenna beamwidth, and the routing scheme. These inferences have directed the direction of research moving forward.

In Chapter 4 the connectivity probability was derived for single lane scenarios under different beamwidths, specifically 3°, 6°, 10°, 20°, and 45°, vehicular density and road curvature. This derivation was carried out by combining the concept of a geometric probability problem and a point process to present a realistic model. Considering that the success of CAVs' cooperative driving and platooning depends on the reliable data transmission from the foremost vehicle to the last vehicle of a platoon, achieving an appropriate SINR value at each hop whilst keeping beams aligned is critical. Given that the in-lane lateral displacements of vehicles, which were modelled by a truncated Gaussian distribution using measured data, the beam misalignment, and the required SINR level all depend on the critical transmission range between successive vehicles, the connectivity probability of mmWave vehicular communications is a two-fold problem. Hence, by using the tools of stochastic geometry and geometric probabilities, a trade-off between critical transmission range and beam alignment probability was revealed. Furthermore, it was shown that there is an optimum beamwidth that maximizes connectivity, which considers the beam alignment probability and the critical transmission range. As a key contribution of this chapter, it is shown that the narrowest antenna beam is the best performer in most scenarios, yet, wider beams perform better for high-density traffic and low-curvature roads. In addition, significant changes in connectivity performance occur for beams narrower than 10°. Moreover, it was found that the connectivity performance has a slight dependence on beamwidth for medium-density traffic and low-curvature roads. Furthermore, a method for the derivation of the expected value of the inverse of sum of random variables in a homogeneous PPP, which is the most analytically novel contribution of this chapter, has been developed. In other words, this method proposed a

generic solution for the inverse of the well-known Campbell's theorem.

In Chapter 5 two baseline routing schemes, namely the in-lane routing, and the closest-vehicle routing, have been analysed to understand the impact on the mean interference to the *typical* receiver. It has been shown that the homogeneous PPP used previously in the literature, allowed for the points to fall on top of each other, although the headway distance between vehicles requires a hardcore separation distance. As such, it was necessary to add a novel platooning-based headway distance into the homogeneous PPP. Beyond this, the single lane models employed in previous chapters were expanded to a two-lane model in order to gain a wider application area. In addition, the mean-interference of the closest vehicle and the in-lane routing schemes were derived and compared to reveal their advantages and disadvantages for different traffic scenarios. It was shown that the main-to-side lobe gain and side-to-side lobe gain had a minor impact on system performance and as such, the elimination of those terms in the model simplified the model significantly. As a key analytically novel contribution, Chapter 5 proposed an exceptionally tractable analytical derivation for the probability of the closest vehicle being located in an own lane. Furthermore, the cumulative distribution functions of various angles between receiver, transmitter and interferers, which were used to classify lobe alignment cases, have been derived. In addition, by classifying each vehicle based on its lane and the location of the corresponding receiver, vehicle types were ranked by the mean-interference they caused. Hence, it was found that the majority of the interference was caused by the interferers that were located in the lane of the *typical* receiver if its corresponding receiver was located in the same lane.

In Chapter 6 the coverage probability of a four-lane road layout was investigated under an in-lane routing scheme. The blockage probability caused by vehicles located in the adjacent lanes was also derived. Eventually, the coverage probabilities for different path loss behaviours, namely LOS, OLOS and NLOS, were derived. Hence, this chapter combines the blockage probabilities of vehicles, routing schemes and multi-lane scenario to simulate the complete behaviour of mmWave vehicular networks. Furthermore, the rate coverage and road spectral efficiency were introduced. As a most insightful finding of this chapter, it was found that the performance gain in coverage probability that arose from narrower beams, originates from the reduction in probability of being interfered with, rather than the increase in antenna gain. In addition, it was found that the performance of mmWave V2V communications is insensitive to the increase in vehicle density if the *typical* receiver is forced to communicate with the closest vehicle, which is the most valuable contribution of this chapter from practical point of view. Finally, the accuracy of a shifted PPP-like model was validated by comparison with a PTV Vissim simulation that took into

account the mobility of autonomous vehicles.

7.2 Future Research Directions

Given the potential socio-economic impact of increased CAV adoption by the public, it is clear that improvements in the enabling technologies, whether that be the sensors themselves, their fusion engines, or their connectivity provisions, will always be welcomed. As such, based upon my research, I also note that the potential for the following research ideas could build on the momentum presented herein.

The connectivity model in Chapter 4 could be extended to multi-lane traffic, and might include different routing behaviours as presented in Chapter 5. In addition, considering that the closest-vehicle routing scheme is more fragile and that its network topology dynamically changes, the rate of generating new links is expected to increase. Accordingly, this will increase the latency due to the excessive reciprocal beam alignment process and handshake protocols. For instance, the relationship between latency and the use of either in-lane routing or closest-vehicle routing would be of interest for CAV safety applications, where latency rather than data rate may be of higher importance. Furthermore, this could be extended to find the trade-off between data rate and latency, and its relation to CAV safety. Moreover, for autonomous vehicle perception, the closest vehicle is the one most likely to limit the vision/perception. Hence, routing over the closest vehicle should enable the greatest perception gain. Nevertheless, the in-lane vehicle routing, or furthest LOS routing, will likely provide the largest range extension for perception with poorer content quality due to the higher interference. Hence, characterizing the trade-off between the sustainability of the network topology and the benefits to autonomous driving capabilities is another research direction that could be explored.

The work presented in this thesis is built on the assumption that all vehicles are CAVs. Yet, it will take decades before the market penetration of CAVs reaches high percentages. Hence, the combination of CAVs and conventional vehicles will cause unusual characteristics in traffic in terms of headway distance, speed limits, lane allocations etc. Thus, the presented work could be enhanced by modelling both CAVs and conventional vehicles separately through the use of clustered and repulsive point processes, respectively. In such scenarios, CAVs will frequently have to pass their data through blockages caused by conventional vehicles, which will deteriorate the performance significantly considering the sensitivity of mmWave communications to blockage. Hence, this also requires the investigation into alternative routing schemes that prevent high path loss by by-passing conventional vehicles. Moreover, if the pod concept for one or two passengers in autonomous vehicles takes hold, the associated reduction of

vehicle dimensions will make blockages of adjacent lane vehicles less frequent. Hence, this will simultaneously improve and degrade the received SINR, and is thus an interesting topic to explore further.

In addition, for mathematical simplification this thesis is built on the assumption that each vehicle employs the same antenna beamwidth simultaneously for both their receiving and transmitting actions. However, one could also expect that each vehicle uses a different beamwidth for different scenarios, which yields a more complex beamwidth optimization problem. In other words, decreasing the beamwidth between selected pairs of transmitters and receivers increases the link performance in the interest of those pairs, which could undermine the overall network performance due to an increase in interference.

Moreover, the presented work has assumed that all vehicles establish single point-to-point communications. Yet, by means of placing several mmWave transceiver antennas on vehicles, it is possible to establish multi-points communications through which a vehicle can send multiple beams to multiple vehicles simultaneously.

With this, I finish the presentation of various promising research opportunities for the future in addition to the main contributions of my thesis.

Chapter 8

Appendices

A Proof of Lemma 1

The coverage probability can be expressed as,

$$\mathbb{P}_c(\mathcal{T}) = 1 - \mathbb{P}\left(h_o < \frac{\mathcal{T}}{P_t G_m G_m \mathcal{P}_L(d)}(I_\Phi + N_0)\right), \tag{A.1}$$

where I_Φ is the sum of all interferences. The small-scale fading of a *typical* link, h_0, is assumed to be Nakagami as in [26, 39], which is based upon a gamma random variable. To simplify the analysis, Alzer's lemma [57] is used

$$[1 - e^{-azm}]^m < \mathbb{P}(h_0 < z) \qquad a = (m!)^{-1/m}, \tag{A.2}$$

which provides a tight upper bound for the case of $h_0 \sim \Gamma(m, 1/m)$ where m is an integer. With the operation of the expected value, and the use of Alzer's lemma, the following can be obtained

$$\mathbb{P}_c(T) < \mathbb{E}_\Phi\left(1 - \left(1 - e^{\frac{-a\mathcal{T}m}{P_t G_m G_m \mathcal{P}_L(d)}(N_0 + I_\Phi)}\right)^m\right). \tag{A.3}$$

By means of binomial transformation and extending the expected value for each term

$$\begin{aligned}\mathbb{P}_c(\mathcal{T}) < \sum_{n=1}^{m}\binom{m}{n}(-1)^{n+1} & \underbrace{\mathbb{E}_0\left(e^{\frac{-an\mathcal{T}m}{P_t G_m G_m \mathcal{P}_L(d)} I_{L_0}}\right)}_{\mathcal{L}_0} \\ \cdot & \underbrace{\mathbb{E}_1\left(e^{\frac{-an\mathcal{T}m}{P_t G_m G_m \mathcal{P}_L(d)} I_{L_1}}\right)}_{\mathcal{L}_1} \cdot \underbrace{\mathbb{E}_2\left(e^{\frac{-an\mathcal{T}m}{P_t G_m G_m \mathcal{P}_L(d)} I_{L_2}}\right)}_{\mathcal{L}_2} \\ \cdot & \underbrace{\mathbb{E}_3\left(e^{\frac{-an\mathcal{T}m}{P_t G_m G_m \mathcal{P}_L(d)} I_{L_3}}\right)}_{\mathcal{L}_3} \cdot \underbrace{\left(e^{\frac{-an\mathcal{T}m}{P_t G_m G_m \mathcal{P}_L(d)} N_0}\right)}_{\text{Noise term}},\end{aligned} \tag{A.4}$$

which concludes the proof of *Lemma 1*, given that each expected value operator corresponds to a Laplace transform.

B Proof of Lemma 2

In order to provide a generic solution for all Laplace transforms in (A.4), each Laplace transform is expanded for different lanes of interferers and their gain alignments. Accordingly, the generic Laplace transform of gain alignment cases is shown in the expected value operators and braces, with $s = \frac{a\mathcal{T}}{G_m G_m \mathcal{P}_L(d)}$. By applying the moment generating function of gamma random variables for small-scale fading, h_i, results in

$$\begin{aligned}\mathbb{E}\left(\prod_{i\epsilon G_i}\prod_{\Phi}\mathbb{E}_{h_i}\left(e^{-snmh_i G_{i,t_r}\mathcal{P}_L(r)}\right)\right) = \\ \prod_{i\epsilon G_i}\mathbb{E}\left(\prod_{\Phi}\left(1+snG_{i,t_r}\mathcal{P}_L\left(r\right)\right)^{-m}\right)\end{aligned}. \tag{B.1}$$

By means of a probability generating functional, a generic Laplace transform that forms a basis for all other Laplace transforms can be written as

$$\mathcal{L}_{\text{generic}} = \prod_{i\epsilon G_i} e^{-\lambda\int_R\left(1-\left(1+snG_{i,t_r}\mathcal{P}_L(r)\right)^{-m}\right)dr}. \tag{B.2}$$

After some algebra (B.2) can be analytically integrated, resulting in a hypergeometric series which is presented as a Q function. Hence, the Laplace transform for the own lane is expressed as

$$\begin{aligned}\mathcal{L}_0^L = e^{-\lambda Q\left(G_m^2,\alpha_L,d,(\lambda\eta)^{-1}+d\right)}\cdot \\ e^{-\lambda Q\left(G_m^2,\alpha_N,(\lambda\eta)^{-1}+d,R_{\text{m}}\right)}.\end{aligned} \tag{B.3}$$

Similarly, for the adjacent and outer lanes, (B.2) is represented with $\mathcal{V}$, which concludes *Lemma 2*,

$$\begin{aligned}\mathcal{L}_i^L = e^{-\lambda\int_0^{\frac{iL_w}{\tan(\phi_h)}}\mathcal{V}\left(g_s^2,\alpha_L,iL_w\right)f_{L_i}(r)dr} \\ \cdot e^{-\lambda\int_{\frac{iL_w}{\tan(\phi_h)}}^{R_{\text{m}}}\mathcal{V}\left(G_m^2,\alpha_L,iL_w\right)f_{L_i}(r)dr} \\ \cdot e^{-\lambda\int_0^{\frac{iL_w}{\tan(\phi_h)}}\mathcal{V}\left(g_s^2,\alpha_N,iL_w\right)\left(1-f_{L_i}(r)\right)dr} \\ \cdot e^{-\lambda\int_{\frac{iL_w}{\tan(\phi_h)}}^{R_{\text{m}}}\mathcal{V}\left(G_m^2,\alpha_N,iL_w\right)\left(1-f_{L_i}(r)\right)dr},\end{aligned} \tag{B.4}$$

where the functions Q and $\mathcal{V}$ are

$$\begin{aligned}Q\left(G_{i,t_r},\alpha,r_{\min},r_{\max}\right) = \\ r\left(1-{}_2F_1\left(\frac{-1}{\alpha},m;\frac{\alpha-1}{\alpha};-snG_{i,t_r}Ar^{-\alpha}\right)\right)\Big|_{r_{\min}}^{r_{\max}},\end{aligned} \tag{B.5}$$

$$\mathcal{V}\left(G_{i,t_r},\alpha,L_x\right) = 1-\left(1+nsG_{i,t_r}A\left(r^2+L_x^2\right)^{-\alpha/2}\right)^{-m}. \tag{B.6}$$

C Proof of Lemma 3

The following steps are carried out in order to calculate the impact of interferences of vehicles that are located in the lane of the *typical* receiver. Since the path loss characterization differs for each vehicle in the neighbourhood of the *typical* receiver, it is necessary to take the interference effects of each vehicle into account individually. The interferences of the nearest 1-st, 2-nd, and 3-rd vehicles to the *typical* receiver, excluding the *typical* transmitter, are modelled as

$$\mathcal{L}_0^O = \prod_{i=1}^{3} \mathbb{E}_{\mathrm{r}} \left(\left(1 + snG_m^2 A_i^t r^{-\alpha_i^t} \right)^{-m} \right). \tag{C.1}$$

Since the vehicles are distributed with mono-dimensional PPP, it is assumed that the vehicles are truncated uniformly distributed. Thus, the following equation represents the application of the expected value of a uniformly distributed random variable truncated at $[2(i-1)\lambda^{-1} + d \quad 2i\lambda^{-1} + d]$, where i is defined for $\{1, 2, 3\}$ for the nearest 1-st, 2-nd, and 3-rd vehicles, excluding the *typical* transmitter, respectively as

$$\mathcal{L}_0^O = \prod_{i=1}^{3} \frac{1}{2\lambda^{-1}} \int_{2(i-1)\lambda^{-1}+d}^{2i\lambda^{-1}+d} \left(1 + snG_m^2 A_i^t r^{-\alpha_i^t} \right)^{-m} dr. \tag{C.2}$$

Integration of (C.2) with some algebra will form (6.15) which concludes *Lemma 3*. Similarly, $\mathcal{L}_{1-2}^O$ is given as

$$\begin{aligned} \mathcal{L}_i^O = {} & e^{-\lambda \int_0^{\frac{iL_w}{\tan(\phi_h)}} \mathcal{V}\left(g_s^2, \alpha_0, iL_w\right) f_{L_i}(r) dr} \\ & \cdot e^{-\lambda \int_{\frac{iL_w}{\tan(\phi_h)}}^{R_{\mathrm{m}}} \mathcal{V}\left(G_m^2, \alpha_0, iL_w\right) f_{L_i}(r) dr} \\ & \cdot e^{-\lambda \int_0^{\frac{iL_w}{\tan(\phi_h)}} \mathcal{V}\left(g_s^2, \alpha_1, iL_w\right) \left(1 - f_{L_i}(r)\right) dr} \\ & \cdot e^{-\lambda \int_{\frac{iL_w}{\tan(\phi_h)}}^{R_{\mathrm{m}}} \mathcal{V}\left(G_m^2, \alpha_1, iL_w\right) \left(1 - f_{L_i}(r)\right) dr}. \end{aligned} \tag{C.3}$$

Due to fact that $\mathcal{L}_3^O$ is subject to different types of interferences from adjacent lanes, such as 1-NLOS and 2-NLOS, it is formulated as

$$\begin{aligned}\mathcal{L}_3^O = & e^{-\lambda \int_0^{\frac{3L_w}{\tan(\phi_h)}} \mathcal{V}\left(g_s^2,\alpha_0,3L_w\right) f_{L_3}(r) dr} \\ & \cdot e^{-\lambda \int_{\frac{3L_w}{\tan(\phi_h)}}^{R_{\mathrm{m}}} \mathcal{V}\left(G_m^2,\alpha_0,3L_w\right) f_{L_3}(r) dr} \\ & \cdot e^{-\lambda \int_0^{\frac{3L_w}{\tan(\phi_h)}} \mathcal{V}\left(g_s^2,\alpha_1,3L_w\right) \sqrt{f_{L_3}(r)} dr} \\ & \cdot e^{-\lambda \int_{\frac{3L_w}{\tan(\phi_h)}}^{R_{\mathrm{m}}} \mathcal{V}\left(G_m^2,\alpha_1,3L_w\right) \sqrt{f_{L_3}(r)} dr} \\ & \cdot e^{-\lambda \int_0^{\frac{3L_w}{\tan(\phi_h)}} \mathcal{V}\left(g_s^2,\alpha_2,3L_w\right) \left(1-f_{L_3}(r)\right) dr} \\ & \cdot e^{-\lambda \int_{\frac{3L_w}{\tan(\phi_h)}}^{R_{\mathrm{m}}} \mathcal{V}\left(G_m^2,\alpha_2,3L_w\right) \left(1-f_{L_3}(r)\right) dr} .\end{aligned} \tag{C.4}$$

Bibliography

[1] N. Lu, N. Cheng, N. Zhang, X. Shen, and J. W. Mark, "Connected vehicles: Solutions and challenges," *IEEE Internet of Things Journal*, vol. 1, pp. 289–299, Aug. 2014.

[2] Zenzic, "UK connected and automated mobility roadmap to 2030." [Online]. Available: `https://zenzic.io/content/uploads/2020/10/Zenzic_Roadmap_Report_v3.pdf`, Oct. 2020.

[3] J. B. Kenney, "Dedicated Short-Range Communications (DSRC) Standards in the United States," *Proceedings of the IEEE*, vol. 99, pp. 1162–1182, July 2011.

[4] S. Sun, J. Hu, Y. Peng, X. Pan, L. Zhao, and J. Fang, "Support for vehicle-to-everything services based on LTE," *IEEE Wireless Communications*, vol. 23, pp. 4–8, June 2016.

[5] J. Choi, V. Va, N. Gonzalez-Prelcic, R. Daniels, C. R. Bhat, and R. W. Heath, "Millimeter-wave vehicular communication to support massive automotive sensing," *IEEE Communications Magazine*, vol. 54, pp. 160–167, Dec. 2016.

[6] V. K. Kukkala, J. Tunnell, S. Pasricha, and T. Bradley, "Advanced driver-assistance systems: A path toward autonomous vehicles," *IEEE Consumer Electronics Magazine*, vol. 7, no. 5, pp. 18–25, 2018.

[7] G. Araniti, C. Campolo, M. Condoluci, A. Iera, and A. Molinaro, "LTE for vehicular networking: a survey," *IEEE Communications Magazine*, vol. 51, no. 5, pp. 148–157, 2013.

[8] A. Tassi, M. Egan, R. J. Piechocki, and A. Nix, "Modeling and design of millimeter-wave networks for highway vehicular communication," *IEEE Transactions on Vehicular Technology*, vol. 66, pp. 10676–10691, Dec. 2017.

[9] J. Harding, G. Powell, R. Yoon, J. Fikentscher, C. Doyle, D. Sade, M. Lukuc, J. Simons, and J. Wang, "Vehicle-to-vehicle communications:

Readiness of V2V technology for application," Tech. Rep. DOT HS 812 014, National Highway Traffic Safety Administration, Aug. 2014.

[10] T. S. Rappaport, J. N. Murdock, and F. Gutierrez, "State of the art in 60-GHz integrated circuits and systems for wireless communications," *Proceedings of the IEEE*, vol. 99, no. 8, pp. 1390–1436, 2011.

[11] G. R. MacCartney, Junhong Zhang, Shuai Nie, and T. S. Rappaport, "Path loss models for 5G millimeter wave propagation channels in urban microcells," in *2013 IEEE Global Communications Conference (GLOBECOM)*, pp. 3948–3953, 2013.

[12] 5G Infrastructure Public Private Partnership, "5G-PPP white paper on automotive vertical sector." [Online]. Available: `https://5g-ppp.eu/wp-content/uploads/2014/02/5G-PPP-White-Paper-on-Automotive-Vertical-Sectors.pdf`, Oct. 2015.

[13] T. S. Rappaport, S. Sun, R. Mayzus, H. Zhao, Y. Azar, K. Wang, G. N. Wong, J. K. Schulz, M. Samimi, and F. Gutierrez, "Millimeter wave mobile communications for 5G cellular: It will work!," *IEEE Access*, vol. 1, pp. 335–349, 2013.

[14] European Commission, "C-ITS Platform." [Online]. Available: `https://ec.europa.eu/transport/sites/transport/files/themes/its/doc/c-its-platform-final-report-january-2016.pdf`, Jan. 2016.

[15] "Report and order and further notice of proposed rulemaking," Tech. Rep. FCC 16-89, Federal Communications Commission , Washington, D.C, USA, July 2016.

[16] "Decision to make the wireless telegraphy (exemption and amendment)(amendment) (no.2) regulations 2018," Tech. Rep. No. 1140, Office Communications, London, UK, Nov. 2018.

[17] T. Rappaport, *Wireless Communications: Principles and Practice*. USA: Prentice Hall PTR, 2nd ed., 2001.

[18] M. Afshang, H. S. Dhillon, and P. H. J. Chong, "Modeling and performance analysis of clustered device-to-device networks," *IEEE Transactions on Wireless Communications*, vol. 15, pp. 4957–4972, July 2016.

[19] T. Abbas, J. Nuckelt, T. Kürner, T. Zemen, C. F. Mecklenbräuker, and F. Tufvesson, "Simulation and measurement-based vehicle-to-vehicle channel characterization: Accuracy and constraint analysis," *IEEE Transactions on Antennas and Propagation*, vol. 63, no. 7, pp. 3208–3218, 2015.

[20] M. Mezzavilla, M. Zhang, M. Polese, R. Ford, S. Dutta, S. Rangan, and M. Zorzi, "End-to-end simulation of 5G mmwave networks," *IEEE Communications Surveys Tutorials*, vol. 20, pp. 2237–2263, Apr. 2018.

[21] M. Gonzalez-Martín, M. Sepulcre, R. Molina-Masegosa, and J. Gozalvez, "Analytical models of the performance of C-V2X mode 4 vehicular communications," *IEEE Transactions on Vehicular Technology*, vol. 68, no. 2, pp. 1155–1166, 2019.

[22] A. D. Wyner, "Shannon-theoretic approach to a gaussian cellular multiple-access channel," *IEEE Transactions on Information Theory*, vol. 40, no. 6, pp. 1713–1727, 1994.

[23] M. D. Renzo, "Stochastic geometry modeling and analysis of multi-tier millimeter wave cellular networks," *IEEE Transactions on Wireless Communications*, vol. 14, pp. 5038–5057, Sept. 2015.

[24] J. Xu, J. Zhang, and J. G. Andrews, "On the accuracy of the Wyner model in cellular networks," *IEEE Transactions on Wireless Communications*, vol. 10, no. 9, pp. 3098–3109, 2011.

[25] F. Baccelli and B. Błaszczyszyn, "Stochastic geometry and wireless networks: Volume I theory," *Foundations and Trends in Networking*, vol. 3, no. 3–4, pp. 249–449, 2010.

[26] M. Ozpolat, E. Kampert, P. A. Jennings, and M. D. Higgins, "A grid-based coverage analysis of urban mmwave vehicular ad hoc networks," *IEEE Communications Letters*, vol. 22, pp. 1692–1695, Aug. 2018.

[27] M. Ozpolat, O. Alluhaibi, E. Kampert, and M. D. Higgins, "Connectivity analysis for mmwave V2V networks: Exploring critical distance and beam misalignment," in *IEEE Globecom*, (Hawaii, USA), Dec. 2019, In press.

[28] T. D. Novlan, H. S. Dhillon, and J. G. Andrews, "Analytical modeling of uplink cellular networks," *IEEE Transactions on Wireless Communications*, vol. 12, no. 6, pp. 2669–2679, 2013.

[29] S. Mukherjee, "Distribution of downlink sinr in heterogeneous cellular networks," *IEEE Journal on Selected Areas in Communications*, vol. 30, no. 3, pp. 575–585, 2012.

[30] S. Singh and J. G. Andrews, "Joint resource partitioning and offloading in heterogeneous cellular networks," *IEEE Transactions on Wireless Communications*, vol. 13, no. 2, pp. 888–901, 2014.

[31] S. Singh, H. S. Dhillon, and J. G. Andrews, "Offloading in heterogeneous networks: Modeling, analysis, and design insights," *IEEE Transactions on Wireless Communications*, vol. 12, no. 5, pp. 2484–2497, 2013.

[32] Y. S. Soh, T. Q. S. Quek, M. Kountouris, and H. Shin, "Energy efficient heterogeneous cellular networks," *IEEE Journal on Selected Areas in Communications*, vol. 31, no. 5, pp. 840–850, 2013.

[33] H.-S. Jo, Y. J. Sang, P. Xia, and J. G. Andrews, "Heterogeneous cellular networks with flexible cell association: A comprehensive downlink sinr analysis," *IEEE Transactions on Wireless Communications*, vol. 11, no. 10, pp. 3484–3495, 2012.

[34] X. Lin, J. G. Andrews, and A. Ghosh, "Spectrum sharing for device-to-device communication in cellular networks," *IEEE Transactions on Wireless Communications*, vol. 13, no. 12, pp. 6727–6740, 2014.

[35] A. H. Sakr and E. Hossain, "Cognitive and energy harvesting-based D2D communication in cellular networks: Stochastic geometry modeling and analysis," *IEEE Transactions on Communications*, vol. 63, no. 5, pp. 1867–1880, 2015.

[36] N. Lee, X. Lin, J. G. Andrews, and R. W. Heath, "Power control for D2D underlaid cellular networks: Modeling, algorithms, and analysis," *IEEE Journal on Selected Areas in Communications*, vol. 33, no. 1, pp. 1–13, 2015.

[37] T. Bai and R. W. Heath, "Coverage and rate analysis for millimeter-wave cellular networks," *IEEE Transactions on Wireless Communications*, vol. 14, pp. 1100–1114, Feb. 2015.

[38] X. Yu, J. Zhang, and K. B. Letaief, "Coverage analysis for dense millimeter wave cellular networks: The impact of array size," in *IEEE Wireless Communications and Networking Conference*, pp. 1–6, Apr. 2016.

[39] A. Thornburg, T. Bai, and R. W. Heath, "Performance analysis of outdoor mmwave adhoc networks," *IEEE Transactions on Signal Processing*, vol. 64, pp. 4065–4079, Aug. 2016.

[40] W. Yi, Y. Liu, and A. Nallanathan, "Modeling and analysis of D2D millimeter-wave networks with Poisson cluster processes," *IEEE Transactions on Communications*, vol. 65, pp. 5574–5588, Dec. 2017.

[41] F. Baccelli and X. Zhang, "A correlated shadowing model for urban wireless networks," in *IEEE Conference on Computer Communications (INFOCOM)*, pp. 801–809, 2015.

[42] E. Steinmetz, M. Wildemeersch, T. Q. S. Quek, and H. Wymeersch, "A stochastic geometry model for vehicular communication near intersections," in *IEEE Globecom Workshops (GC Wkshps)*, (San Diego, CA), pp. 1–6, 2015.

[43] M. J. Farooq, H. Elsawy, and M. Alouini, "A stochastic geometry model for multi-hop highway vehicular communication," *IEEE Transactions on Wireless Communications*, vol. 15, pp. 2276–2291, Mar. 2016.

[44] T. S. Rappaport, G. R. MacCartney, M. K. Samimi, and S. Sun, "Wideband millimeter-wave propagation measurements and channel models for future wireless communication system design," *IEEE Transactions on Communications*, vol. 63, pp. 3029–3056, Sept. 2015.

[45] T. S. Rappaport, F. Gutierrez, E. Ben-Dor, J. N. Murdock, Y. Qiao, and J. I. Tamir, "Broadband millimeter-wave propagation measurements and models using adaptive-beam antennas for outdoor urban cellular communications," *IEEE Transactions on Antennas and Propagation*, vol. 61, pp. 1850–1859, Apr. 2013.

[46] "Spatial channel model for multiple input multiple output (MIMO) simulations," Tech. Rep. 25.996, 3rd Generation Partnership Project (3GPP), Sept. 2003.

[47] P. Kyosti, J. Meinilä, L. Hentilä, X. Zhao, T. Jämsä, C. Schneider, M. Narandzić, M. Milojević, A. Hong, J. Ylitalo, V. Holappa, M. Alatossava, R. Bultitude, Y. Jong, and T. Rautiainen, "WINNER II channel models," Tech. Rep. IST-4-027756 WINNER II D1.1.2 V1.2, Sept. 2007.

[48] S. Sun, T. S. Rappaport, S. Rangan, T. A. Thomas, A. Ghosh, I. Z. Kovacs, I. Rodriguez, O. Koymen, A. Partyka, and J. Jarvelainen, "Propagation path loss models for 5G urban micro- and macro-cellular scenarios," in *2016 IEEE 83rd Vehicular Technology Conference (VTC Spring)*, pp. 1–6, 2016.

[49] A. J. Goldsmith, *Wireless Communications*. Cambridge, UK: Cambridge University Press, 2005.

[50] L. Bernadó, T. Zemen, F. Tufvesson, A. F. Molisch, and C. F. Mecklenbräuker, "Delay and doppler spreads of nonstationary vehicular channels for safety-relevant scenarios," *IEEE Transactions on Vehicular Technology*, vol. 63, pp. 82–93, Jan. 2014.

[51] Z. Pi and F. Khan, "An introduction to millimeter-wave mobile broadband systems," *IEEE Communications Magazine*, vol. 49, pp. 101–107, June 2011.

[52] V. Va and R. W. Heath, "Basic relationship between channel coherence time and beamwidth in vehicular channels," in *IEEE 82nd Vehicular Technology Conference. (VTC2015-Fall)*, pp. 1–5, Sept. 2015.

[53] T. Bai, R. Vaze, and R. W. Heath, "Analysis of blockage effects on urban cellular networks," *IEEE Transactions on Wireless Communications*, vol. 13, no. 9, pp. 5070–5083, 2014.

[54] M. Di Renzo and P. Guan, "Stochastic geometry modeling of coverage and rate of cellular networks using the Gil-Pelaez inversion theorem," *IEEE Communications Letters*, vol. 18, no. 9, pp. 1575–1578, 2014.

[55] K. A. Hamdi, "A useful lemma for capacity analysis of fading interference channels," *IEEE Transactions on Communications*, vol. 58, no. 2, pp. 411–416, 2010.

[56] A. K. Gupta, H. S. Dhillon, S. Vishwanath, and J. G. Andrews, "Downlink multi-antenna heterogeneous cellular network with load balancing," *IEEE Transactions on Communications*, vol. 62, no. 11, pp. 4052–4067, 2014.

[57] H. Alzer, "On some inequalities for the incomplete Gamma function," *Mathematics of Computation*, vol. 66, no. 218, pp. 771–778, 1997.

[58] S. Weber, J. G. Andrews, and N. Jindal, "The effect of fading, channel inversion, and threshold scheduling on ad hoc networks," *IEEE Transactions on Information Theory*, vol. 53, no. 11, pp. 4127–4149, 2007.

[59] J. Venkataraman, M. Haenggi, and O. Collins, "Shot noise models for outage and throughput analyses in wireless ad hoc networks," in *MILCOM 2006 - 2006 IEEE Military Communications conference*, pp. 1–7, 2006.

[60] H. ElSawy, E. Hossain, and M. Haenggi, "Stochastic geometry for modeling, analysis, and design of multi-tier and cognitive cellular wireless networks: A survey," *IEEE Communications Surveys Tutorials*, vol. 15, no. 3, pp. 996–1019, 2013.

[61] F. Baccelli, B. Blaszczyszyn, and P. Muhlethaler, "Stochastic analysis of spatial and opportunistic Aloha," *IEEE Journal on Selected Areas in Communications*, vol. 27, no. 7, pp. 1105–1119, 2009.

[62] J. Wildman, P. H. J. Nardelli, M. Latva-aho, and S. Weber, "On the joint impact of beamwidth and orientation error on throughput in directional wireless Poisson networks," *IEEE Transactions on Wireless Communications*, vol. 13, pp. 7072–7085, Dec. 2014.

[63] M. Haenggi, *Stochastic Geometry for Wireless Networks*. Cambridge University Press, 2012.

[64] M. Haenggi and R. K. Ganti, "Interference in large wireless networks," *Foundations and Trends in Networking*, vol. 3, no. 2, pp. 127–248, 2009.

[65] M. Haenggi, J. G. Andrews, F. Baccelli, O. Dousse, and M. Franceschetti, "Stochastic geometry and random graphs for the analysis and design of wireless networks," *IEEE Journal on Selected Areas in Communications*, vol. 27, no. 7, pp. 1029–1046, 2009.

[66] H. J. Thomas, R. S. Cole, and G. L. Siqueira, "An experimental study of the propagation of 55 GHz millimeter waves in an urban mobile radio environment," *IEEE Transactions on Vehicular Technology*, vol. 43, pp. 140–146, Feb. 1994.

[67] Y. Wang, K. Venugopal, A. F. Molisch, and R. W. Heath, "Mmwave vehicle-to-infrastructure communication: Analysis of urban microcellular networks," *IEEE Transactions on Vehicular Technology*, vol. 67, pp. 7086–7100, Aug. 2018.

[68] R. Schneider, D. Didascalou, and W. Wiesbeck, "Impact of road surfaces on millimeter-wave propagation," *IEEE Transactions on Vehicular Technology*, vol. 49, pp. 1314–1320, July 2000.

[69] A. Yamamoto, K. Ogawa, T. Horimatsu, A. Kato, and M. Fujise, "Path-loss prediction models for intervehicle communication at 60 GHz," *IEEE Transactions on Vehicular Technology*, vol. 57, pp. 65–78, Jan. 2008.

[70] A. Karttunen, A. F. Molisch, S. Hur, J. Park, and C. J. Zhang, "Spatially consistent street-by-street path loss model for 28-GHz channels in micro cell urban environments," *IEEE Transactions on Wireless Communications*, vol. 16, pp. 7538–7550, Nov. 2017.

[71] H. Fernández, L. Rubio, V. M. Rodrigo-Peñarrocha, and J. Reig, "Path loss characterization for vehicular communications at 700 MHz and 5.9 GHz under los and nlos conditions," *IEEE Antennas and Wireless Propagation Letters*, vol. 13, pp. 931–934, 2014.

[72] S. Kim, B. Qin, Z. J. Chong, X. Shen, W. Liu, M. H. Ang, E. Frazzoli, and D. Rus, "Multivehicle cooperative driving using cooperative perception:

Design and experimental validation," *IEEE Transactions on Intelligent Transportation Systems*, vol. 16, pp. 663–680, Apr. 2015.

[73] R. Woodman, K. Lu, M. D. Higgins, S. Brewerton, P. Jennings, and S. Birrell, "A human factors approach to defining requirements for low-speed autonomous vehicles to enable intelligent platooning," in *2019 IEEE Intelligent Vehicles Symposium (IV)*, (Paris), June 2019.

[74] S. Kwon, Y. Kim, and N. B. Shroff, "Analysis of connectivity and capacity in 1-D vehicle-to-vehicle networks," *IEEE Transactions on Wireless Communications*, vol. 15, pp. 8182–8194, Dec. 2016.

[75] E. Kampert, P. A. Jennings, and M. D. Higgins, "Investigating the V2V millimeter-wave channel near a vehicular headlight in an engine bay," *IEEE Communications Letters*, vol. 22, pp. 1506–1509, July 2018.

[76] N. Wisitpongphan, F. Bai, P. Mudalige, V. Sadekar, and O. Tonguz, "Routing in sparse vehicular ad hoc wireless networks," *IEEE Journal on Selected Areas in Communications*, vol. 25, pp. 1538–1556, Oct. 2007.

[77] P. Santi and D. M. Blough, "The critical transmitting range for connectivity in sparse wireless ad hoc networks," *IEEE Transactions on Mobile Computing*, vol. 2, pp. 25–39, Jan. 2003.

[78] M. Khabazian and M. K. M. Ali, "A performance modeling of connectivity in vehicular ad hoc networks," *IEEE Transactions on Vehicular Technology*, vol. 57, pp. 2440–2450, July 2008.

[79] "Vehicle-to-vehicle connectivity analysis for vehicular ad-hoc networks," *Ad Hoc Networks*, vol. 58, pp. 25–35, 2017. Hybrid Wireless Ad Hoc Networks.

[80] M. A. Hoque, X. Hong, and B. Dixon, "Efficient multi-hop connectivity analysis in urban vehicular networks," *Vehicular Communications*, vol. 1, no. 2, pp. 78–90, 2014.

[81] A. Jia, S. Jiang, Y. Lv, X. Zhang, T. Chang, I. Rashdan, P. Unterhuber, and W. Wang, "Connectivity analysis of V2V channel at intersections," in *2021 15th European Conference on Antennas and Propagation (EuCAP)*, pp. 1–4, 2021.

[82] C. Shao, S. Leng, Y. Zhang, A. Vinel, and M. Jonsson, "Performance analysis of connectivity probability and connectivity-aware mac protocol design for platoon-based vanets," *IEEE Transactions on Vehicular Technology*, vol. 64, no. 12, pp. 5596–5609, 2015.

[83] B. Pan and H. Wu, "Performance analysis of connectivity considering user behavior in V2V and V2I communication systems," in *2017 IEEE 86th Vehicular Technology Conference (VTC-Fall)*, pp. 1–5, 2017.

[84] B. L. Nguyen, D. T. Ngo, N. H. Tran, M. N. Dao, and H. L. Vu, "Dynamic V2I/V2V cooperative scheme for connectivity and throughput enhancement," *IEEE Transactions on Intelligent Transportation Systems*, pp. 1–11, 2020.

[85] H. Gao, C. Liu, Y. Li, and X. Yang, "V2VR: Reliable hybrid-network-oriented V2V data transmission and routing considering rsus and connectivity probability," *IEEE Transactions on Intelligent Transportation Systems*, pp. 1–14, 2020.

[86] F. Li, W. Chen, and Y. Shui, "Study on connectivity probability of vanets under adverse weather conditions at 5.9 GHz," *IEEE Access*, vol. 8, pp. 547–555, 2020.

[87] X. Lin and J. G. Andrews, "Connectivity of millimeter wave networks with multi-hop relaying," *IEEE Transactions on Wireless Communications*, vol. 4, pp. 209–212, Apr. 2015.

[88] K. Eshteiwi, G. Kaddoum, K. Ben Fredj, E. Soujeri, and F. Gagnon, "Performance analysis of full-duplex vehicle relay-based selection in dense multi-lane highways," *IEEE Access*, vol. 7, pp. 61581–61595, 2019.

[89] R. Singh, D. Saluja, and S. Kumar, "Graphical approach for V2V connectivity enhancement in clustering-based vanet," *IEEE Wireless Communications Letters*, pp. 1–1, 2021.

[90] S. Sun, T. S. Rappaport, T. A. Thomas, A. Ghosh, H. C. Nguyen, I. Z. Kovács, I. Rodriguez, O. Koymen, and A. Partyka, "Investigation of prediction accuracy, sensitivity, and parameter stability of large-scale propagation path loss models for 5G wireless communications," *IEEE Transactions on Vehicular Technology*, vol. 65, pp. 2843–2860, May 2016.

[91] E. Ben-Dor, T. S. Rappaport, Y. Qiao, and S. J. Lauffenburger, "Millimeter-wave 60 GHz outdoor and vehicle AOA propagation measurements using a broadband channel sounder," in *IEEE Global Communications Conference (GLOBECOM)*, pp. 1–6, Dec. 2011.

[92] L. Breiman, "The poisson tendency in traffic distribution," *Annals of Mathematical Statistics*, vol. 34, pp. 308–311, Mar. 1963.

[93] S. M. Ross, *Stochastic processes*. Hoboken, NJ, USA: Wiley, 2 ed., 1996.

[94] A. W. Ahmed, S. F. Said, X. Lu, and H. Carlsson, "Pavement performance follow-up and evaluation of polymer-modified test sections," *International Journal of Pavement Engineering*, pp. 1–14, 2018.

[95] E. Woodgate and M. Winnet, "Lateral distribution of motorway traffic," Tech. Rep. TRL Report 356, Transport Research Laboratory, Wokingham, UK, 1998.

[96] W. L. Stevens, "Solution to a geometrical problem in probability," *Annals of Human Genetics*, vol. 9, no. 4, pp. 315–320, 1939.

[97] H. Solomon, *Geometric Probability*. Philadelphia, PA, USA: SIAM: Cambridge University Press, 1978.

[98] Z. L. Fazliu, F. Malandrino, C. F. Chiasserini, and A. Nordio, "Mmwave beam management in urban vehicular networks," *IEEE Systems Journal*, pp. 1–12, 2020.

[99] W. Yi, Y. Liu, Y. Deng, A. Nallanathan, and R. W. Heath, "Modeling and analysis of mmwave V2X networks with vehicular platoon systems," *IEEE Journal on Selected Areas in Communications*, vol. 37, no. 12, pp. 2851–2866, 2019.

[100] I. Rasheed, F. Hu, Y. Hong, and B. Balasubramanian, "Intelligent vehicle network routing with adaptive 3D beam alignment for mmwave 5G-based V2X communications," *IEEE Transactions on Intelligent Transportation Systems*, pp. 1–13, 2020.

[101] Z. Li, L. Xiang, X. Ge, G. Mao, and H. Chao, "Latency and reliability of mmwave multi-hop V2V communications under relay selections," *IEEE Transactions on Vehicular Technology*, pp. 1–1, 2020.

[102] Y. Wu, L. Yan, and X. Fang, "A low-latency content dissemination scheme for mmwave vehicular networks," *IEEE Internet of Things Journal*, vol. 6, no. 5, pp. 7921–7933, 2019.

[103] D. Moltchanov, R. Kovalchukov, M. Gerasimenko, S. Andreev, Y. Koucheryavy, and M. Gerla, "Socially inspired relaying and proactive mode selection in mmwave vehicular communications," *IEEE Internet of Things Journal*, vol. 6, no. 3, pp. 5172–5183, 2019.

[104] C. Perfecto, J. Del Ser, and M. Bennis, "Millimeter-wave V2V communications: Distributed association and beam alignment," *IEEE Journal on Selected Areas in Communications*, vol. 35, no. 9, pp. 2148–2162, 2017.

[105] E. van Nunen, F. Esposto, A. K. Saberi, and J. Paardekooper, "Evaluation of safety indicators for truck platooning," in *2017 IEEE Intelligent Vehicles Symposium (IV)*, pp. 1013–1018, 2017.

[106] S. N. Chiu, D. Stoyan, W. S. Kendall, and J. Mecke, *Stochastic Geometry and Its Applications*. Chichester, West Sussex, UK: Wiley, 1995.

[107] S. M. Ross, *Introduction to Probability Models, Ninth Edition*. USA: Academic Press, Inc., 2006.

[108] A. Gelman and D. Nolan., *Teaching Statistics: A Bag of Tricks*. Oxford University Press, 2017.

[109] M. Treiber and A. Kesting, "An open-source microscopic traffic simulator," *IEEE Intelligent Transportation Systems Magazine*, vol. 2, no. 3, pp. 6–13, 2010.

[110] J. Hasch, E. Topak, R. Schnabel, T. Zwick, R. Weigel, and C. Waldschmidt, "Millimeter-wave technology for automotive radar sensors in the 77 GHz frequency band," *IEEE Transactions on Microwave Theory and Techniques*, vol. 60, pp. 845–860, Mar. 2012.

[111] A. Loch, A. Asadi, G. H. Sim, J. Widmer, and M. Hollick, "mm-Wave on wheels: Practical 60 GHz vehicular communication without beam training," in *2017 9th International Conference on Communication Systems and Networks (COMSNETS)*, pp. 1–8, Jan. 2017.

[112] J. Park, J. Lee, J. Liang, K. Kim, K. Lee, and M. Kim, "Millimeter wave vehicular blockage characteristics based on 28 GHz measurements," in *IEEE 86th Vehicular Technology Conference (VTC-Fall)*, pp. 1–5, Sept. 2017.

[113] A. U. Rahman, A. Ghosh, A. Chandra, J. Vychodil, J. Blumenstein, T. Mikulasek, and A. Prokes, "Time-variance of 60 GHz vehicular infrastructure-to-infrastructure (I2I) channel," *Vehicular Communications*, vol. 26, p. 100288, 2020.

[114] V. Petrov, J. Kokkoniemi, D. Moltchanov, J. Lehtomäki, M. Juntti, and Y. Koucheryavy, "The impact of interference from the side lanes on mmwave/THz band V2V communication systems with directional antennas," *IEEE Transactions on Vehicular Technology*, vol. 67, pp. 5028–5041, June 2018.

[115] I. Rasheed and F. Hu, "Intelligent super-fast vehicle-to-everything 5G communications with predictive switching between mmwave and THz links," *Vehicular Communications*, p. 100303, 2020.

[116] "Technical Specification Group Radio Access Network; Study on channel model for frequencies from 0.5 to 100 GHz," Tech. Rep. 38.901 v15.0.0, 3rd Generation Partnership Project (3GPP), June 2018.

[117] M. R. Akdeniz, Y. Liu, M. K. Samimi, S. Sun, S. Rangan, T. S. Rappaport, and E. Erkip, "Millimeter wave channel modeling and cellular capacity evaluation," *IEEE Journal on Selected Areas in Communications*, vol. 32, pp. 1164–1179, June 2014.

[118] M. Boban, D. Dupleich, N. Iqbal, J. Luo, C. Schneider, R. Müller, Z. Yu, D. Steer, T. Jämsä, J. Li, and R. S. Thomä, "Multi-band vehicle-to-vehicle channel characterization in the presence of vehicle blockage," *IEEE Access*, vol. 7, pp. 9724–9735, Jan. 2019.

[119] J. G. Andrews, F. Baccelli, and R. K. Ganti, "A tractable approach to coverage and rate in cellular networks," *IEEE Transactions on Communications*, vol. 59, pp. 3122–3134, Nov. 2011.

[120] J. Ploeg, A. F. A. Serrarens, and G. Heijenk, "Connect & drive: design and evaluation of cooperative adaptive cruise control for congestion reduction," *Journal of Modern Transportation*, vol. 19, pp. 207–213., Sept. 2011.

[121] M. Gramaglia, P. Serrano, J. A. Hernández, M. Calderon, and C. J. Bernardos, "New insights from the analysis of free flow vehicular traffic in highways," in *2011 IEEE International Symposium on a World of Wireless, Mobile and Multimedia Networks*, pp. 1–9, 2011.

[122] J. Park, J. Lee, K. Kim, K. Lee, and M. Kim, "Vehicle antenna position dependent path loss for millimeter-wave V2V communication," in *2018 11th Global Symposium on Millimeter Waves (GSMM)*, pp. 1–3, May 2018.

[123] N. Akhtar, S. C. Ergen, and O. Ozkasap, "Vehicle mobility and communication channel models for realistic and efficient highway VANET simulation," *IEEE Transactions on Vehicular Technology*, vol. 64, no. 1, pp. 248–262, 2015.

[124] Department for Transport, "Road traffic estimates: Great Britain 2018." [Online]. Available: `https://assets.publishing.service.gov.uk/government/uploads/system/uploads/attachment_data/file/808555/road-traffic-estimates-in-great-britain-2018.pdf`, May. 2019.